DESIGN, ANALYSIS AND FABRICATION OF PIEZOELECTRIC

MICROMACHINED ULTRASONIC POWER

TRANSDUCERS FOR BIOMEDICAL

IMPLANTS

by

Hamid Basaeri

A dissertation submitted to the faculty of
The University of Utah
in partial fulfillment of the requirements for the degree of

Doctor of Philosophy

Department of Mechanical Engineering

The University of Utah

August 2019

The University of Utah Graduate School

STATEMENT OF DISSERTATION APPROVAL

The dissertation of **Hamid Basaeri**

has been approved by the following supervisory committee members:

Shadrach Roundy	, Chair	**6/4/2019**
		Date Approved
Bruce Gale	, Member	**6/4/2019**
		Date Approved
Jiyoung Chang	, Member	**6/4/2019**
		Date Approved
Darrin Young	, Member	**6/4/2019**
		Date Approved
Prashant Tathireddy	, Member	**6/4/2019**
		Date Approved

and by **Bruce Gale** , Chair of

the Department of **Mechanical Engineering**

and by David B. Kieda, Dean of The Graduate School.

ABSTRACT

Bioimplantable devices have been used to perform therapeutic functions such as drug delivery or diagnostic monitoring of physiological parameters. Proper operation of these devices depends on the continuous, reliable supply of power. Ultrasonic power transfer systems can wirelessly power bioimplantable devices. The power delivered to the implant should remain stable and reliable even with possible uncertainties in the location of the implant. Although commercial off-the-shelf (COTS) transducers are widely used in the literature, they may not be the best candidate for powering small implants since they may not be able to provide sufficient power in the presence of location uncertainties. In this work, a diaphragm-based structure, which uses piezoelectric materials (also known as piezoelectric micromachined ultrasonic transducers), is fabricated on a small scale suitable for implantable devices. The proposed process demonstrates a new method to fabricate ultrasonic power receivers for bio medical implants. For the first time, a MEMS scale ultrasonic power receiver suitable for bio implantable devices is designed and fabricated that enables the highest demonstrated power output to our knowledge. The pMUT is able to generate a power of 0.7 mW across an optimal resistive load of 4.3 kΩ when separated from the transmitter by a distance of 20 mm. The transmitter generates an input power intensity of 322 mW/cm^2 at 88 kHz, less than Food and Drug Administration limit of 720 mW/cm^2. A comparative study is performed between power generation capability of the pMUT and a COTS transducer with the same lateral dimensions as the pMUT. It is

demonstrated that the pMUT has a more robust performance in the presence of location and orientation uncertainties compared to COTS bulk-mode piezoelectric transducers. Finally, this project compares the efficiency of acoustic power transfer systems to RF systems. The highest efficiency of the systems evaluated is an APT system with 12.8 mm diameter receiver, which achieves 46.5% efficiency at 30 mm separation distance. However, an APT with a smaller (2 mm × 2 mm) pMUT receiver results in 0.14% efficiency (4.5% area normalized efficiency) with at the same depth. This system can be slightly improved with a larger transmitter.

TABLE OF CONTENTS

ACKNOWLEDGMENTS

Hereby, I would love to deeply acknowledge the people whose contributions have made my graduate experience at the University of Utah a successful and wonderful one.

First, I want to express my sincere gratitude to my advisor Prof. Shad Roundy, for providing the necessary balance between guidance and freedom for independent work throughout my time here. There are many things I have learned from him that I will treasure for the rest of my life. Thank you very much.

I would also like to thank my committee members Dr. Darrin Young, Dr. Prashant Tathireddy, Dr. Bruce Gale, and Dr. Jiyoung Chang for all their valuable insights and comments. In particular, I would like to thank Dr. Darrin Young, and his student Yuechuan Yue, for kindly helping me and providing me access to the impedance analyzer in their lab. I also want to extend my gratitude to my fellow labmates in Integrated Self-Powered Sensing Lab and friends who made my life more enjoyable during my Ph.D. studies.

Beyond my committee, I appreciate the technical support and discussions with staff in the Utah Nanofab. In particular, Brian Baker, Tony Olsen, and Steve Pritchett proved to be valuable resources in helping with MEMS fabrication processes.

I would like to thank my dad and mom for the sacrifices they made and their unconditional love. I would not be able to become what I am today without their generous support. I hope to do the same and be there for them. I also thank my brother and wish him the very best in his life.

Last but not the least, I would like to thank my beloved wife Yekta, whose role in my life was and remains immense, for her emotional support, encouragement, and patience throughout the long journey of my Ph.D. studies.

CHAPTER 1

INTRODUCTION

1.1 Motivation

Implantable medical devices (IMDs) are designed for monitoring biological parameters, drug delivery, or improving the function of certain organs in the human body. The expanded use of IMDs for monitoring patient health will be an essential medical instrument in the near future. Patients with serious diseases such as bradycardia, fibrillation, or diabetes, to name just a few, may need these devices to better improve their health [1]. The existing interaction between medicine and technology allows for the development of new implantable devices to detect or monitor diseases inside the human body [2]. An implantable device needs a reliable supply of power for operation. Batteries, the traditional method of supplying power to implants, eventually require replacement, which typically requires invasive surgery. Although they are a convenient and reliable source of energy with relatively high energy density, they may not be the best candidate to power small implantable devices due to their limited lifetime. Furthermore, implants should be as small as possible to reduce trauma to the patient. However, because their miniaturization has not kept pace with the shrinking size of sensing and computational elements [3], onboard power sources such as batteries can dominate the size of implants and be a limiting factor for miniaturization. One alternative to battery power is to use inductive power transfer (IPA)

or mid to far field radio frequency (RF) transmission. However, for very small sensors ($\sim$mm^3) or for sensors at large implant depths ($>$ 1 cm), IPA and RF power transfer become extremely inefficient [4]. IPA and RF power transfer techniques typically require high operating frequencies. At very high frequencies, the absorption in tissue becomes severely limiting, and it may also cause tissue heating. At lower frequencies, a mm^2 scale receiving antenna becomes very inefficient. On the other hand, acoustic power transfer (APT) has much lower absorption in tissue. Additionally, the acoustic wavelength is much lower than RF meaning the optimal energy receiving structure (i.e., antenna) can be much smaller. Therefore, using acoustics to transfer energy rather than RF could enable much smaller and more deeply implanted biosensing systems.

Although there is a wide variety of possible transduction methods to convert acoustical to electrical energy, only a few are frequently used in practice. At very small scales, a diaphragm type receiver will produce significantly more power than a traditional disc receiver due to the diaphragm's greater compliance and lower effective acoustic impedance. Diaphragm structures can be made with a single piezoelectric layer (i.e., a unimorph), or a piezoelectric layer on each side of an elastic layer (i.e., a bimorph). The piezoelectric layer can either partially cover the elastic layer or cover the entire surface of the elastic layer and employ patterned electrodes on the piezo surface. There are two standard manufacturing techniques for diaphragms: diaphragms with deposited piezo material and diaphragms with screen printed piezo material. However, neither of them can provide the desired piezo thickness, which results in the optimal received power. Therefore, a new process could enable higher power density for this application. An additional problem is that the acoustic power receiver may be misorientated at some angle with

respect to the transmitter and may be laterally misaligned after being implanted in the human body. The power transferred to the receiver is sensitive to all of these uncertainties. Diaphragm structures are less sensitive to these uncertainties compared to COTS bulk mode transducers of similar size due to operating at a lower frequency. In order to undertake the experimental part of the project, a MEMS process has been developed to realize high efficiency millimeter scale power receivers that are designed for robust operation in the presence of location and orientation uncertainties.

It is important to note that acoustic power transfer could enable a fundamentally new method of powering and communicating with a wide range of implanted sensors leading to more effective diagnostic tools for clinicians and better maintenance of chronic conditions without the need to visit a doctor. The method could enable almost any implanted sensor that one might envision. Lower cost and less intrusive methods to monitor chronic conditions improve both the ability to manage these conditions and decrease healthcare costs. Implanted medical devices are not new. However, as they are usually quite large, the procedure to implant them is difficult and can be traumatic. Thus, they are generally used in more severe situations. Sensing technologies and associated electronics have achieved size scales that would make implanted sensors much less intrusive. However, the power supply generally requires that the implanted sensing systems be much larger. The proposed ultrasonic powering platform could overcome these limitations and make smaller implanted sensors achievable. The practical results of this research are that it would become less difficult and less expensive to implant sensors and other medical devices.

1.2 Research Objectives and Tasks

To achieve the research goals of this project, we accomplish three objectives: (1) identify the best architecture for powering biomedical devices, (2) develop a MEMS process and fabricate a device, and (3) characterize and evaluate power robustness. The key outcome of this research is to demonstrate that a MEMS scale diaphragm ultrasound receiver can perform more robustly compared to an off-the-shelf bulk-mode transducer in presence of location uncertainties. There are three objectives to this project, and they are arranged in a progressive manner as follows:

Objective 1: identify the best architecture for powering biomedical devices. The first aim is to compare the available mechanisms and architectures for powering implantable devices and identify the one that can best provide sufficient and stable power to a biomedical implant. Two common piezoelectric generator architectures that may be used for acoustic power transfer are the bulk-mode plate and the flexure-mode unimorph diaphragm. The plate that operates in thickness mode is a circular piezoelectric disk that is rigidly fixed around its circumference. This structure operates in 3-3 mode, meaning that the piezoelectric poling axis and the dominant strain direction are both perpendicular to the face of the plate. The diaphragm architecture is a circular piezoelectric disk fixed to the back side of a larger circular non-piezoelectric elastic layer. The elastic layer is usually fixed around its circumference. This structure operates in 3-1 mode in which the poling axis is perpendicular to the face of the diaphragm (direction 3), whereas the strain is dominant in the direction parallel to the face of the diaphragm (direction 1). The diaphragm may be a better choice due to its two main advantages: low frequency for a given size enabling lower acoustic loss through tissue, and robustness to misorientation and

misalignment.

Objective 2: develop a MEMS process and fabricate a device. Under currently available fabrication technology, piezoelectric materials can be deposited in thicknesses up to approximately 6 μm. There are several deposition techniques for integration of piezoelectric materials on silicon; however, there are extreme challenges in getting a PZT layer with a thickness more than 6 μm. The devices that result from deposited PZT typically suffer from low piezoelectric coefficients compared to bulk piezoelectric materials. As bulk piezoelectric materials provide much more electromechanical force due to the simple fact that they contain more piezoelectric material, maximum power generation is usually obtained with bulk materials rather than thin-film deposited piezoelectric materials. However, piezoelectric materials can be purchased in thicknesses above about 127 μm. This leaves a significant gap in achievable thicknesses. A new fabrication process is proposed and a pMUT device is fabricated by starting with bulk PZT with a thickness of 127 μm and polishing it back to get a PZT layer that is thicker than standard microfabrication processes, but thin enough for a millimeter scale bending diaphragm. This is followed by characterizing the fabricated device in order to evaluate its performance and validate the models.

Objective 3: characterize and evaluate power robustness. The third aim is to experimentally study the sensitivity of the received power from the fabricated MEMS receiver with respect to depth, alignment, and orientation of the receiver, and operating frequency, and compare the power results to off-the-shelf transducers. After the receiver has been fabricated, it is placed in water at a distance from a transmitter. The transmitter is first characterized separately. The transmitter impedance, capacitance, and resonance

frequency are measured. As the orientation of the implant cannot be perfectly controlled, it is important to consider the effect of the misalignment between the external acoustic power transmitter and implanted receiver. However, the orientation effect is complex for the geometry under consideration and needs to be validated experimentally. As a system, power and voltage magnitude and sensitivity to receiver position are measured and compared to finite element modeling. The generated results are compared to results from a COTS receiver to evaluate the improvement of the performance of the fabricated device in terms of robust operation in the presence of location and orientation uncertainties. A small COTS receiver with a size similar to the fabricated device is placed in the tank and the receiver voltage and power are recorded for the same scenarios. The voltage and power values are compared to the values from the fabricated device.

1.3 Dissertation Overview

This dissertation is divided into six chapters that correspond to the motivation (Chapter 1); background and literature review (Chapter 2); evaluate ultrasonic receiver structures for powering implantable devices (Chapter 3); study the performance of a MEMS ultrasonic transducer in presence of position and alignment uncertainties (Chapter 4); study the efficiency of acoustic power transfer systems and radio frequency power transfer systems (Chapter 5); and the conclusion of the dissertation (Chapter 6). The piezoelectric micromachined ultrasonic transducer is fabricated in the Utah Nanofab.

- Chapter 1 introduces the motivation of this project and discusses research objectives.
- Chapter 2 presents a comprehensive literature review on wireless power transfer

methods for bio medical implants and in particular acoustic power transfer. Current issues and challenges related to the implementation of this technique for powering implantable devices are presented. This chapter is a reprint of a journal article that has been published in *Smart Materials and Structures*.

- Chapter 3 presents the design and fabrication of a MEMS ultrasonic receiver. The frequency and the generated output voltage and power from different ultrasonic transducers are compared and the best structure is selected for fabrication. This chapter is a reprint of a journal article that has been published in *IEEE Sensors Letters*.

- Chapter 4 presents the performance evaluation of the fabricated pMUT when the receiver is not perfectly aligned with the transmitter. The results are then compared to a COTS receiver with a similar area to the pMUT. This chapter is a reprint of a journal article that has been published in *Journal of Micromechanics and Microengineering*.

- Chapter 5 presents comparative study between the efficiency of APT systems and RF systems. The area normalized efficiency is discussed for two APT systems, and then is compared to the efficiency from RF systems. The comparison is done when the distance between the transmitter and the receiver are equal for APT and RF systems.

- Chapter 6 summarizes the results of the work of this project, which focuses primarily on MEMS ultrasonic power receivers and their potential for wirelessly powering implantable devices. In addition, this chapter identifies original contributions of this project and offers suggestions for future work.

1.4 References

[1]　M. A. Wood and K. A. Ellenbogen, "Cardiac pacemakers from the patient's perspective," *Circulation*, vol. 105, no. 18, pp. 2136–2138, 2002.

[2]　J. Lueke and W. Moussa, "MEMS-based power generation techniques for implantable biosensing applications," *Sensors*, 2011.

[3]　F. Akhtar and M. H. Rehmani, "Energy replenishment using renewable and traditional energy resources for sustainable wireless sensor networks: A review," *Renew. Sustain. Energy Rev.*, vol. 45, pp. 769–784, 2015.

[4]　A. Denisov and E. Yeatman, "Ultrasonic vs. Inductive Power Delivery for Miniature Biomedical Implants," *2010 Int. Conf. Body Sens. Networks*, pp. 84–89, 2010.

CHAPTER 2

A REVIEW OF ACOUSTIC POWER TRANSFER

FOR BIO-MEDICAL IMPLANTS

Topical Review

A review of acoustic power transfer for bio-medical implants

Hamid Basaeri, David B Christensen and Shad Roundy

Department of Mechanical Engineering, University of Utah, Salt Lake City, UT, USA

E-mail: h.basaeri@utah.edu

Abstract

Bio-implantable devices have been used to perform therapeutic functions such as drug delivery or diagnostic monitoring of physiological parameters. Proper operation of these devices depends on the continuous reliable supply of power. A battery, which is the conventional method to supply energy, is problematic in many of these devices as it limits the lifetime of the implant or dominates the size. In order to power implantable devices, power transfer techniques have been implemented as an attractive alternative to batteries and have received significant research interest in recent years. Acoustic waves are increasingly being investigated as a method for delivering power through human skin and the human body. Acoustic power transfer (APT) has some advantages over other powering techniques such as inductive power transfer and mid range RF power transmission. These advantages include lower absorption in tissue, shorter wavelength enabling smaller transducers, and higher power intensity threshold for safe operation. This paper will cover the basic physics and modeling of APT and will review the current state of acoustic (or ultrasonic) power transfer for biomedical implants. As the sensing and computational elements for biomedical implants are becoming very small, we devote particular attention to the scaling of acoustic and alternative power transfer techniques. Finally, we present current issues and challenges related to the implementation of this technique for powering implantable devices.

Keywords: implantable devices, energy harvesting, ultrasonic transducer, wireless power transfer

(Some figures may appear in colour only in the online journal)

1. Introduction

Bio-implantable or implantable medical devices (IMDs) are devices designed for monitoring biological parameters, drug delivery, or improving the function of certain organs in the human body. The expanded use of IMDs for monitoring patient health will be an essential medical instrument in the near future. Patients with serious diseases such as brady-cardia, fibrillation, and diabetes, to name just a few, may need these devices for their survival [1]. The existing interaction between medicine and technology allows for the development of new implantable devices to detect or monitor diseases inside the human body [2–4]. For instance, an implantable glucose sensor permits diabetics to obtain real-time, accurate glucose readings without pricking their finger [5]. Other

IMDs, such as those to measure blood pressure and implanted microelectrodes to monitor cerebral or intramuscular elec-tromyographic (EMG) signals, are explained in [6–8].

An implantable device needs a reliable supply of power for operation. Batteries, the traditional method of supplying power to implants, eventually require replacement which typically requires invasive surgery. Although they are a convenient and reliable source of energy with relatively high energy density, they are not the best candidate to power small implantable devices due to their limited lifetime. If the implant is large, and a large battery can be included, the lifetime may be many years [9, 10]. However, typically implants should be as small as possible to reduce trauma to the patient, and miniaturization of power sources has not kept pace with the shrinking size of the sensing and computational

elements. Subsequently, onboard power sources such as a battery can dominate the size of implants and be a limiting factor for miniaturization [11, 12]. This fact has led to a rich field of research on alternative methods to power implants.

For example, bio-medical devices can be powered by implantable fuel cell systems that are capable of converting endogenous substances and oxygen into electricity using a spatially separated electrochemical reaction. Glucose is one of the most common fuels due to its ubiquitous availability in the human body. Fuel cells enabled by enzymatic, microbial, and abiotically catalyzed reactions have all been proposed and demonstrated [13]. The state-of-the-art in abiotically cata-lyzed glucose fuel cells is fully reviewed by Kerzenmacher *et al* [14]. Based on their literature survey, abiotically cata-lyzed glucose fuel cells can generate power densities between 2.5 and 8 μW cm^{-2} for no longer than 100 days in *in vitro* experiments. Although this is a promising direction for future research and development, current state of the art does not support powering long term bio-implantable devices.

Vibrational or kinetic energy harvesting has also been proposed as a technique to power implantable devices. Vibrational energy harvesting systems harvest the energy of human motion in order to power a device. Generally speak-ing, vibration intensity available inside the body is usually very low [15], and therefore, cannot be considered as an appropriate method to power implantable devices. However, in certain specific applications, sufficient kinetic energy is available to harvest. These harvesters may use different methods to convert energy from the motion of the human body to electrical energy such as electromagnetic, electro-static, and piezoelectric conversion. An electromagnetic generator for diaphragm muscle movement developed in [16] is capable of producing up to 1 mW of power, but at an approximate volume of 16 cm^3 the power density is only 0.062 mW cm^{-3}. Chen *et al* [17] developed a device to be embedded in orthopedic implants which produces 1.2 mW in a volume of 0.45 cm^3. Although the power density of this device, 2.66 mW cm^{-3}, is enough for powering implantable devices, it is feasible only for knee implants since this power density can be achieved only in the presence of a 900 N force. Additionally, pacemakers can be powered from heartbeat vibrations. Karami and Inman have investigated the use of vibration energy harvesters for charging the batteries of pace makers as their power requirement is low (around 1 μW) [18, 19]. Their device can generate 8 μW of power from heartbeat oscillations. For a more detailed comparison and discussion of vibrational energy harvesting for implantable medical devices, we refer the reader to Hanan *et al* [20], Cadei *et al* [21], and Romero *et al* [22]. Other alternative energy harvesting methods such as optics [23], and thermal gradients [24] have also been implemented to power implantable devices, however, as temperature differentials and light are very scarce inside the body they are usually not very effective.

Given the limitations of batteries, and the challenge with harvesting existing energy within the body, there has been an increasing research effort on methods to wirelessly transfer power to medical implants [12, 20, 25–27]. These methods include power transfer by mid to far field radio frequency (RF) radiation, inductive power transfer (IPT), and acoustic (or ultrasound) power transfer (APT). Each method has some benefits. However, as the size of the implant shrinks and the depth grows, it has been shown that ultrasonic power transfer can be fundamentally more efficient than IPT [28, 29]. The goal of this paper is to review the state-of-the-art in trans-ferring power to bio-implantable devices using APT. In so doing, we will briefly review power transfer by both coupled electromagnetic coils and mid to far field RF methods for comparison. However, the bulk of the review will specifically cover APT. The remainder of this paper is organized as fol-lows: we first compare RF, coupled inductive coils, and acoustic techniques. Second, we will cover the fundamentals of APT including common modeling techniques. We will review published studies and acoustic power implementations along with their transducer designs. Finally, we draw some conclusions about profitable directions for future research.

2. Comparison of power transfer methods for medical devices

Radio waves cover the range of 3 kHz–300 GHz of the electromagnetic spectrum. The use of a set of transmitting and receiving antennas operating in the RF range allows for the transmission of power. For the purposes of this paper, we categorize electromagnetic transmission as either IPT if the coupling is in the near field, or RF if the coupling is in the mid field (i.e. transition region) or far field. We note that this differentiation is not universal in the literature, and often systems that exhibit near field coupling are referred to as RF. Nevertheless, in this paper, we will follow this classification. Far field RF transmission is omnidirectional and thus suffers from low efficiency. One of the major drawbacks of this method is that it loses its strength as it spreads further away from the source, and therefore, a very small amount of power is available to be harvested. Furthermore, this kind of radia-tion can cause potential risks to humans, thus the generated power should be applied only to low power applications (mW and μW) since the output power is restricted by government regulations [12]. As an example, Shih *et al* presented a pressure/temperature sensing device for continuous intrao-cular pressure monitoring with a single turn 10 mm diameter loop antenna to generate 2.3 μW of power operating at 2.4 GHz [30]. Poon *et al* proposed a mid field RF powering technique to increase the gain of the transmitted power signal and to avoid spreading. However, it does not overcome the issue with high attenuation in tissue [31, 32]. Microwaves, a sub-section of radio waves in the range of 3–300 GHz, can transfer power over long distances, however, they are not widely used since they are not safe when the RF exposure density is high. A schematic of a RF power transfer system is depicted in figure 1(a).

Inductive power transfer systems usually consist of two coupled coils which have the same inductance as shown in figure 1(b). The transmitter coil is placed outside of the body whereas the receiver coil is integrated with the implanted

a) Radio frequency   b) Inductive coupling   c) Acoustic
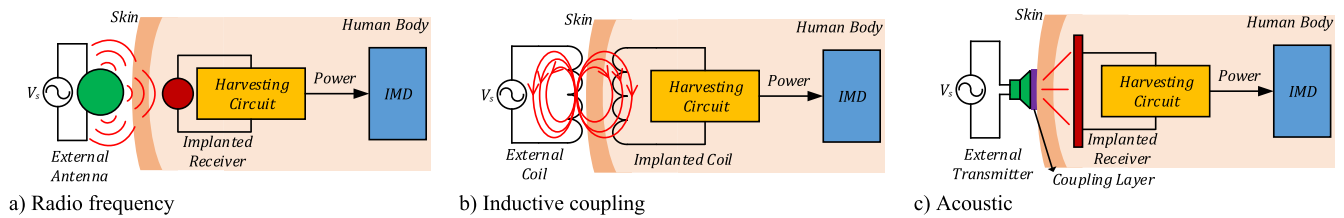
Figure 1. Different power transfer methods for powering IMDs.

device inside the body. When a sinusoidal current is placed on the transmitter coil, a voltage is induced in the receiver coil as a result of electromagnetic induction [25]. The generated voltage is conditioned and then fed to the IMD. The highest power and efficiency is achieved when both coils are tuned to their resonance frequency [29]. There are several factors which can affect the efficiency of the wireless power transfer including resonance frequency (or operating frequency) and coupling between the transmitter and the receiver coils which itself can be affected by distance and alignment. The inefficiency of IPT in a large space is discussed in [33], and it is stated that this kind of energy transfer is not practical for large distances because as the distance between transmitter and receiver coils compared to the coils' diameters increases, the coupling goes down leading to high conduction losses due to excessive reactive current. The literature is full of examples of IPT and RF powered sensors, including biomedical implants. A full review of this work is not possible here. Suffice it say that these methods clearly work, but suffer at small sizes and deep implant depths because the efficiency becomes very poor.

Acoustic energy is emitted from diverse types of mechanical waves which are capable of penetrating through gases, liquids and solids [34]. It can be harvested from the ambient environment or transferred wirelessly to a receiver as shown in figure 1(c). Typically, the acoustic wave, which is usually at ultrasound frequencies, is generated by a piezoelectric transducer that is in contact with the skin. The pressure wave transmits through the tissue and induces a voltage on a receiver structure which is also typically a piezoelectric device [35]. In the context of implanted devices, acoustic waves have some significant advantages over electromagnetic waves: they have shorter wavelengths which result in smaller sized receiving transducers, and they exhibit lower attenuation in human tissue which results in deeper penetration. Furthermore, some focusing techniques such as the one presented in [36] can be implemented on these devices due to the fact that their wavelengths are in the range of mm. These waves are safe to use in the human body at diagnostic intensities, and they are not susceptible to electromagnetic interference [37]. The transducers can also be designed in a compact size, which is an important feature for implantable devices. Acoustic waves are suitable for propagation within the predominantly liquid environment inside the human torso, and cause minimal tissue heating when operating at lower frequencies. There are some applications in which the implant incorporates electrodes and wiring to these electrodes. Electromagnetic power transfer can cause unwanted voltages

on these wires which may result in unintentional excitation whereas ultrasonic power transfer does not suffer from this problem. A more detailed discussion of the devices reported in the literature and the current state of the art will be presented in section 5.

Each of these power transfer approaches for implantable devices has its own advantages and weaknesses. Inductive coupling works in the near field, and the transferred power is reduced according to the cube of the reciprocal of the charging distance [38]. On the other hand, RF radiation works in the far field at a longer distance relative to the size of the antenna. The power in far field systems reduces according to the square of the reciprocal of the charging distance [38]. Additionally, there is no need for the transmitting and receiving antennas to be coupled for RF. However, for inductive coupling, the transmitting and receiving coils should be coupled [39]. Although inductively coupled power transfer systems can be implemented in a simple way, they need more accurate alignment than RF systems. Moreover, they have a shorter effective powering distance which makes using them difficult in implantable devices [40]. Furthermore, electromagnetic waves can generate excessive tissue heating, affecting the immune system, calcium metabolism and DNA synthesis [41, 42]. The efficiency of inductive and RF power transfer drops dramatically as the size decreases [43, 44] due to the relatively large wavelength of electromagnetic waves and the increased attenuation at high frequencies. For instance, a single turn 10 mm diameter loop antenna implanted at 15 mm depth has been shown to generate 2.3 μW [30]. However, the same amount of power at the same depth could be generated by an acoustic generator with a diameter of 1 mm or less [45, 46]. Overall, the research literature indicates that obtaining more power with smaller devices can be achieved by the use of APT.

Several devices utilizing differing power sources are compared in table 1 in terms of their frequency, power and size. As shown in figure 2, the operating frequency of RF devices is generally higher than inductive coupling and acoustic devices. Most RF and inductive coupling devices are tested in air while APT is usually analyzed in water or tissue. Figure 3 gives the depth of the implanted device in the body versus the receiver size for different devices in table 1 and shows that the implant depth for APT devices is typically higher compared to RF and IPT for the same size device. Figure 4 plots the output power intensity at the receiver face for these devices against the receiver size, and shows that typically higher power density is achieved using acoustics compared to RF and IPT devices with almost the same size.

Table 1. Comparison of several implantable devices with different powering mechanisms.

Method	Article								
	Author	Year/Ref	Efficiency (%)	Frequency (MHz)	Output power (mW)	Receiver area (cm^2)	Power intensity (mW cm^{-2})	Depth (mm)	Medium
Radio frequency (RF)	O'Driscoll	2009/ [49]		1000	0.14	0.04	3.5	15	
	Poon	2010/ [47]	0.2	1000	0.005	0.04	0.125	40	
	Shih	2011/ [30]	1.73	2400	2.3×10^{-3}	0.78	0.0029	15	Tissue
	Ho	2014/ [31]	0.04	1600	0.2	0.04	5	50	
Inductive coupling (IPT)	Jow	2007/ [50]	85.5	5		4		10	Air
	Kilinc	2010/ [51]	66.7	13.56		4		30	Air
	Kiani	2010/ [52]	1.02	13.56	11.2	1	11.2	20	Air
	Kiani	2011/ [53]	4.82	13.56	27	1.2	22.5	7	Air
	Silay	2011/ [54]	54.98	8	10	1	10	10	Air
	Liu	2013/ [55]		13.56	0.95	3	0.317	24	Pig skin
Acoustic (APT)	Arra	2007/ [56]	25	0.84	62.5	4.9	12.73	100	Water
	Larson	2011/ [57]	0.022	1	0.51	0.01	51	120	Rat hind limb
	Sanni	2012/ [58]	1	0.2	8	0.78	10.26	70	Water
	Mazzilli	2014/ [59]	1.6	1	28	0.3	93.33	105	Water
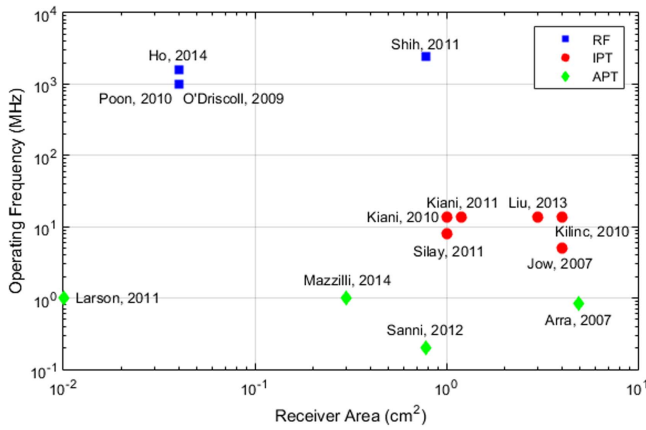
Figure 2. Operating frequency of reported devices versus receiver area.
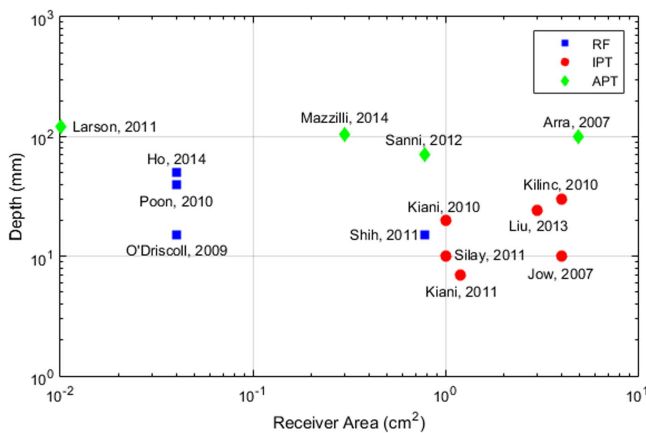
Figure 3. Implanted depth of reported devices versus receiver area.
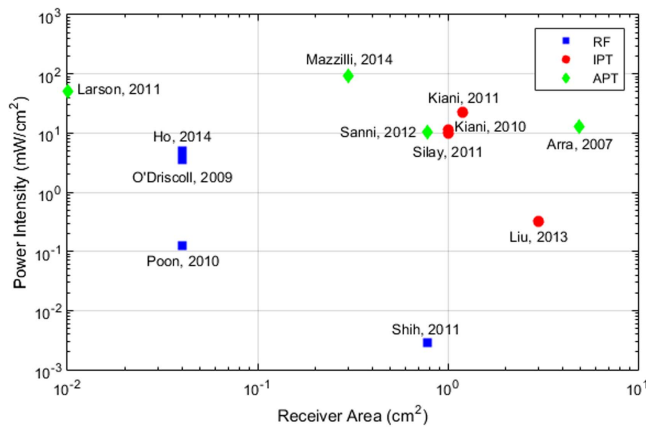
Figure 4. Output power intensity of reported devices versus receiver area.

For example, Poon *et al* [47] studied the optimal frequency for RF power transfer in tissue for a 4 mm^2 receiver. Their studies indicate an optimal efficiency of 0.2% at an implant depth of 4 cm. The resulting power generation would be 5 μW or 1.25 μW mm^{-2}. Note that if a 1 mm^2 receiver were used, the power generation may be even lower than 1.25 μW as the scaling is not necessarily linear. Alternatively, using the

power transmission models developed by Denisov *et al* [29], an acoustic power receiver of the same size at the same implant depth has an optimal efficiency of 2% (compared to 0.2% for RF). Given the increased efficiency, and the fact that the food and drug administration (FDA) limits for power transmission into tissue are higher for ultrasound (7200 μW mm^{-2}) than for RF radiation [48], the resulting optimal power density for acoustics is 144 μW mm^{-2}. With a 4 mm^2 receiver, 576 μW could be transferred. It should be noted that these FDA limits are for imaging or high intensity focused ultrasound devices since there is no specific limitation for ultrasound power transfer operating in continuous wave (CW) mode. Moreover, the safety limitations are not the same for all organs in the body. The 7200 μW mm^{-2} limitation is intended for peripheral vessels, however, there are some other organs such as cardiac, abdominal, and ophthalmic organs having much lower limitations [44]. Operating frequency is another important factor affecting the regulation limits. The dependency of safety limits to the operating frequency will be covered in the frequency selection section. Thus, at these very small sizes and large implant depths, an acoustically powered sensor would have roughly two orders of magnitude more power at its disposal. The advantages of acoustic energy transfer compared to other sources of energy make it an appropriate choice for powering bio-implantable devices.

3. Acoustic power transfer

The devices shown in table 1, are specific instantiations and typically only tested at a single depth. This section will cover the physics of APT in order to provide a more complete picture of its potential. The basic structure of an APT system for a bio-medical implant is depicted in figure 5. An external ultrasonic transmitter converts electrical energy into a pressure wave which is transferred through the medium (i.e. body tissue). The pressure wave is captured by a receiver implanted in the body, and converted to electrical energy by an inverse process. A rectifier provides a usable stable DC voltage for powering a bio-sensor.

3.1. Fundamentals of acoustics

The field of physical acoustics deals with the generation and propagation of sound. A time-dependent external source can generate a perturbation into a gas, liquid, or solid in order to deliver momentum and energy to the medium. The propagation of the acoustic wave away from the source at a finite speed is a function of the elastic properties and density of the medium, and is governed by the wave equation [60].

The wave equation governing linear, lossless acoustic motion is derived for a linearized version of the principle of conservation of mass and momentum under the assumption of an isentropic equation of state [61]:

$$\frac{1}{c^2}\frac{\partial^2 p}{\partial t^2} - \nabla^2 p = 0, \tag{1}$$
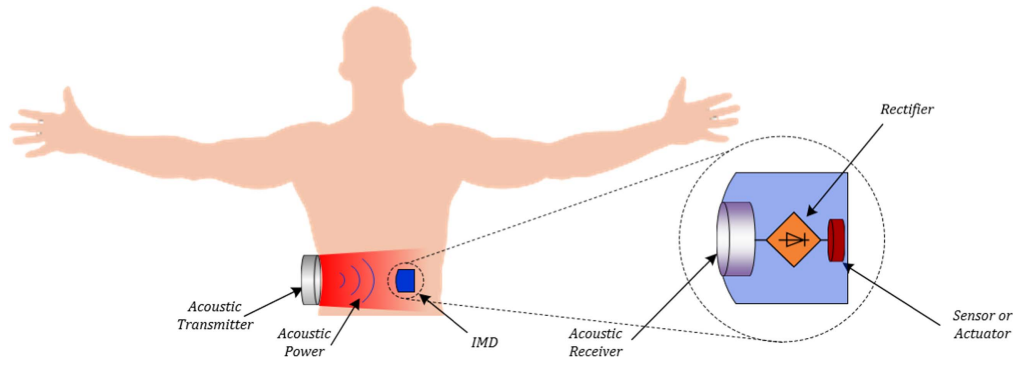
Figure 5. Diagram of an acoustic power transfer system for bio-medical implant.

Table 2. Mechanical properties of several materials used for acoustic transmission [63, 64].

Material	Density (kg m^{-3})	Acoustic velocity (m s^{-1})	Acoustic impedance (MRayls)
PZT	7500 ~ 8000	4000 ~ 5000	30 ~ 40
Water (20 °C)	1000	1480	1.48
Air (25 °C)	1.2	346	0.000 409
Human tissue	1490 ~ 1610	1060	1.58 ~ 1.7

where c is the isentropic speed of the sound and p is the acoustic pressure with respect to mean pressure. The pressure fluctuation, $p(x, t)$, can be derived as a function of the acoustic particle velocity, $u(x, t)$ for a plane, progressive acoustic wave propagating along the x-axis as [60]:

$$p(x, t) = \rho c u(x, t), \tag{2}$$

where ρ is the density of the medium and $Z = \rho c$ is the acoustic impedance of the medium. The SI unit of acoustic impedance is the $\mathrm{Pa\,s\,m^{-1}}$, often called the rayl (1 rayl = $1\,\mathrm{Pa\,s\,m^{-1}} = \mathrm{kg\,s^{-1}\,m^{-2}}$). Acoustic impedance specifies how much pressure is generated by the vibration of the medium at the desired frequency. The acoustic impedance in a material is the product of its density and the speed of sound in the material [62]. The acoustic impedance for several materials can be found in table 2. It should be mentioned that some of the values for PZT and human tissue are reported as a range. This is due to the fact that there are several types of PZT materials as well as human tissue, and each of them has different properties. Moreover, the acoustic velocity depends on the direction in the material. As can be seen, there is a considerable mismatch between the acoustic impedance of piezoelectric material and tissue. In the case where there is a large impedance mismatch, a larger vibration amplitude would need to be generated by the transmitter in order to push the desired acoustic power to the tissue than with a matched transducer. This issue will be fully covered in the impedance matching section.

The instantaneous acoustic intensity, $\vec{I}(x, y, z, t)$, is defined as the power per unit area and can be calculated by knowing the acoustic particle velocity vector $\vec{u}(x, y, z, t)$ [60]:

$$\vec{I}(x, y, z, t) = p(x, y, z, t)\vec{u}(x, y, z, t). \tag{3}$$

The corresponding acoustic power W of the source can then be found by integrating the intensity over the source area.

The characteristics of the generated pressure field in a medium change with distance from the transmitter. The pressure field is generally split into the near field and far field. In the near field, for a cylindrical transmitter, the shape of the pressure field is cylindrical and the pressure magnitude oscillates with distance from the transmitter having multiple minima and maxima which make the power transfer unpredictable [35]. In other words, the perturbation to the transmitter, which is caused by having an object in its near field, makes it hard to predict the transferred power. At a certain distance from the transmitter on the acoustic axis, the beam begins to diverge and the pressure field changes to a spherically spreading wave which decays with increasing distance. The far field is generally smoother than the near field with pressure decaying with distance. At the transition between the near field and far field, as seen in figure 6, the pressure field converges to a natural focus. This transition distance is called the Rayleigh distance and is defined as [65]:

$$L = \frac{(D^2 - \lambda^2)}{4\lambda} \approx \frac{D^2}{4\lambda}, D^2 \gg \lambda^2, \tag{4}$$

where D is the aperture width of the source or transmitter and λ is the wavelength of the acoustic wave in the medium, which is a function of frequency, f.

The wavelength, λ, is defined as:

$$\lambda = \frac{c}{f}. \tag{5}$$

At the Rayleigh distance, for circular transducers, the acoustic beam spreads out at an angle that can be calculated
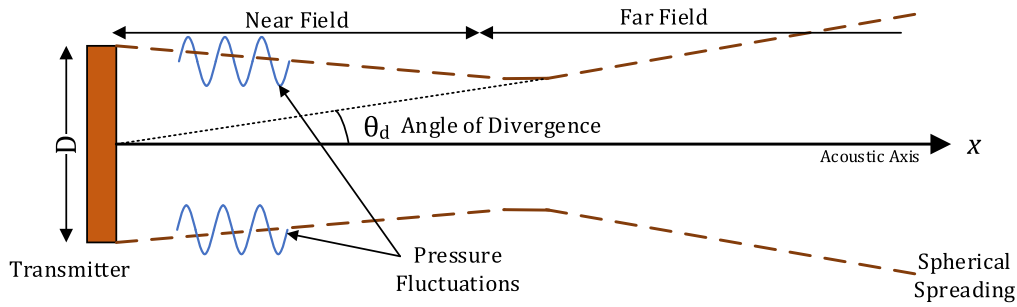
Figure 6. Representation of near field and far field.

by the wavelength and the diameter of the transmitter as:

$$\theta_d = \sin^{-1}\left(\frac{1.22\lambda}{D}\right). \tag{6}$$

By knowing the intensity at zero distance, $I(0)$, the intensity distribution for each point on the propagation axis can be given by:

$$I(x) = I(0)\sin^2\left[\left(\frac{\pi}{\lambda}\right)\left(\sqrt{\frac{D^2}{4} + x^2} - x\right)\right]. \tag{7}$$

In order to achieve the maximum received power, it is best to place the receiver at one Rayleigh distance where the beam spreading is at a minimum [66], and the acoustic pressure has a large and stable value. On the acoustic axis in the near field, there are several points at which the pressure has its maximum value. The location of these points depends on the wavelength and the diameter of the transmitter. Considering m as the order of the pressure peak, the pressure peak locations can be calculated as [35]:

$$X_{\max}(m) = \frac{D^2 - \lambda(2m + 1)^2}{4\lambda(2m + 1)} \quad m = 1, 2, 3, \dots. \tag{8}$$

3.2. Impedence matching

When there is an impedance mismatch for a wave generated by a transducer with acoustic impedance Z_2 propagating in a medium with acoustic impedance of Z_1, a reflection coefficient, for normal incidence, can be defined as [64]:

$$\Gamma = \frac{Z_2 - Z_1}{Z_2 + Z_1} = \frac{P_r}{P_i}. \tag{9}$$

The reflection coefficient can be interpreted as the ratio of the amplitude of the reflected wave P_r to the amplitude of the incident wave $_{Pi}$. Therefore, the transferred pressure wave will be $P_t = (1 - \Gamma)_{Pi}$. This means that the larger the reflection coefficient value, the smaller the captured wave by the receiver. According to table 2, there is a mismatch between the acoustic impedance of PZT (39.71 MRayls) and average value for human tissue (1.64 MRayls), and therefore, the reflection pressure coefficient will be 0.92. Therefore, only

$(1 - \Gamma) = 0.08$ of the generated wave is captured by the receiver. The situation is actually worse as the power depends on P_t squared which is proportional to $(1 - \Gamma)^2$. In other words, the intensity of the reflected wave I_r depends on the square of Γ and can be written as:

$$\frac{I_r}{I_i} = |\Gamma|^2. \tag{10}$$

Another concern with mismatched impedances is the generation of pressure standing waves in the tissue by the reflected wave [61]. As discussed in the previous section, this problem can cause peak pressure levels that exceed the tissue safety limit. Hence, in order not to exceed the tissue safety limit and to avoid any losses in the transferred power, it is necessary to match the transducer impedance to the tissue impedance.

Acoustic impedance matching techniques can generally be classified as either single or multiple matching layer methods. The single matching layer method is the easiest and the most common technique. Using this method, a layer with a thickness of $\lambda/4$ is inserted between the transducer and the medium. It should be mentioned that this single matching layer technique using a layer with a thickness of $\lambda/4$ works well at a single frequency and is not broadband. The inserted layer should be biocompatible and have an acoustic impedance close to [35]:

$$Z_{\text{matching}} = \sqrt{Z_1 . Z_2}. \tag{11}$$

The main disadvantage of using the single layer matching technique is that it considerably limits the availability of a biocompatible material with the calculated acoustic impedance. For the case of PZT and tissue, the calculated acoustic impedance is 8.1 MRays, and there are few biocompatible materials with this acoustic impedance value. Another issue of this method is that it does not consider the adhesion layer between the transducer and the new material which can negatively affect the quality of matching. Of course, its effect on the matching layer is negligible if the adhesion layer thickness is thin compared to the matching layer thickness.

Alternatively, multiple layers for matching the acoustic impedances of the transducer and tissue can be used [63, 67–69]. Each of the matching layers and their adhesive layers are represented by a 2×2 matrix. The acoustic impedance

matching is then obtained by the multiplication of a chain of transfer matrices. For the nth layer with acoustic impedance of Z_n, the transfer matrix is defined by [69]:

$$T_n = \begin{bmatrix} \cos \theta_n & jZ_n \sin \theta_n \\ \dfrac{j}{Z_n} \sin \theta_n & \cos \theta_n \end{bmatrix}, \qquad (12)$$

where $\theta_n = 2\pi t_n / \lambda_n$ is the phase shift, and t_n is the thickness of nth layer. Then, the equivalent matrix T_{equ} can be obtained by multiplying the transfer matrices for each layer as:

$$T_{\text{equ}} = T_1 T_2 \dots T_n = \begin{bmatrix} T_{11} & T_{12} \\ T_{21} & T_{22} \end{bmatrix}. \qquad (13)$$

When the equivalent acoustic impedance of all the layers equals the acoustic impedance of the tissue, matching is obtained. Assuming Z_1 to be the acoustic impedance of the transducer, the equivalent acoustic impedance resulting from multi layers is then given by:

$$Z_{\text{equ}} = \frac{T_{11} Z_1 + T_{12}}{T_{21} Z_1 + T_{22}}. \qquad (14)$$

Finally, it should be noted that the effective acoustic impedance of the receiver can be adjusted through the electrical impedance of the load circuitry [28]. The acoustic impedance of bulk ceramics is more or less constant. However, the acoustic impedance of poled electroceramics depends strongly on the frequency near resonance. Thus, the acoustic impedance is a function of both the frequency and electrical load [35, 70].

3.3. Frequency selection

It is important to select a proper transmission operating frequency as several critical operational factors can be negatively impacted by improper selection, such as tissue attenuation, Rayleigh distance, and the size of the receiver and transmitter. The best choice is to use the resonance frequency of the transducer and operate the transducer close to this frequency in order to achieve the maximum transferred power. The resonance frequency of the transducer depends on the geometry and material of the transducer. By increasing the frequency, the thickness of transducers and matching layer decrease. However, the Rayleigh distance increases with frequency, which leads to an increase of losses due to tissue absorption.

Both the frequency and the intensity of the acoustic field affect safety. The FDA states that for continuous energy transfer through tissue, the spatial-peak temporal-average intensity (I_{SPTA}) should be less than $7200 \, \mu\text{W mm}^{-2}$ to avoid any thermal damage [48]. In order to address mechanical damage, the FDA limits the spatial-peak peak-average intensity (I_{SPPA}) for pulse wave telemetry and energy delivery to be less than $190 \, \text{W cm}^{-2}$ [48]. Finally, in order to measure and estimate ultrasonic bio-effects, the mechanical index (MI)

is defined as [71]:

$$\text{MI} = \frac{p_n}{\sqrt{f_{\text{c}}}}, \qquad (15)$$

where p_n is peak negative pressure of the ultrasound wave in MPa, de-rated by $0.3 \, \text{dB cm}^{-1} \, \text{MHz}^{-1}$ to account for the difference between in-water and in-tissue acoustic attenuation, and f_{c} is the center frequency of the ultrasound wave in MHz. MI is an indication of an ultrasound beam's ability to cause cavitation related bio-effects, and can be considered as a reasonable proxy for micro mechanical damage. A higher MI produces a larger bio-effect (cavitation) [59]. Therefore, cavitation is less prominent at high frequencies whereas lower frequencies can be less safe. To reduce the risk of cavitation for diagnostic ultrasound, the FDA states that the MI must be lower than 1.9 [48].

Other parameters that can be affected by the operating frequency are the attenuation factor α and the loss of pressure amplitude. The pressure can be expressed as [59]:

$$p(x) = p_0 \exp^{-\alpha(f)x}, \qquad (16)$$

where the attenuation factor $\alpha(f) = \alpha \times f_0^k$ is a function of operating frequency. The average attenuation coefficient for biological soft tissue α is considered to be $0.3 \, \text{dB cm}^{-1} \, \text{MHz}^{-1}$ [72, 73]. The distance along the acoustic axis is x, and k is a constant with a value of 1 for tissue. The normalized pressure ($p(x)/p_0$) exponentially decreases with increasing operating frequency for a constant distance. Hence, higher frequencies limit the penetration of ultrasound and promote heating.

3.4. Transducer structures

Although there is a wide variety of possible transduction methods to convert acoustical to electrical energy, only a few are frequently used in practice. Most acoustic power generators employ electrostatic [74, 75] or piezoelectric [28] transduction methods. Piezoelectric transduction is the most common method used for receiving acoustical energy and converting it to electrical energy [60] and vice-versa. Figure 7 shows two common types of piezoelectric architectures which can be used for APT: the bulk-mode plate and the flexure-mode unimorph diaphragm. The plate is a circular piezoelectric disk that is usually fixed around its circumference. The piezoelectric 3–3 axis, which is the poling axis, is perpendicular to the face of the plate. The diaphragm is also a circular piezoelectric disk. However, one face of the piezoelectric disk is fixed to the back side of a larger circular elastic layer, or shim that is not piezoelectric. The shim is clamped around its circumference. Figure 7 shows two different diaphragm architectures. Diaphragm structures can be made with a single piezoelectric layer (i.e. a unimorph), or a piezoelectric layer on each side of the shim (i.e. a bimorph). The piezoelectric layer can either partially cover the shim or cover the entire surface of the shim and employ patterned electrodes on the piezo surface. If implemented as a MEMS device, this structure is usually referred to as a piezoelectric micromachined ultrasound transducer or PMUT.
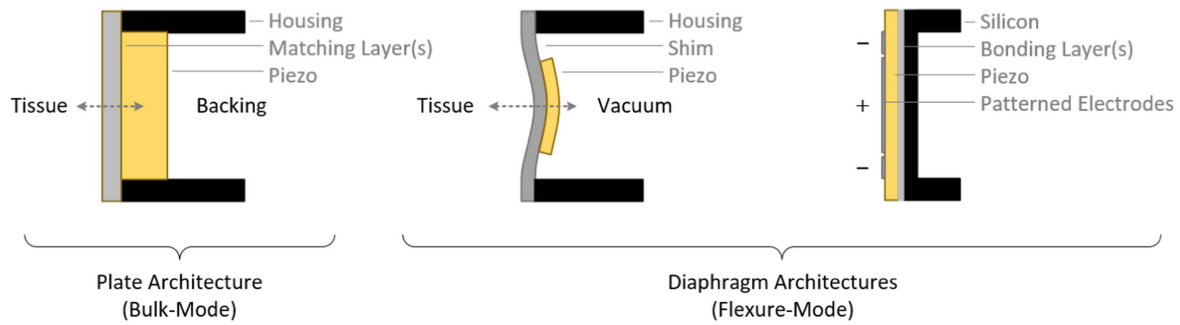
Figure 7. Plate (left), unimorph diaphragm (middle), and patterned-electrode PMUT diaphragm (right) architectures.

The literature is focused more on the plate architecture for transferring power in an implantable device. There are two main reasons that the plate structure can have better performance compared to the diaphragm. First, the diaphragm structure operates in 3–1 mode which, for most materials, has a lower coupling coefficient compared to the 3–3 mode of the plate. Second, plates use significantly more piezoelectric material than diaphragms of the same diameter and thus have better performance in terms of acoustic to electric generation. However, diaphragm structures can operate at much lower frequencies for a given diameter leading to less signal attenuation and tissue heating which can make them appealing for bio-implantable power applications. Christensen and Roundy [28] analyzed these two structures as implantable acoustic receivers for powering small, deeply implanted devices, and compared the power loss mechanisms and the total power generated for these two structures. They showed that the diaphragm architecture generates more power compared to plate architecture for large implant distances and small device sizes. They also concluded that the diaphragm is generally less sensitive to misalignment and differences in orientation.

Piezoelectric materials are widely applied in a variety of macroscale devices; however, their integration into microsystems has been challenging. Among lead zirconate titanate (PZT), zinc oxide, and aluminum nitride, PZT is the dominant piezoelectric material for power generation purposes in the literature [3] given that it exhibits higher piezoelectric coefficients, d_{33}, d_{31}, and coupling coefficients [76]. Existing deposition techniques for integration of piezoelectric materials on silicon are introduced in [77] and their challenges are discussed. As bulk piezoelectric materials provide much more electromechanical force due to the simple fact that they contain more piezoelectric material, maximum power generation is usually obtained with bulk materials rather than thin-film deposited piezoelectric materials.

4. Modeling techniques

Design optimization and analysis of acoustic energy harvesting devices require some form of modeling (analytical or numerical) to predict behavior. The basic equations of acoustics, which can be used to develop analytical models, are discussed in the fundamentals of acoustics section. Either analytical or numerical modeling, or a combination of both, may be appropriate for a given power transfer design depending on the structures, transduction techniques, and accuracy required. The lumped element modeling technique attempts to capture spatially distributed phenomena by discretizing elements into lumped components. This technique is conducive to creating equivalent electrical circuits. It is easy implement and thus can be used as the first modeling technique to predict the behavior of the system and to analyze the impact of each parameter on the system response. Numerical methods are also used, particularly when the complexity or required accuracy exceeds the capabilities of lumped element or simplified analytical models. It is important to note that lumped element models are one dimensional, and therefore other modeling techniques, such as numerical methods, should be considered for modeling the whole system in three dimensions to further investigate behavior.

4.1. Lumped element modeling (LEM)

A popular method to model acoustic signal or power transfer is by electrical circuit analogy. By developing equivalent lumped parameter components, this modeling method allows one dimensional analysis. It also enables simulation using a large infrastructure of circuit simulation tools [78]. As most acoustic energy harvesting systems use piezoelectric transducers, the classical Krimholtz, Leedom, and Matthae (KLM) [79] and Mason [80] equivalent circuit models are two attractive and common methods for modeling the piezoelectric plate architecture. Mason first developed an electrical equivalent circuit model by treating acoustic wave propagation as an electrical transmission line as illustrated in figure 8. KLM developed a similar equivalent circuit model, shown in figure 9, in part to replace the negative capacitance, which is not a physical device, in the Mason model. However, it has been shown that these two models produce equivalent results [81] and can be used interchangeably. These models can be treated as a starting point to develop a full model with all the system constraints. The entire piezoelectric transducer with two electrodes on its largest faces is modeled as a frequency dependent three-port network. The models include one electrical port for applying or collecting electrical power, and two acoustical (or mechanical) ports for generating or receiving mechanical waves as shown in figures 8 and 9. In the
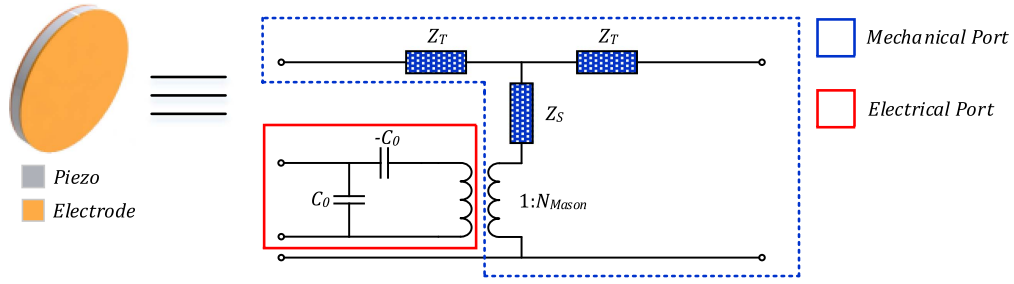
Figure 8. Mason equivalent model of a piezoelectric transducer.
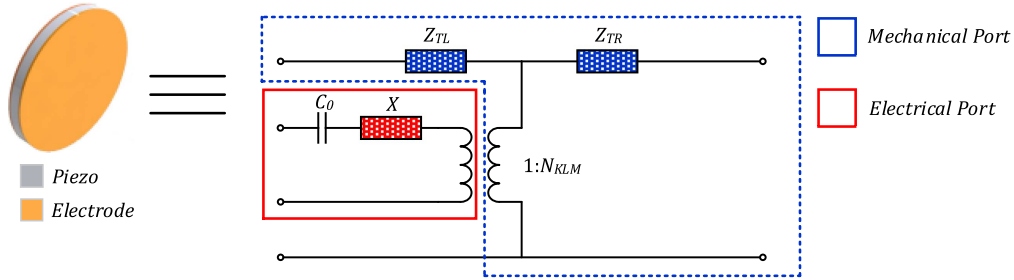
Figure 9. KLM equivalent model of a piezoelectric transducer.

mechanical port, the acoustic impedances due to the two faces of the piezoelectric transducer are modeled as quarter wavelength transmission lines [82]. The effect of matching layers can also be modeled as an acoustic impedance in series with the acoustic impedances of the transmitter and the receiver. The piezoelectric transducers for these models are generally plates operating in thickness stretch mode, however, there are formulations for other very simple geometries [83].

The frequency dependent acoustic capacitance, X, will become zero when the system operates at the series resonance frequency f_r which is [82]:

$$f_r = \frac{c}{2d}, \tag{17}$$

where c is the acoustic velocity in the piezoelectric transducer, and d is its thickness. For a specific area of the piezoelectric material (A), it can be shown that the acoustic impedance is:

$$Z_0 = \rho A c = A\sqrt{\rho c_{33}^D}, \tag{18}$$

where c_{33}^D is the open circuit complex elastic stiffness. According to figure 9, C_0 represents the transducer capacitance. In other words, C_0 is the parallel-plate capacitance from the electrodes and is given by:

$$C_0 = \frac{\varepsilon_{33}^S \cdot \varepsilon_0 A}{d}, \tag{19}$$

where ε_0 is permittivity of free space, and ε_{33}^S is the clamped relative complex permittivity. An ideal transformer with a turn ratio of N is considered for modeling the transduction between electrical and mechanical domains. The turn ratio for the Mason and KLM models can be expressed as follows

[82]:

$$N_{\text{Mason}} = \frac{C_0}{h_{33}}, \tag{20}$$

$$N_{\text{KLM}} = \frac{1}{2\left(\dfrac{h_{33}}{\omega Z_0}\right)}\csc\left(\frac{kt}{2}\right), \tag{21}$$

where h_{33} is the piezoelectric pressure constant, defined by [82]:

$$h_{33} = k_t \sqrt{\frac{c_{33}^D}{\varepsilon_{33}^S \cdot \varepsilon_0}}, \tag{22}$$

where k_t is the electromechanical coupling coefficient. The other circuit parameters, shown in figure 8, for the Mason model are defined as [81]:

$$Z_T = iZ_0 \tan\left(\frac{kt}{2}\right), \tag{23}$$

$$Z_S = -iZ_0 \csc(kt). \tag{24}$$

The values for the impedance elements of KLM model, shown in figure 9, can be given by [81]:

$$Z_{\text{TL}} = Z_0 \left[\frac{Z_L \cos\left(\dfrac{kt}{2}\right) + iZ_0 \sin\left(\dfrac{kt}{2}\right)}{Z_0 \cos\left(\dfrac{kt}{2}\right) + iZ_L \sin\left(\dfrac{kt}{2}\right)} \right], \tag{25}$$

$$Z_{\text{TR}} = Z_0 \left[\frac{Z_R \cos\left(\dfrac{kt}{2}\right) + iZ_0 \sin\left(\dfrac{kt}{2}\right)}{Z_0 \cos\left(\dfrac{kt}{2}\right) + iZ_R \sin\left(\dfrac{kt}{2}\right)} \right], \tag{26}$$
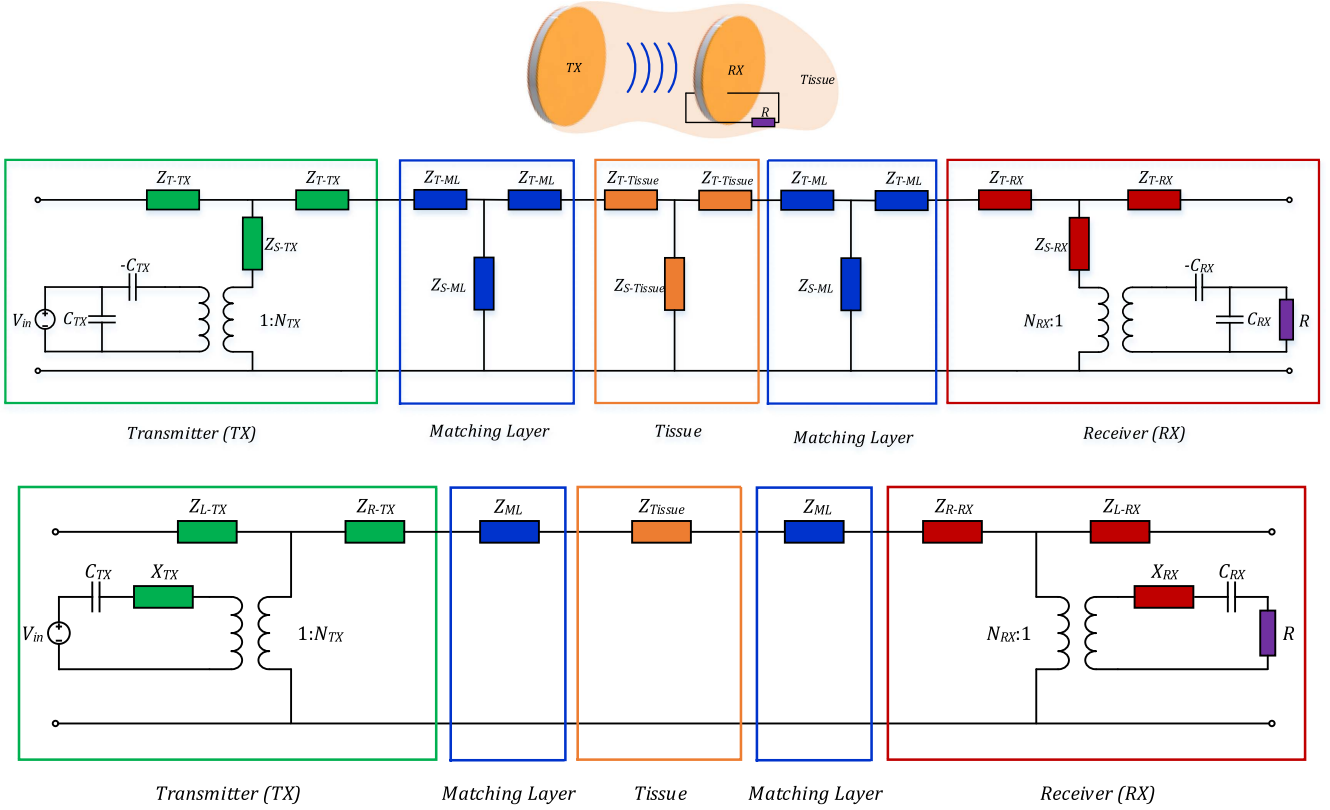
Figure 10. Complete LEM model for an acoustic power transfer system using the Mason (top) and KLM (bottom) models.

$$X = iZ_0 \left(\frac{h_{33}}{\omega Z_0} \right)^2 \sin \left(\frac{kt}{2} \right), \tag{27}$$

where Z_L and Z_R are the load impedance on left and right acoustic ports, respectively. The output power of the system, which is delivered to the load R, can be calculated by using the Thevenin equivalent model and assuming operation at the resonance frequency. In the Thevenin equivalent model, there is an output impedance $Z_{out} = 1/j\omega C_{RX}$, where C_{RX} is the capacitance (i.e. C_0) of the receiver. The load R is the electrical load impedance at the receiver. Therefore, the power can be derived as follows [82]:

$$P_{out} = \frac{1}{2C_{RX}} \left(\mu T \cdot N \cdot \frac{R}{R + Z_{out}} \right)^2 \cdot f_r, \tag{28}$$

where $T \approx 2 \left| Z_{Receiver} \right| \times c$ and μ is the tissue attenuation ($\mu = e^{-2\alpha x}$, α is the attenuation coefficient and x is the depth of the implant). $Z_{Receiver}$ is the acoustic impedance of the receiver in the mechanical port. Finally, knowing the C_0 of the transmitter, or C_{TX}, the theoretical power efficiency (η) is defined as [82]:

$$\eta = \left| \frac{P_{out}}{P_{in}} \right| = \frac{\left(\mu T \cdot N \cdot \dfrac{R}{R + Z_{out}} \right)^2}{C_{TX} C_{RX} V_{in}^2}, \tag{29}$$

where P_{out} and P_{in} are the electrical output power delivered to the load and the electrical input power to the transmitting

transducer, respectively. The complete equivalent circuits of an APT system using the Mason and KLM models are illustrated in figure 10.

4.2. Numerical approaches

Huygens principle is one approach to calculating the pressure generated by an ultrasound transducer at some location away from the transducer. Using this principle, each vibrating point on the surface of the transmitter is considered as the center of a new disturbance which acts as a point source emitting a spherical wave. It is assumed that propagation from these sources is forward. For a circular piston transmitter with radius a, the total acoustic pressure at an observation point on the acoustic axis with distance x from transmitter due to radiation from all incremental areas ds is [84]:

$$p = -j\rho_0 u f \int_0^{2\pi} \int_0^a \frac{e^{j\frac{\omega}{c_0}(l - c_0 t)}}{l} r \, dr \, d\varphi, \tag{30}$$

where r is the distance from the origin to ds, u is the particle velocity at ds, and l is the distance from each incremental area to the observation point, shown in figure 11 and calculated by:

$$l = \sqrt{r^2 + x^2}. \tag{31}$$
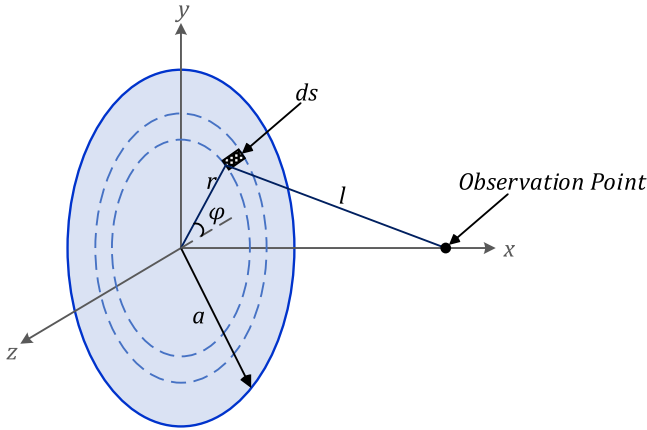
Figure 11. Geometry of a circular transmitter.

By integrating over the surface of the transmitter, the pressure at the observation point can be derived as:

$$
\begin{aligned}
p = (-2j\rho_0 c_0 u)&\left[\cos\left(\frac{\omega}{2c_0}(\sqrt{a^2+x^2}+x)\right)\right.\\
&\left.+j\sin\left(\frac{\omega}{2c_0}(\sqrt{a^2+x^2}+x)\right)\right]e^{-j\omega t}\\
&\times\sin\left(\frac{\omega}{2c_0}(\sqrt{a^2+x^2}-x)\right).
\end{aligned}
\tag{32}
$$

Finite element method (FEM) simulations are implemented in order to validate design concepts and to provide useful physical insights. Moreover, when using these techniques, one can straightforwardly carry out design optimization to improve the output voltage or to reduce device size. There are several works in the literature which make use of commercial FEM software such as COMSOL. As these problems deal with several areas of physics, including acoustics, solid mechanics, and piezoelectricity, COMSOL seems to be a good candidate since it has many features useful in solving multi-physics problems.

Ozeri *et al* used COMSOL to carry out a 2D axisymmetric simulation [35, 36]. Their simulation model included the piezoelectric element with its acoustic matching layer. Simulations were done for a maximum propagating distance of 50 mm surrounded by a thin perfectly matched layer to avoid reflections. Other works include the use of COMSOL to extract the effective acoustic impedance of the receiver in order to include the effect of resonance shift in the KLM model [66].

Shahab *et al* [85, 86] used finite element simulations to compare to an analytical model for ultrasonic power transfer. Their presented analytical model is a continuum model that is capable of modeling a cylindrical receiver excited by a spherical wave source. The simulation was carried out in COMSOL to explore the 3D behavior of the receiver in water under harmonic excitation. The longitudinal tip displacement and the output voltage of the receiver were both computed using the analytical and FEM model and were compared to

each other. They report that good agreement was observed in these results.

ANSYS, another computer aided engineering software tool, is also used by some researchers to model their devices. Hori *et al* developed a two-dimensional axisymmetric model in ANSYS in order to investigate optimal design parameters. Their model includes the piezoelectric element and the matching layer, and the propagating medium is assumed to be water and modeled as an infinite medium [87]. Other published works use ANSYS for modeling only a part of the power transfer system. For instance, He *et al* [88] simulated their MEMS device in ANSYS to find the resonance frequency of the receiver.

k-Wave is an open source Matlab toolbox designed for the time-domain simulation of propagating acoustic waves in 1D, 2D, or 3D [89]. The toolbox can model both linear and nonlinear wave propagation based on numerical models. It is also capable of performing photoacoustic reconstruction and modeling elastic wave propagation in solids.

The modeling techniques discussed thus far are primarily geared toward piezoelectric transducers. However, other transduction mechanisms, most notably electrostatics, have been used for APT in the context of IMDs. Capacitive micromachined ultrasound transducers (CMUTs) have been employed to receive the mechanical wave and convert it to electrical energy. For instance, Fowler *et al* developed a CMUT device and implemented the modeling in Coventor-Wave, which is a MEMS design software package for finite element analysis [90].

Table 3 presents a summary of different modeling techniques used by researchers for modeling APT for implants. Basic equations and analytical methods, in general, are not attractive to model complex systems. LEM techniques are still popular as they are easy to implement and can model the whole APT system as a circuit. Among numerical methods, COMSOL appears to be to the most widely used among researchers. Finally, the finite difference time domain (FDTD) method also provides full-wave solutions to the propagation problem [91]. Mo *et al* used this technique to study the effect of misalignment of the ultrasound transmitter and receiver on the power transmission efficiency [92].

5. Reported devices

Several research groups are currently active in the field of APT for bio-medical devices, and a wide range of devices have been reported. Here we summarize some of the key developments and trends, with examples for each of the main device types.

5.1. Electrostatic transduction

Significantly less work has been reported on electrostatic transduction than on piezoelectric transduction, possibly because of the lower achievable output power. These devices most often employ a comb drive to generate electrical energy from a base vibration. Depending on the actuation

Table 3. Different modeling techniques used by published works.

Article		Analytical		LEM		Numerical				
Author	Year/Ref	Basic equations	Continuum	Mason	KLM	Huygens	COMSOL	ANSYS	CoventorWare	FDTD
Arra	2007/[56]	●								
Ozeri	2010/[35]	●			●		●			
Denisov	2010/[29]			●						
Zhu	2010/[74]			●					●	
Shigeta	2011/[93]			●				●		
Ozeri	2012/[94]				●		●			
Seo	2013/[65]				●					
Mo	2013/[92]									●
Hori	2013/[87]			●				●		
Fowler	2013/[95]								●	
Lee	2013/[96]					●				
Lee	2014/[97]					●				
Fowler	2014/[90]								●	
He	2014/[88]							●		
Shahab	2014/[98]		●				●			
Ozeri	2014/[70]	●			●		●			
Chou	2014/[99]				●		●			
Fowler	2015/[100]								●	
Charthad	2015/[45]				●		●			
Christensen	2015/[28]	●		●	●					
Song	2015/[82]				●					
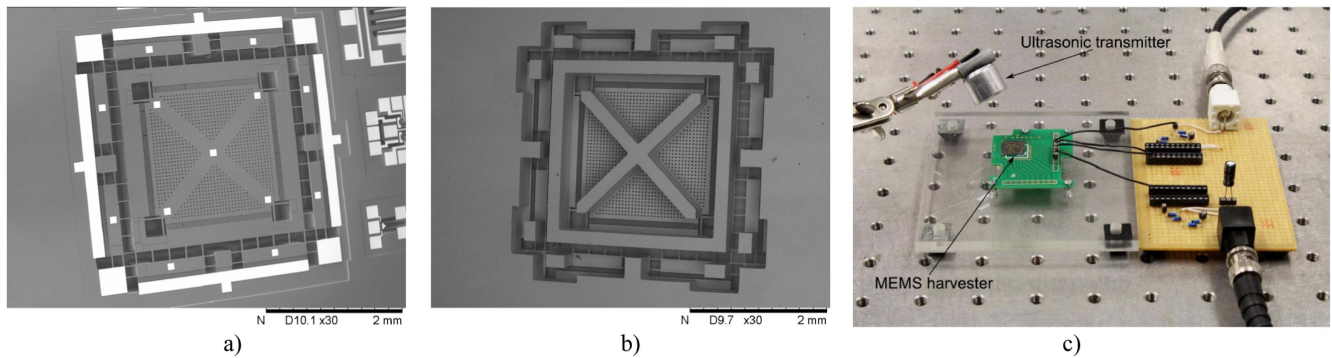
Figure 12. (a) SEM image of fabricated MEMS energy harvester, (b) underside of fabricated harvester, (c) photo showing MEMS harvester experimental setup [90].

mechanism, there are three types of electrostatic harvesters including in-plane gap closing, in-plane overlap, and out-of-plane gap closing electrostatic generators [3]. For the in-plane gap closing generators, the actuation direction can be parallel or perpendicular to the plane. The highest power density can be achieved from in-plane gap closing electrostatic generators since their design is more manageable and less prone to detrimental in-plane rotation [101].

Moheimani *et al* one of the only groups publishing on electrostatic transduction for IMDs, have reported a MEMS device that vibrates due to incoming ultrasonic waves for extracting ultrasonic energy via electrostatic comb-finger transducers. For a proof of concept in 2010, they developed a two degree-of-freedom (2-DOF) device capable of generating power of up to 21.4 nW for an air gap of 5 mm [74, 102]. The fabrication process was based on a commercial silicon-on-insulator (SOI) MEMS process with a 25 μm thick device layer and minimum gap of 2 μm which is fully presented in [103]. In 2013, they designed and fabricated a 3-DOF CMUT device, shown in figure 12, that has three resonance modes in three different translational directions so that ultrasonic energy can be harvested regardless of the device's orientation relative to the exciting ultrasonic transmitter [90, 95]. The resonance frequency of their fabricated device was around 25 kHz, and the device can generate 24.7, 19.8, and 14.5 nW in each of three directions from ultrasonic waves generated by an external transmitter. Adding a rotational mode to their device improved the total output power in two directions [100]. This device provided average power outputs of 50.9, 60.6, and 14.3 nW in three directions. Although these power values are still low, they may be useful for certain implanted medical devices including pacemakers, neurostimulators, and drug pumps.

5.2. Piezoelectric transduction

5.2.1. Plate structure. A plate structure for transmitting and receiving power is most commonly used in the literature. In 2001, Kawanabe *et al* developed a device with two piezo discs [104]. The rectified output power of their devices can be used to charge the battery of a cardiac pacemaker. They also studied the temperature increase in the body due to the input power since their input power is relatively high (0.5 and

1.7 W). For an input power of 1.7 W, the temperature inside the skin started to increase from about 35 °C–36.5 °C in 25 min. A power of 340 mW could be transferred with their device with an efficiency of 20%. The same research group presented a modified structure with two pairs of piezo oscillators [105]. This newer device increased the information transmission rate from 600 bps to 9.5 Kbps. Although it applied six times higher input power compared to their previous work, they have not studied the resulting temperature change inside the body. The efficiency of the device was the same as their previously reported device which results in higher output power and voltage.

In order to power implantable devices with a power level up to a few hundred mW, Ozeri *et al* developed an ultrasonic receiver operating at 673 kHz [35]. The transducers contain matching layers consisting of two layers of cyanoacrylate and graphite. Their models include the effect of the matching layers. They investigated the output power for different receiver depths ranging from 5–30 mm through water and pig muscle in a test tank. They also studied the effect of lateral misalignment of the transducers. According to their results, the efficiency of the power transfer through pig muscle is much smaller than the efficiency through water since pig muscle has more than two orders of magnitude higher attenuation compared to water. To improve the efficiency of their system, Ozeri *et al* presented a transducer based on a kerfless transmitter with Gaussian radial distribution of its radiating surface velocity [36]. The efficiency increased from 27% to 39.1% by partitioning the transmitter electrode in to five concentric rings in order to have six equal area concentric elements.

Lee *et al* [96] describe an ultrasound power transfer system in which the frequency is adjusted in order to maximize the power transfer efficiency for different tissue thicknesses. For instance, at a 23 mm depth, the maximum efficiency was achieved at 255 kHz which is 21% while the maximum power transfer efficiency at a 45 mm depth was 13.8% at 265 kHz.

Ziaie *et al* developed an implantable micro-oxygen generator with the total size of 1.2 mm × 1.3 mm × 8 mm [46]. Instead of PZT disks, they used a PZT bar whose dimensions are chosen in a way to compromise between the

size of the implant and body attenuation. The whole device was covered by a 5 μm-thick parylene layer for biocompatibility assurance. An implantable pressure sensing system was also presented by this group [106]. Their fabricated prototype, which was used for measuring bladder pressure, has a diameter of 8 mm and a length of 40 mm. A speaker with input power of 11.7 W was used to generate an acoustic wave resulting in an output power of 16 μW. It should be noted that APT under angular misalignments of the receiver was also studied.

Mazzilli *et al* have also worked on ultrasound wireless energy transfer for implantable medical devices. They used focused transducers in order to narrow the ultrasonic beam in the near field and increase the output power intensity. In 2010, they presented a power transfer system with a single element focused transducer having a diameter of 50 mm and a radius of curvature of 50 mm as the transmitter, and a receiver with a diameter of 6.35 mm [107]. Operating at a frequency of 1.033 MHz, they achieved a power transfer of 3 mW with an electro-acoustic efficiency of 10%. In another work, they used a plate array for the receiver and a spherical array for the transmitter [59]. A spherical transducer array made up of 64-elements was employed for the transmitter to focus the transmitting beam. The receiver was an array of six elements, each with an area of 1 mm $\times$ 5 mm. The output power of this device was 28 mW with the efficiency of 1.6%.

5.2.2. Diaphragm structure. The plate structure is an efficient structure as long as the piezoelectric device can be relatively thick. For optimal performance, the piezoelectric thickness should be half the acoustic wavelength in the piezoelectric material. The acoustic wavelength in PZT at 1 MHz is approximately 4 mm. In order for the piezoelectric element to be much thinner (significantly below 1 mm) and operate efficiently, the frequency must go up. However, as the frequency goes up, so does the absorption in tissue [108]. For this reason, some researchers are studying the use of piezoelectric devices with alternative, more compliant, geometries as power receivers. This will enable a thinner device to be used efficiently at lower frequencies resulting in increased overall efficiency. It should be noted that compliant diaphragm structures are used as ultrasound transceivers, external to the body, for imaging applications [109]. However, the imaging application is significantly different than an implanted power receiver.

Lee *et al* developed a diaphragm based PZT receiver and conducted acoustic transmission experiments with it using streaky pork at four different depths [110]. They achieved a maximum power output of 0.15 μW at a resonance frequency around 1.5 kHz. As part of this work, they developed a novel customized PZT deposition chamber based on a jet-printing method for implantable power harvesters. The thickness of the deposited PZT is about 10 μm, which is achieved by depositing PZT powders with particle size smaller than 1 μm in diameter which were put in a continuously vibrating powder container. The same group also studied the effect of packaging on the output voltage [111, 112]. Two different

spherical and cubic packages with the same cross section were considered. The packaged and unpackaged devices were tested in different mediums such as air, fatty, and muscular pork tissue. The maximum power transmission efficiency was achieved when using the spherical package in the muscular layer of the streaky pork.

As stated earlier, the integration of piezoelectric materials to microsystems suffers from several weaknesses of additive thin-film deposition methods. Current deposition methods for piezoelectric materials on a silicon wafer such as sol–gel [113], sputtering [114], screen printing [115], and pulsed laser deposition [116] result in lower piezoelectric material performance compared to bulk PZT. Furthermore, the PZT films are thin (typically <5 μm). Thicker films would result in higher power generation capability. Some other issues include high-temperature deposition steps and issues related to film uniformity and process reliability [77]. Therefore, alternative fabrication methods have been introduced to fabricate thick film piezoelectric receivers for energy harvesting and power transfer applications.

Aktakka *et al* [77, 117, 118] developed a low-temperature, aligned, wafer scale bonding process to integrate commercially available piezoelectric substrates on silicon, which appears to be an appropriate process for fabricating implanted piezoelectric receivers. They have presented a low-temperature (200 °C) gold–indium bonding process for bulk PZT wafers on Si wafers. PZT films with a thickness of 10 μm were achieved using mechanical lapping and polishing. They report the fabrication of both square and circular shaped PZT diaphragms with three different sizes.

He *et al* [88] used a MEMS fabrication processes to fabricate the ultrasonic PZT receiver for implantable microdevices shown in figure 13. The fabrication process, [119], makes use of a low-temperature bonding technique using conductive epoxy resin, after which the bulk PZT is thinned using mechanical lapping. As they developed a device with a PZT layer with a thickness of 40 μm through bonding and mechanical thinning methods. The operating frequency is about 40 kHz which is considerably lower than reported plate structures.

Christensen and Roundy [28] have recently carried out a comparative study between plate and diaphragm piezoelectric receivers for implantable devices. The results of their modeling, which were validated on larger devices, indicate that more power can generally be achieved by a diaphragm structure compared to a plate structure for diameters of approximately two millimeters and smaller. They also concluded that the diaphragm is significantly less sensitive to changes in implant depth, alignment, and orientation.

5.3. Power transfer performance metrics

We consider three different performance metrics, or figures of merit, in comparing different devices. Efficiency can be defined as the ratio of generated output electrical power from the receiver to electrical input power applied to the transmitter and is expressed as a percentage. Although it can give good insight into the effectiveness of power transfer, it does not
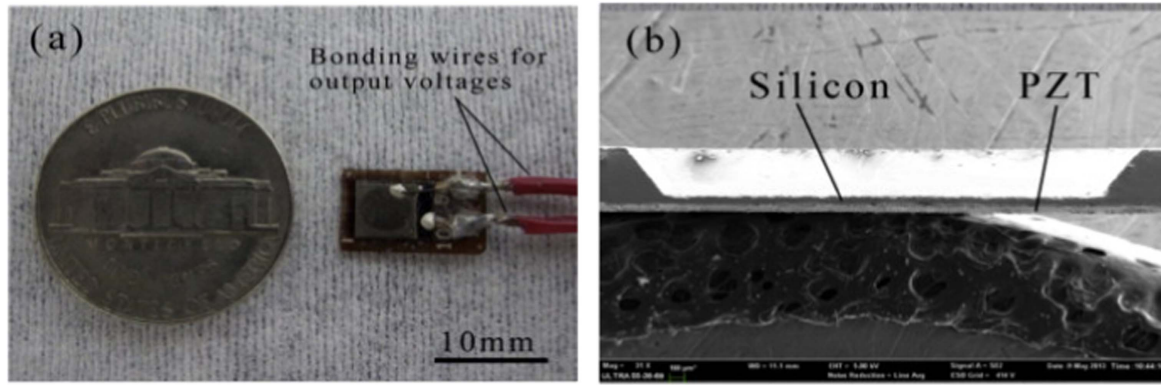
Figure 13. (a) Optical image of receiver and (b) SEM image of the cross-section of the receiver [88].

consider the dependence of input and output power to the device size. In other words, the best efficiency is usually achieved when the transmitter and receiver have the same size. But, this may not always be desirable. Furthermore, in many cases the critical issue is the power generated by, and the size of, the receiver, not the overall efficiency. Therefore, output power intensity, the ratio of output power to the receiver area, is another useful metric to consider.

The ratio of the size of receiver to the size of transmitter can also affect the efficiency. For example, if the transmitter is large, and the receiver is small, much of the acoustic energy transmitted may not be captured by the receiver. In this case, the efficiency will be low, but the power intensity at the receiver could still be high. Furthermore, this situation may address the application of medical devices quite well. Therefore, we define an area normalized efficiency, η', as shown in (33) where the standard definition of efficiency is modified by the transmitter area (A_{TX}) and receiver area (A_{RX}). This is equivalent to the ratio of output power intensity to input power intensity. Consider the case in which the area of a small receiver is held constant as the area of a larger transmitter is increased. If the transmit power intensity (P_{in}/A_{TX}) is constant, both the transmit area and input power will go up. However, received power will stay more or less constant. Efficiency, however, would go down. Thus, efficiency seems to unfairly penalize the small receiver. However, in this case, area normalized efficiency, η', would stay the same, which reflects the fact that the receiver has not changed. Thus η' is designed to address this shortcoming of efficiency as a metric when the transmitter is large and the receiver is small

$$\eta' = \frac{P_{out}}{P_{in}} \times \frac{A_{TX}}{A_{RX}} \times 100. \tag{33}$$

There are some cases in which the area normalized efficiency cannot be used properly unless several factors are taken in to account. If the transmitter diameter becomes too small compared to the wavelength, less energy will be captured by the receiver due to less radiation directivity. This can also cause the medium to reflect to the transmitter as a reactive load resulting in less radiated real power. Moreover, if the ratio of the diameter to the thickness is too small, then

there would not be a pure vibration mode for the transmitter and the acoustic wave radiates in the medium in coupled modes which limits the efficiency. These issues are primarily features of relatively small transmitters. In that case, area normalized efficiency may not be an appropriate metric.

Table 4 provides a list of publications from the last 15 years including their important parameters. Only papers reporting experimental results are included in the table, and they are presented in the order of their publication year. The research team is identified by the first author on the corresponding paper. A few observations about these publications can be made.

The number of publications considering the diaphragm as the RX transducer are sparse compared to those considering the plate. Furthermore, none of them (with the exception of Christensen's work [28]) have compared the power generation potential of the plate and diaphragm when used as small, deeply implanted RX.

The vast majority of publications address, to some extent, the effect of RX depth on power generation. However, only a few of the publications take into consideration RX power sensitivity due to alignment and orientation. The papers that do address these effects present them in a narrow scope offering only experimental or simulation data for their particular device. This information is useful for the devices in question, but provides very little insight into other TX–RX systems. Mo, [92], provides the most information on alignment and orientation using FDTD simulations, but the analysis is still lacking in that it does not provide details about the effect that frequency and RX diameter have on RX power sensitivity.

Figure 14 plots the number of publications by year. It is clear that the number of publications for acoustic power transmission for implants has increased dramatically in recent years. Figure 15 shows the efficiency versus the area of the receiver for the reported devices with the best efficiency value of 50.4%. Larger receiver devices generally have higher efficiency. This may be because smaller receiver devices tend to have transmitters which are much larger than the receiver while for large devices the TX and RX are usually the same size. Thus small receiver devices are perhaps unfairly penalized by the efficiency metric. The area normalized efficiency

Table 4. Acoustic power transfer in implantable devices.

Author	Year/Ref	Transduction mechanism	Medium	Efficiency (%)	Input power (mW)	Output power (mW)	Operating frequency (kHz)	TX area (cm²)	RX area (cm²)	TX size (cm³)	RX size (cm³)	Depth (mm)	Power density (mW cm⁻³)	Power Intensity (mW cm⁻²)	η' (%)
Kawanabe	2001/[104]	PZT-plate	Goat Tissue	20	1700	340	1000	7.07	7.07	3.534	3.534		96.21	48.09	20
Suzuki	2002/[105]	PZT-plate	Skin	20	10 500	2100	1000	7.07	7.07	1.414	1.414	40	1485.15	297.03	20
Arra	2007/[56]	PZT-plate	Water	25	250	62.5	840	7.07	4.91	1.718	1.19	100	52.52	12.73	36
Lee	2007/[110]	PZT-diaphragm	Pork tissue	0.01	1.5	0.000 15	1.5		0.38		0.031	25	0.005	0.0004	
Shigeta	2009/[120]	PZT-plate	Water	0.35	229	0.8	4200	2.688	9.62	0.174	0.467	70	1.71	0.0832	0.098
Zhu	2010/[74]	Electrostatic	Air			2.14×10^{-5}	38.78					5			
Shih	2010/[111]	PZT-diaphragm	Pork tissue	0.015	1.23	0.000 18	35		0.38		0.031	60	0.0058	0.00047	
Ozeri	2010/[35]	PZT-plate	Pork tissue	27	260	70	673	1.77	1.77	0.53	0.53	5	132.1	39.55	27
Ozeri	2010/[36]	PZT-plate	Pork tTissue	39.1	256	100	650	1.77	1.77	0.53	0.53	5	188.67	56.50	39.1
Mazzilli	2010/[107]	PZT-plate	Water	10	30	3	1033	19.63	0.316			50		9.49	621.2
Shigeta	2011/[93]	PZT-plate	Water	50.4	20	10.08	1200	15.2	15.2	2.86	2.86	32.3	3.52	0.66	50.4
Larson	2011/[57]	PZT-plate	Rat hind limb	0.022	2300	0.51	1000	5.31	0.01		0.001	120	510	51	11.68
Maleki	2011/[46]	PZT-plate	Tissue			0.33	2150	52.4	0.05	5.345	0.0051	30	64.7	6.60	
Sanni	2012/[58]	PZT-plate	Water	1	800	8	200	0.78	0.78	0.078	0.078	70	102.56	10.26	1
Sanni	2013/[37]	PZT-plate	Water	0.2	488	0.976	200	0.78	0.78	0.078	0.078	80	12.51	1.25	0.2
Lee[a]	2013/[96]	PZT-plate	Pork tissue	21	15.5	3.25	255	19.63	19.63	15.7	15.7	23	0.21	0.17	21
Charthad	2014/[45], [121]	PZT-plate	Chicken breast			0.1	1000		0.01		0.0014	30	71.43	10	
Kim	2014/[106]	PZT-plate	Pork tissue	1.4×10^{-4}	11 700	0.016	0.35		0.4		0.0152	100	1.05	0.04	
He	2014/[88]	PZT-diaphragm	Pork tissue	0.096	51	0.049	40.43	23.76	0.1			22		0.49	22.81
Mazzilli	2014/[59]	PZT-plate	Water	1.6	1750	28	1000	21.3	0.3			105		93.33	113.6
Ozeri	2014/[70]	PZT-plate	Water			20	765	1.77	1.77	0.53	0.53	150	37.73	11.30	
Shmilovitz	2014/[122]	PZT-plate	Water			35	720	1.77	1.77	0.53	0.53	85	66.04	19.77	
Chou	2014/[99]	PZT-plate	Oil	1				0.15	0.15	0.046	0.046	25			1
Lee[a]	2014/[97]	PZT-platePZT-plate	Pork tissue	18	15.5	2.6	250	19.63	19.63	15.7	15.7	18	0.165	0.13	18
Song[a]	2015/[82]	PZT-plate	Water	0.15	7704	12	1150	10.7	0.08	2.14	0.016	200	750	150	20.06
Seo	2015/[66]	PZT-plate	Water				10 000					20			
Fang[a]	2015/[123]	PZT-plate	Pork tissue			3	3500		1.1		0.066	4		2.73	
Zhou	2015/[124], [125]	PZT-plate	Water				672		1.28		0.256	67			
Christensen[a]	2015/[28]	PZT-plate	Water	1.95	62.5	1.22	1058	1.29	1.29	0.24	0.24	40	5.08	0.94	1.95
		PZT-diaphragm	Water	0.016	62.5	0.001	3.5	1.29	0.5	0.24	0.005	40	0.2	0.002	0.041
Vihvelin[a]	2016/[126]	PZT-plate	Porcine tissue	25			1300	0.5	0.5	0.06	0.06	5			25

Table 4. (Continued.)

Author	Year/Ref	Transduction mechanism	Medium	Efficiency (%)	Input power (mW)	Output power (mW)	Operating frequency (kHz)	TX area (cm^2)	RX area (cm^2)	TX size (cm^3)	RX size (cm^3)	Depth (mm)	Power density (mW cm^{-3})	Power Intensity (mW cm^{-2})	η' (%)
Radziemski[a]	2016/ [127]	PZT-plate	Porcine tissue	22	2000	440	1000	4.91	4.91			5		89.61	22
Seo	2016/ [128]	PZT-plate		Tissue	0.12		1850		0.005			8.8			

Article

[a] Best reported performance.
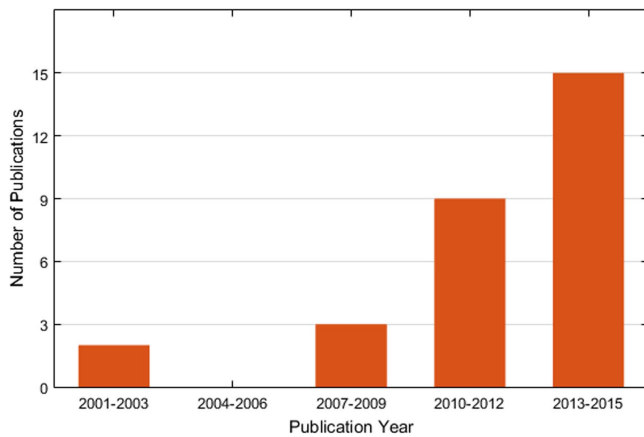
Figure 14. Number of publications of reported devices over the last 15 years.
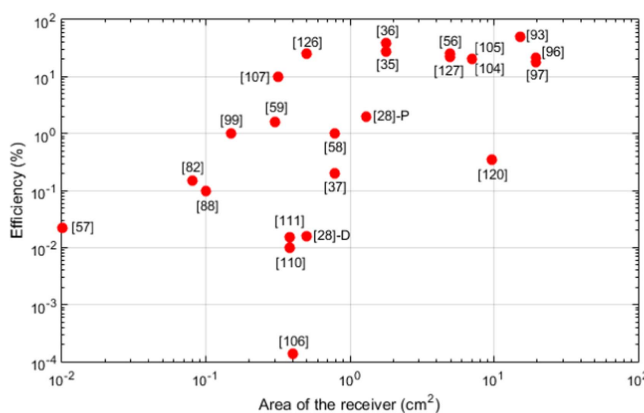
Figure 15. Efficiency versus area of the receiver for reported devices.
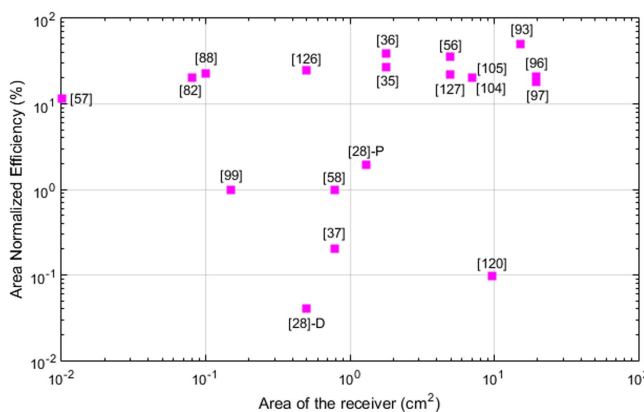
Figure 16. Area normalized efficiency versus area of the receiver for reported devices.

versus the receiver area is plotted in figure 16. It is clear that once normalizing for area, the trend of larger receivers exhibiting better efficiency goes away. One possible explanation is that the trend is due more to the size match of the transmitter and receiver rather than poor transduction performance on the part of the receiver. It should be noted that those devices with focused transducers are taken out from this figure since they result in area normalized efficiencies greater than 100%. Figure 17 shows the operating frequency of these
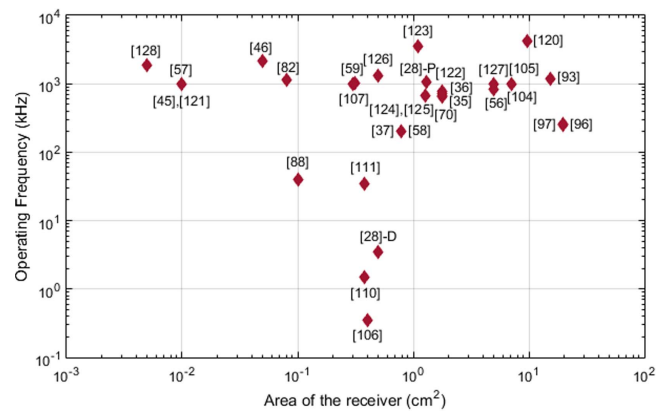
Figure 17. Operating frequency versus area of the receiver for reported device.

devices plotted against receiver size. The frequency values are mostly around 1 MHz. This is likely due to multiple factors which could include device size (half-wavelength thickness at 1 MHz is about 2 mm), and availability of commercial transducers operating at this frequency.

6. Conclusion

Implantable medical devices are now being widely used in order to monitor physiological parameters useful for medical diagnosis, provide therapeutic functions, and collect data for scientific studies. Although batteries have been used to power IMDs, they now consume a substantial portion of the device volume as the sizes of these devices have become smaller. Efforts to reduce overall implant size require focus on a suitable replacement for batteries, as battery technology has not kept pace with ever-shrinking modern electronics. Furthermore, batteries, having a fixed total energy, require replacement and, inevitably, surgery to carry out this replacement. Hence, further miniaturization, and therefore reduced trauma to the patient, will be greatly accelerated by the development of robust wireless powering techniques. Such wireless powering methods can miniaturize existing, and enable new real-time health monitoring and fuel more personalized and preventative healthcare. Common alternatives in the literature include RF, inductive coupling, vibrational energy harvesting, and APT.

APT is capable of obtaining more power with smaller devices compared to other methods. This is due to the fact that it has shorter wavelengths, which results in smaller sized receivers. Moreover, it exhibits lower attenuation in human tissue resulting in deeper penetration. This paper has covered the basic fundamentals of acoustic power transmission, discussed common modeling techniques, and reviewed the current state of the art as reported in the scientific literature. Modeling approaches can generally be broken down into analytical mathematical models, 1D lumped element models such as the Mason and KLM equivalent circuit models, and numerical finite element techniques. All methods are used in the scientific literature to provide design insight and

performance estimates. Analytical models have typically not dealt with issues of alignment or orientation. To fill the system modeling gap, there is still a need for a comprehensive design scheme that addresses a TX–RX system for differing architectures and diameters and considers power sensitivity due to depth, alignment, and orientation.

Reported implementations of APT for medical devices are showing progress on miniaturization. Among different transduction mechanisms, piezoelectric transduction seems to be more attractive since it can produce devices capable of generating higher power densities compared to electrostatic transduction. Although the piezoelectric plate structure can provide the required power for most implantable devices, a diaphragm structure may perform better for sub-mm size receivers especially implanted at large depths. Besides common metrics for comparing devices such as efficiency and power intensity, another performance figure of merit was defined and used in this paper for comparing APT for IMDs that is a function of device efficiency and also transmitter and receiver area. This area normalized efficiency does not appear to be a strong function of receiver size, indicating that very good acoustic power generation performance can be expected from very small devices.

Acknowledgment

References

[1] Wood M A and Ellenbogen K A 2002 Cardiac pacemakers from the patient's perspective *Circulation* **105** 2136–8

[2] Ledet E H, D'Lima D, Westerhoff P, Szivek J A, Wachs R A and Bergmann G 2012 Implantable sensor technology: from research to clinical practice *J. Am. Acad. Orthop. Surg.* **20** 383–92

[3] Lueke J and Moussa W 2011 MEMS-based power generation techniques for implantable biosensing applications *Sensors* **11** 1433–60

[4] Gerrish P, Herrmann E, Tyler L and Walsh K 2005 Challenges and constraints in designing implantable medical ICs *IEEE Trans. Device Mater. Reliab.* **5** 435–44

[5] Guiseppi-Elie A, Brahim S, Slaughter G and Ward K 2005 Design of a subcutaneous implantable biochip for monitoring of glucose and lactate *IEEE Sens. J.* **5** 345–55

[6] Troyk P R, DeMichele G A, Kerns D A and Weir R F 2007 IMES: an implantable myoelectric sensor *Annual Int. Conf. IEEE Engineering in Medicine and Biology—Proc.* pp 1730–3

[7] Wise K D, Anderson D J, Hetke J F, Kipke D R and Najafi K 2004 Wireless implantable microsystems: high-density electronic interfaces to the nervous system *Proc. IEEE* **92** 76–97

[8] Zumsteg Z S, Kemere C, Member S, Driscoll S O, Member S, Santhanam G, Ahmed R E, Shenoy K V and Meng T H 2005 Power feasibility of implantable digital spike sorting circuits for neural prosthetic systems *IEEE Trans. Neural Syst. Rehabil. Eng.* **13** 272–9

[9] Owens B 1986 *Batteries for Implantable Biomedical Devices* (New York: Plenum)

[10] Bock D C, Marschilok A C, Takeuchi K J and Takeuchi E S 2012 Batteries used to power implantable biomedical devices *Electrochim. Acta* **84** 155–64

[11] Akhtar F and Rehmani M H 2015 Energy replenishment using renewable and traditional energy resources for sustainable wireless sensor networks: a review *Renew. Sustain. Energy Rev.* **45** 769–84

[12] Wei X and Liu J 2008 Power sources and electrical recharging strategies for implantable medical devices *Front. Energy Power Eng. China* **2** 1–13

[13] Rapoport B I, Kedzierski J T and Sarpeshkar R 2012 A glucose fuel cell for implantable brain–machine interfaces *PLoS One* **7** 1–15

[14] Kerzenmacher S, Ducrée J, Zengerle R and von Stetten F 2008 Energy harvesting by implantable abiotically catalyzed glucose fuel cells *J. Power Sources* **182** 1–17

[15] Roundy S and Wright P 2004 A piezoelectric vibration based generator for wireless electronics *Smart Mater. Struct.* **13** 1131–42

[16] Nasiri A, Zabalawi S A and Jeutter D C 2011 A linear permanent magnet generator for powering implanted electronic devices *IEEE Trans. Power Electron.* **26** 192–9

[17] Chen H, Liu M, Jia C and Wang Z 2009 Power harvesting using PZT ceramics embedded in orthopedic implants *IEEE Trans. Ultrason. Ferroelectr. Freq. Control* **56** 2010–4

[18] Karami M and Inman D 2012 Powering pacemakers from heartbeat vibrations using linear and nonlinear energy harvesters *Appl. Phys. Lett.* **100** 042901

[19] Karami M and Inman D 2011 Linear and nonlinear energy harvesters for powering pacemakers from heart beat vibrations *Proc. SPIE* **7977** 797703

[20] Hannan M A, Mutashar S, Samad S A and Hussain A 2014 Energy harvesting for the implantable biomedical devices: issues and challenges *Biomed. Eng. Online* **13** 79

[21] Cadei A, Dionisi A, Sardini E and Serpelloni M 2014 Kinetic and thermal energy harvesters for implantable medical devices and biomedical autonomous sensors *Meas. Sci. Technol.* **25** 12003

[22] Romero E, Warrington R O and Neuman M R 2009 Energy scavenging sources for biomedical sensors *Physiol. Meas.* **30** R35

[23] Ayazian S and Hassibi A 2011 Delivering optical power to subcutaneous implanted devices *2011 Annual Int. Conf. IEEE Engineering in Medicine and Biology Society* pp 2874–7

[24] Yang Y, Wei X-J and Liu J 2007 Suitability of a thermoelectric power generator for implantable medical electronic devices *J. Phys. D: Appl. Phys.* **40** 5790–800

[25] Ben Amar A, Kouki A B and Cao H 2015 Power approaches for implantable medical devices *Sensors* **15** 28889

[26] Kim A, Ochoa M, Rahimi R and Ziaie B 2015 New and emerging energy sources for implantable wireless microdevices *IEEE Access* **3** 89–98

[27] Paulo J and Gaspar P D 2010 Review and future trend of energy harvesting methods for portable medical devices *Proc. World Congress on Engineering* vol 2, pp 168–96

[28] Christensen D B and Roundy S 2015 Ultrasonically powered piezoelectric generators for bio-implantable sensors: plate versus diaphragm *J. Intell. Mater. Syst. Struct.* **27** 1092–105

[29] Denisov A and Yeatman E 2010 Ultrasonic versus inductive power delivery for miniature biomedical implants *2010 Int. Conf. on Body Sensor Networks* pp 84–9

[30] Shih Y, Shen T and Otis B 2011 A 2.3 W wireless intraocular pressure/temperature monitor *IEEE J. Solid-State Circuits* **46** 2592–601

[31] Ho J S, Yeh A J, Neofytou E, Kim S, Tanabe Y, Patlolla B, Beygui R E and Poon A S Y 2014 Wireless power transfer

to deep-tissue microimplants *Proc. Natl Acad. Sci. USA* **111** 7974–9

[32] O'driscoll S, Poon A and Meng T 2014 Wireless power transmission for implantable medical devices *US Patent* 8,634,928

[33] Waffenschmidt E and Staring T 2009 Limitation of inductive power transfer for consumer applications *13th European Conference on Power Electronics and Applications, 2009. EPE '09* pp 1–10

[34] Roes M G, Duarte J L, Hendrix M A and Lomonova E A 2013 Acoustic energy transfer: a review *IEEE Trans. Ind. Electron.* **60** 242–8

[35] Ozeri S and Shmilovitz D 2010 Ultrasonic transcutaneous energy transfer for powering implanted devices *Ultrasonics* **50** 556–66

[36] Ozeri S, Shmilovitz D, Singer S and Wang C C 2010 Ultrasonic transcutaneous energy transfer using a continuous wave 650 kHz Gaussian shaded transmitter *Ultrasonics* **50** 666–74

[37] Sanni A and Vilches A 2013 Powering low-power implants using PZT transducer discs operated in the radial mode *Smart Mater. Struct.* **22** 115005

[38] Lu X, Wang P and Niyato D 2015 Wireless networks with RF energy harvesting: a contemporary survey *IEEE Commun. Surv. Tutorials* **17** 757–89

[39] Lu X, Wang P, Niyato D, Kim D I and Han Z 2015 Wireless charging technologies: fundamentals, standards, and network applications *IEEE Commun. Surv. Tutorials* **18** 1413–52

[40] Shinohara N 2011 Power without wires *IEEE Microw. Mag.* **12** S64–73

[41] Walleczek J 1992 Electromagnetic field effects on cells of the immune system: the role of calcium signaling *FASEB J.* **6** 3177–85

[42] Meral I, Mert H, Mert N, Deger Y and Yoruk I 2007 Effects of 900 MHz electromagnetic field emitted from cellular phone on brain oxidative stress and some vitamin levels of guinea pigs *Brain Res.* **1169** 120–4

[43] Liao Y, Yao H, Lingley A, Parviz B and Otis B P 2012 A 3-CMOS glucose sensor for wireless contact-lens tear glucose monitoring *IEEE J. Solid-State Circuits* **47** 335–44

[44] Van Schuylenbergh K and Puers R 2009 *Inductive Powering: Basic Theory and Application to Biomedical Systems* (Netherlands: Springer)

[45] Charthad J, Weber M J, Chang T C and Arbabian A 2015 A mm-sized implantable medical device (IMD) with ultrasonic power transfer and a hybrid Bi-directional data link *IEEE J. Solid-State Circuits* **50** 1741–53

[46] Maleki T, Cao N, Hyun Song S, Kao C, Chu S, Ko A and Ziaie B 2011 An ultrasonically powered implantable micro-oxygen generator (IMOG) *IEEE Trans. Biomed. Eng.* **58** 3104–11

[47] Poon A, O'Driscoll S and Meng T 2010 Optimal frequency for wireless power transmission into dispersive tissue *IEEE Trans. Antennas Propag.* **58** 1739–50

[48] Food and Drug Administration 2008 'Guidance for Industry and FDA—Staff Information for Manufacturers Seeking Marketing Clearance of Diagnostic Ultrasound Systems and Transducers' Silver Spring US FDA

[49] O'Driscoll S, Poon A and Meng T H 2009 A mm-sized implantable power receiver with adaptive link compensation *2009 IEEE Int. Solid-State Circuits Conf.—Digest of Technical Papers* (doi:10.1109/ISSCC.2009.4977424)

[50] Jow U and Ghovanloo M 2007 Design and optimization of printed spiral coils for efficient transcutaneous inductive power transmission *IEEE Trans. Biomed. Circuits Syst.* **1** 193–202

[51] Kilinc E, Dehollain C and Maloberti F 2010 Design and optimization of inductive power transmission for

implantable sensor system *Proc. SM2ACD'10* (doi:10.1109/SM2ACD.2010.5672335)

[52] Kiani M and Ghovanloo M 2010 An RFID-based closed-loop wireless power transmission system for biomedical applications *IEEE Trans. Circuits Syst.* II **57** 260–4

[53] Kiani M, Kwon K and Zhang F 2011 Evaluation of a closed loop inductive power transmission system on an awake behaving animal subject *2011 Annual Int. Conf. of the IEEE Engineering in Medicine and Biology Society* (Piscataway, NJ: IEEE) (doi:10.1109/IEMBS.2011.6091887)

[54] Silay K, Dehollain C and Declercq M 2011 Inductive power link for a wireless cortical implant with two-body packaging *IEEE Sens. J.* **11** 2825–33

[55] Liu X, Berger J, Ogirala A and Mickle M H 2013 A touch probe method of operating an implantable RFID tag for orthopedic implant identification *IEEE Trans. Biomed. Circuits Syst.* **7** 236–42

[56] Arra S, Leskinen J, Heikkilä J and Vanhala J 2007 Ultrasonic power and data link for wireless implantable applications *2007 2nd Int. Symp. Wireless Pervasive Computing* (doi:10.1109/ISWPC.2007.342668)

[57] Larson P J and Towe B C 2011 Miniature ultrasonically powered wireless nerve cuff stimulator *2011 5th Int. IEEE/EMBS Conf. on Neural Engineering (NER)* (Piscataway, NJ: IEEE) (doi:10.1109/NER.2011.5910538)

[58] Sanni A, Vilches A and Toumazou C 2012 Inductive and ultrasonic multi-tier interface for low-power, deeply implantable medical devices *IEEE Trans. Biomed. Circuits Syst.* **6** 297–308

[59] Mazzilli F, Lafon C and Dehollain C 2014 A 10.5 cm ultrasound link for deep implanted medical devices *IEEE Trans. Biomed. Circuits Syst.* **8** 738–50

[60] Briand D, Yeatman E and Roundy S (ed) 2015 *Micro Energy Harvesting* (Weinheim: Wiley)

[61] Kinsler L and Frey A 2000 *Fundamentals of Acoustics* 4th edn (New York: Wiley)

[62] Nakamura K 2012 *Ultrasonic Transducers: Materials and Design for Sensors, Actuators and Medical Applications* (Amsterdam: Elsevier)

[63] Hu Y C, Liao P L, Shih W P, Wang X Y and Chang P Z 2009 Study on the acoustic impedance matching of human tissue for power transmitting/charging system of implanted biochip *2009 IEEE 3rd Int. Conf. on Nano/Molecular Medicine and Engineering, NANOMED 2009* (doi:10.1109/NANOMED.2009.5559087)

[64] Zaid T, Saat S, Yusop Y and Jamal N 2014 Contactless energy transfer using acoustic approach—a review *2014 Int. Conf. on. IEEE Computer, Communications, and Control Technology (I4CT)* (doi:10.1109/I4CT.2014.6914209)

[65] Seo D, Carmena J M, Rabaey J M, Alon E and Maharbiz M M 2013 Neural dust: an ultrasonic, low power solution for chronic brain–machine interfaces arXiv:1307.2196

[66] Seo D, Carmena J M, Rabaey J M, Maharbiz M M and Alon E 2015 Model validation of untethered, ultrasonic neural dust motes for cortical recording *J. Neurosci. Methods* **244** 114–22

[67] Inoue T, Ohta M and Takahashi S 1987 Design of ultrasonic transducers with multiple acoustic matching layers for medical application *IEEE Trans. Ultrason. Ferroelectr. Freq. Control* **34** 8–16

[68] Hill R and El-Dardiry S 1980 A theory for optimization in the use of acoustic emission transducers *J. Acoust. Soc. Am.* **67** 673–82

[69] Callens D, Bruneel C and Assaad J 2004 Matching ultrasonic transducer using two matching layers where one of them is glue *NDT E Int.* **37** 591–6

[70] Ozeri S and Shmilovitz D 2014 Simultaneous backward data transmission and power harvesting in an ultrasonic

transcutaneous energy transfer link employing acoustically dependent electric impedance modulation *Ultrasonics* **54** 1929–37

[71] American Institute of Ultrasound in Medicine and National Electrical Manufacturers Association 1998 *Acoustic Output Measurement Standard for Diagnostic Ultrasound Equipment* (Laurel, MD: American Institute of Ultrasound in Medicine)

[72] Culjat M O, Goldenberg D, Tewari P and Singh R S 2010 A review of tissue substitutes for ultrasound imaging *Ultrasound Med. Biol.* **36** 861–73

[73] Narayana P, Ophir J and Maklad N 1984 The attenuation of ultrasound in biological fluids *J. Acoust. Soc. Am.* **76** 1–4

[74] Zhu Y, Moheimani S O R and Yuce M R 2010 Ultrasonic energy transmission and conversion using a 2D MEMS resonator *IEEE Electron Device Lett.* **31** 374–6

[75] Banerji S, Goh W, Cheong J H and Je M 2013 CMUT ultrasonic power link front-end for wireless power transfer deep in body *2013 IEEE MTT-S Int. Microwave Workshop Series on RF and Wireless Technologies for Biomedical and Healthcare Applications (IMWS-BIO)* (doi:10.1109/IMWS-BIO.2013.6756176)

[76] Chen S N, Wang G J and Chien M C 2006 Analytical modeling of piezoelectric vibration-induced micro power generator *Mechatronics* **16** 379–87

[77] Aktakka E E, Peterson R L and Najafi K 2013 Wafer-level integration of high-quality bulk piezoelectric ceramics on silicon *IEEE Trans. Electron Devices* **60** 2022–30

[78] Leach W M 1994 Controlled-source analogous circuits and SPICE models for piezoelectric transducers *IEEE Trans. Ultrason. Ferroelectr. Freq. Control* **41** 60–6

[79] Krimholtz R, Leedom D A and Matthaei G L 1970 New equivalent circuits for elementary piezoelectric transducers *Electron. Lett.* **13** 398–9

[80] Mason W 1948 *Electromechanical Transducers and Wave Filters* (New York, Van Nostrand)

[81] Sherrit S, Leary S P, Dolgin B P and Bar-Cohen Y 1999 Comparison of the Mason and KLM equivalent circuits for piezoelectric resonators in the thickness mode *1999 Proc. Ultrasonics Symp.* vol 2 (doi:10.1109/ULTSYM.1999.849139)

[82] Song S H, Kim A and Ziaie B 2015 Omni-directional ultrasonic powering for mm-scale implantable biomedical devices *IEEE Trans. Biomed. Eng.* **62** 2717–23

[83] Redwood M 1961 Transient performance of a piezoelectric transducer *J. Acoust. Soc. Am.* **33** 527–36

[84] Ensminger D and Bond L 2011 *Ultrasonics: Fundamentals, Technologies, and Applications* (Boca Raton, FL: CRC)

[85] Shahab S, Gray M and Erturk A 2015 An experimentally validated contactless acoustic energy transfer model with resistive-reactive electrical loading *Proc. SPIE* **9431** 943105

[86] Shahab S, Gray M and Erturk A 2015 Ultrasonic power transfer from a spherical acoustic wave source to a free–free piezoelectric receiver: modeling and experiment *J. Appl. Phys.* **117** 104903

[87] Hori Y, Fujimori K, Tsuruta K and Nogi S 2013 Design and development of highly efficient transducer for ultrasonic wireless power transmission system *IEEE J. Trans. Electron. Inf. Syst.* **184** 337–43

[88] He Q, Liu J, Yang B, Wang X, Chen X and Yang C 2014 MEMS-based ultrasonic transducer as the receiver for wireless power supply of the implantable microdevices *Sensors Actuators* A **219** 65–72

[89] Treeby B and Cox B 2010 *k*-wave: MATLAB toolbox for the simulation and reconstruction of photoacoustic wave fields *J. Biomed. Opt.* **15** 021314

[90] Fowler A, Moheimani S O R and Behrens S 2014 An omnidirectional MEMS ultrasonic energy harvester for implanted devices *J. Microelectromech. Syst.* **23** 1454–62

[91] Hallaj I and Cleveland R 1999 FDTD simulation of finite-amplitude pressure and temperature fields for biomedical ultrasound *J. Acoust. Soc. Am.* **105** L7–12

[92] Mo C, Hudson S and Radziemski L J 2013 Effect of misalignment between ultrasound piezoelectric transducers on transcutaneous energy transfer *Proc. SPIE* **8688** 868814

[93] Shigeta Y and Hori Y 2011 Development of highly efficient transducer for wireless power transmission system by ultrasonic *2011 IEEE MTT-S Int. Microwave Workshop Series on Innovative Wireless Power Transmission: Technologies, Systems, and Applications (IMWS)* (doi:10.1109/IMWS.2011.5877115)

[94] Shaul O, Boaz S and Doron S 2012 Non-invasive sensing of the electrical energy harvested by medical implants powered by an ultrasonic transcutaneous energy transfer link *2012 IEEE Int. Symp. on Industrial Electronics (ISIE)* (doi:10.1109/ISIE.2012.6237251)

[95] Fowler A, Moheimani S O R and Behrens S 2013 A 3-DOF SOI MEMS ultrasonic energy harvester for implanted devices *J. Phys.: Conf. Ser.* **476** 012002

[96] Lee S Q, Youm W and Hwang G 2013 Biocompatible wireless power transferring based on ultrasonic resonance devices *Proc. Meet. Acoust.* **19** 030030

[97] Lee S, Youm W, Hwang G, Moon K S and Ozturks Y 2014 Resonant ultrasonic wireless power transmission for bio-implants *Proc. SPIE* **9057** 90570J

[98] Shahab S and Erturk A 2014 Contactless ultrasonic energy transfer for wireless systems: acoustic-piezoelectric structure interaction modeling and performance enhancement *Smart Mater. Struct.* **23** 125032

[99] Chou T, Subramanian R, Park J and Mercier P 2014 A miniaturized ultrasonic power delivery system *2014 IEEE Biomedical Circuits and Systems Conf. (BioCAS) Proc.* (doi:10.1109/BioCAS.2014.6981757)

[100] Fowler A G and Moheimani S O R 2015 4-DOF SOI-MEMS ultrasonic energy harvester *2015 IEEE 15th Int. Conf. on Nanotechnology (IEEE-NANO)* (doi:10.1109/NANO.2015.7388922)

[101] Roundy S, Wright P K and Pister K S J 2002 Micro-electric vibration-to-electricity converters *ASME 2002 Int. Mechanical Engineering Congress and Exposition* (American Society of Mechanical Engineers) (doi:10.1115/IMECE2002-39309)

[102] Zhu Y, Moheimani S O R and Yuce M R 2011 A 2-DOF MEMS ultrasonic energy harvester *IEEE Sens. J.* **11** 155–61

[103] Zhu Y, Moheimani S O R and Yuce M R 2009 A 2-DOF wideband electrostatic transducer for energy harvesting and implantable applications *2009 IEEE Sensors* (doi:10.1109/ICSENS.2009.5398476)

[104] Kawanabe H, Katane T, Saotome H, Saito O and Kobayashi K 2001 Power and information transmission to implanted medical device using ultrasonic *Japan J. Appl. Phys.* **40** 3865

[105] Suzuki S-N, Kimura S, Katane T, Saotome H, Saito O and Kobayashi K 2002 Power and interactive information transmission to implanted medical device using ultrasonic *Japan J. Appl. Phys.* **41** 3600

[106] Kim A, Powell C R and Ziaie B 2014 An implantable pressure sensing system with electromechanical interrogation scheme *IEEE Trans. Biomed. Eng.* **61** 2209–17

[107] Mazzilli F, Peisino M, Mitouassiwou R, Cotte B, Thoppay P, Lafon C, Favre P, Meurville E and Dehollain C 2010 In-vitro platform to study ultrasound as source for wireless energy transfer and communication for implanted medical devices *2010 Annual Int. Conf. of the IEEE Engineering in Medicine and Biology* (doi:10.1109/IEMBS.2010.5627541)

[108] Duck F, Baker A and Starritt H 1998 *Ultrasound in Medicine* (Boca Raton, FL: CRC Press)

[109] Dogheche K, Cavallier B, Delobelle P, Hirsinger L, Cattan E, Rèmiens D, Marzencki M, Charlot B, Basrour S and Ballandras S 2006 A Bi-Stable micro-machined piezoelectric transducer for mechanical to electrical energy transformation *Integr. Ferroelectr.* **76** 3–12

[110] Lee B-S, Shih P-J, He J-J, Shih W-P and Wu W-J 2007 A study of implantable power harvesting transducers *Proc. SPIE* **6530** 65300I

[111] Shih P J and Shih W P 2010 Design, fabrication, and application of bio-implantable acoustic power transmission *J. Microelectromech. Syst.* **19** 494–502

[112] Shih P-J, Weng W-P, Shih W-P, Tsai Y-C and Chang P-Z 2007 Acoustic polarization for optimized implantable power transimittion *2007 IEEE 20th Int. Conf. on Micro Electro Mechanical Systems MEMS.* (doi:10.1109/MEMSYS.2007.4433136)

[113] Pardo R L J, García A, Brebøl K, Leighton G and Huang Z 2010 Impedance measurements for determination of elastic and piezoelectric coefficients of films *Adv. Appl. Ceram.* **109** 156–61

[114] Kanno I, Fujii S, Kamada T and Takayama R 1997 Piezoelectric properties of *c*-axis oriented Pb(Zr, Ti)O$_3$ thin film *Appl. Phys. Lett.* **70** 1378–80

[115] Hindrichsen C G, Lou-Moller R, Hansen K and Thomsen E V 2010 Advantages of PZT thick film for MEMS sensors *Sensors Actuators* A **163** 9–14

[116] Vrejoiu B I, Le Rhun G, Pintilie L, Hesse D and Alexe M 2006 Intrinsic ferroelectric properties of strained tetragonal PbZr0. 2Ti0. 8O3 obtained on layer-by-layer grown, defect-free single-crystalline films *Adv. Mater.* **18** 1657–61

[117] Aktakka E E, Kim H and Najafi K 2009 Wafer level fabrication of high performance MEMS using bonded and thinned bulk piezoelectric substrates *TRANSDUCERS 2009 —2009 Int. Solid-State Sensors, Actuators and Microsystems Conf.* (doi:10.1109/SENSOR.2009.5285795)

[118] Aktakka E E and Najafi K 2015 Three-axis piezoelectric vibration energy harvester *2015 28th IEEE Int. Conf. on Micro Electro Mechanical Systems (MEMS)* (doi:10.1109/MEMSYS.2015.7051166)

[119] Tang G *et al* 2012 Fabrication and analysis of high-performance piezoelectric MEMS generators *J. Micromech. Microeng.* **22** 65017

[120] Shigeta Y, Yamamoto T, Fujimori K, Sanagi M, Nogi S and Tsukagoshi T 2009 Development of ultrasonic wireless power transmission system for implantable electronic devices *2009 European Wireless Technology Conf. (EuWIT 2009)* (Piscataway, NJ: IEEE)

[121] Charthad J, Weber M J, Chang T C, Saadat M and Arbabian A 2014 A mm-sized implantable device with ultrasonic energy transfer and RF data uplink for high-power applications *Proc. IEEE 2014 Custom Integrated Circuits Conf.* (doi:10.1109/CICC.2014.6946071)

[122] Shmilovitz D, Ozeri S, Wang C-C and Spivak B 2014 Noninvasive control of the power transferred to an implanted device by an ultrasonic transcutaneous energy transfer link *IEEE Trans. Biomed. Eng.* **61** 995–1004

[123] Fang B, Feng T, Zhang M and Chakrabartty S 2015 Feasibility of B-mode diagnostic ultrasonic energy transfer and telemetry to a cm 2 sized deep-tissue implant *2015 IEEE Int. Symp. on Circuits and Systems (ISCAS)* (doi:10.1109/ISCAS.2015.7168750)

[124] Zhou J, Kim A, Song S H and Ziaie B 2015 An ultrasonically powered implantable micro-light source for localized photodynamic therapy *Transducers-2015 18th Int. Conf. Solid-State Sensors, Actuators Microsystems, (TRANSDUCERS 2015)* pp 876–9

[125] Zhou J, Kim A and Ziaie B 2015 An ultrasonically controlled power management system for implantable biomedical devices *Biomedical Circuits and Systems Conf. (BioCAS)* (doi:10.1109/BioCAS.2015.7348297)

[126] Vihvelin H, Leadbetter J, Bance M, Brown J A and Adamson R B A 2016 Compensating for tissue changes in an ultrasonic power link for implanted medical devices *IEEE Trans. Biomed. Circuits Syst.* **10** 404–11

[127] Radziemski L and Makin I R S 2016 *In vivo* demonstration of ultrasound power delivery to charge implanted medical devices via acute and survival porcine studies *Ultrasonics* **64** 1–9

[128] Seo D, Neely R M, Shen K, Rabaey J M, Carmena J M, Maharbiz M M, Singhal U and Alon E 2016 Wireless recording in the peripheral nervous system with ultrasonic neural dust neuron neuroresource wireless recording in the peripheral nervous system with ultrasonic neural dust *Neuron* **91** 1–11

CHAPTER 3

A MEMS SCALE ULTRASONIC POWER RECEIVER

FOR BIOMEDICAL IMPLANTS

Mechanical sensors

A MEMS-Scale Ultrasonic Power Receiver for Biomedical Implants

Hamid Basaeri[1] , Yuechuan Yu[2] , Darrin Young[2], and Shad Roundy[1]

[1]Department of Mechanical Engineering, University of Utah, Salt Lake City, UT 84112 USA
[2]Department of Electrical and Computer Engineering, University of Utah, Salt Lake City, UT 84112 USA

Abstract—Bio-implantable medical devices need a reliable and stable source of power to perform effectively. Although batteries are typically the first candidate to power implantable devices, they have a limited lifetime and must be periodically replaced or recharged. To alleviate this issue, ultrasonic power transfer systems can wirelessly power bio-implantable devices. Diaphragm structures which use piezoelectric materials (also known as piezoelectric micromachined ultrasonic transducers) can be fabricated on a small scale suitable for implantable devices. Diaphragms can be fabricated by deposition of lead zirconate titanate (PZT) films on a non-piezoelectric material. However, current deposition techniques cannot provide PZT thicknesses more than about 6 μm. We numerically investigate the performance of a square ultrasonic PZT receiver with inner and outer electrodes. Using COMSOL simulations, we optimize the piezoelectric film thickness for a 2 mm × 2 mm diaphragm with a silicon substrate of 50 μm and find the optimal thickness to be 20 μm for a maximum output power delivered to an optimal load. We fabricate a micromachined ultrasonic power-generating receiver capable of providing sufficient power for implantable medical devices using bulk PZT. We show that when a transmitter is generating an input power intensity of 322 mW/cm^2 at 88 kHz, less than Food and Drug Administration limit of 720 mW/cm^2, the receiver delivers a power of 0.7 mW to an optimal resistive load of 4.3 kΩ when the distance between the transmitter and the receiver is 20 mm. Furthermore, the process developed can be used to fabricate devices that are significantly smaller than the one characterized, which enables further miniaturization of bio-implanted systems.

Index Terms—Mechanical sensors, acoustic energy harvesting, acoustic power transfer, implantable sensors, piezoelectric micromachined ultrasonic transducer (pMUTs).

I. INTRODUCTION

Acoustic power transfer can be a safe alternative to batteries. In comparison to other wireless transfer methods such as inductive and radio frequency power transfer, acoustic energy has much shorter wavelengths and relatively lower attenuation in human tissue; therefore, acoustic energy can be more efficient for small devices and large implant depths. For a more detailed discussion of acoustic power transfer for implantable medical devices (IMDs), see a recent review [1]. In these systems, an external transmitter converts electrical energy into pressure wave, which is transferred through the human body. A receiver, implanted in the body, captures and converts the pressure wave to electrical energy (typically using the piezoelectric effect). A rectifier provides a usable stable dc voltage for IMDs. There are two common architectures for ultrasonic power receiver structures: plate and diaphragm architectures. Diaphragm structures have been sparsely studied [2]–[4] compared to off-the-shelf plate transducers [5]–[7]. Although the plate is the more widely used architecture, the diaphragm can be a better candidate for powering a bio-implantable device because it can be smaller at a given operating frequency and can produce more power at very small scales [8].

The majority of researchers developing piezoelectric micromachined ultrasonic transducers (pMUTs) use thin film deposition techniques such as sol-gel spin coating [9], screen printing [10], and sputtering [11]. Microelectromechanical systems (MEMS) piezo processes can only fabricate layer thicknesses up to 6 μm [12]. These thin piezo films suffer from a low electromechanical coupling coefficient due to film stresses and/or lower density compared to their bulk piezo material

counterparts [13]. As an alternative to deposited piezo layers, high-quality bulk piezo materials can be used in the fabrication of pMUTs. However, off-the-shelf piezo transducers are typically 100-μm thick or thicker, which results in a large gap in available piezoelectric material thickness between deposited thin layers and off-the-shelf bulk transducers. When an ultrasound receiver requires a piezo layer with thickness between 6 and 100 μm to deliver the maximum power to an optimal load, neither of these techniques can be used.

In this article, we numerically and experimentally investigate the power generation capability of a pMUT. The magnitude of the transferred power depends on several factors including size of the receiver and the operating frequency. The pMUT needs to be small to reduce the trauma to the patient and needs to operate at a relatively low frequency (~100 kHz) to reduce attenuation in human tissue. To achieve a 2 mm × 2 mm device capable of operating in low frequencies, we study the effect of the thickness of the piezoelectric layer on the generated voltage and power. The ideal piezo thickness for that particular size and frequency combination is in the 6 to 100 μm range. Since this thickness can be provided by neither current deposition techniques nor off-the-shelf piezo transducers, we propose a fabrication process using bulk piezo materials that can bridge the gap in available piezoelectric layer thicknesses. We start with a thick bulk lead zirconate titanate (PZT) and polish it down to produce a PZT layer that is thicker than standard microfabrication processes but thin enough for a millimeter scale bending diaphragm. Then, we characterize the fabricated device in air and water and investigate the performance of the device as an acoustic power receiver.

II. DESIGN AND FABRICATION

The device structure of the proposed pMUT receiver with patterned inner and outer electrodes is illustrated in Fig. 1(a). When acoustic
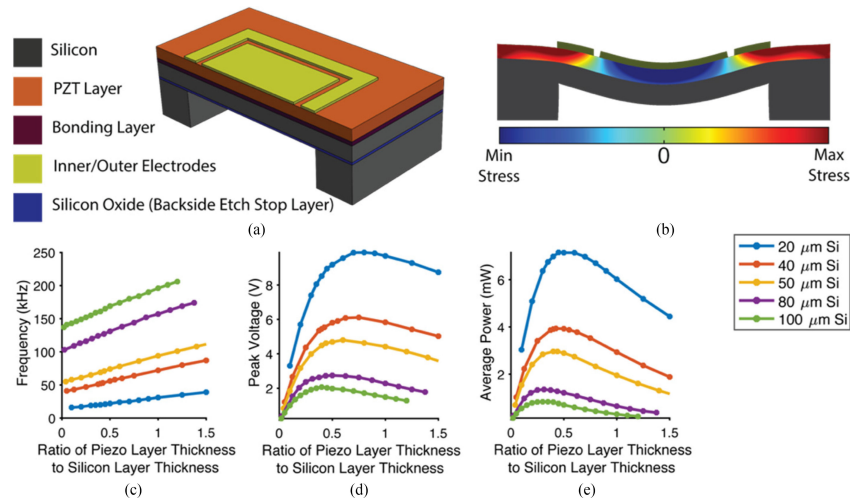
Fig. 1. (a) Schematic drawing showing the cross-sectional view of the proposed micromachined ultrasonic receiver. (b) Working principle of the pMUT structure with inner and outer electrodes; the edge of the inner electrode is placed where stress changes direction. (c) Simulated resonance frequency versus ratio of piezo thickness to silicon thickness. (d) Simulated peak voltage versus ratio of piezo thickness to silicon thickness. (e) Simulated average power across an optimal resistive load versus ratio of piezo thickness to silicon thickness.

pressure is applied to the receiver, the inner (outer) portion of the diaphragm will be in tension, whereas the outer (inner) portion will be in compression [14]. To achieve the maximum voltage, the inner electrode needs to be placed up to where the sum of stresses becomes zero [see Fig. 1(b)]. By placing inner and outer electrodes on the top surface of PZT, there is no need to access the floating bottom electrode of PZT that makes the fabrication process much easier. Our proposed electrode configuration results in a lower electrical capacitance compared to typical pMUTs with top and bottom electrodes.

When the device is subjected to acoustic pressure, the applied pressure is converted to electrical energy by the direct piezoelectric effect. The generated voltage and power depend on the thickness of the piezoelectric layer. Assuming a piezo with a thickness of t and a cross-sectional area of A is being cyclically stressed at frequency ω, the generated power dissipated through an optimal resistive load can be derived as follows [15]:

$$P_{\text{rms}} = \frac{1}{4}\omega k^2 c^E (At) S^2 \tag{1}$$

where k and c^E are the coupling coefficient and stiffness of piezo, respectively, and S is the zero-to-peak strain in the piezo. When the piezo thickness increases, the volume increases, so the power should go up; however, the strain decreases since thinner layers of piezoelectric material have higher strains. When the thickness becomes too large, the reduction in strain dominates. On the other hand, as thickness gets too low, not having enough piezo material dominates. Therefore, there is a thickness at which the power is optimized. COMSOL simulations have been carried out in water for different thickness of piezoelectric and silicon layers. The length of a side of the square receiver is set to be 2 mm, and the patterned electrodes are also modeled. At each thickness, the device is operated at its resonance frequency, and the optimal load is used for estimating the generated voltage and power. The resonance frequency, generated peak voltage, and average power are plotted against the ratio of piezo thickness to silicon thickness in Fig. 1(c)–(e), respectively. In this study, our aim is to maximize the power available for a biomedical implant of a size significantly less than 1 cm². Thus, we restrict ourselves to 4 mm² for the power receiver. Our goal is to produce the maximum amount of power within this size constraint. We desire a relatively low resonance frequency in order to minimize attenuation in tissue. However, we still need to operate well above audible frequencies. This leads us to a desired device frequency of approximately 100 kHz. The total diaphragm thickness (around 70
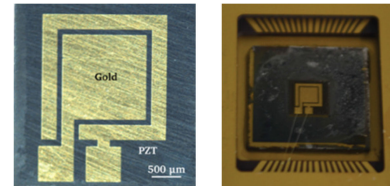
Fig. 2. (Left) Close-up of one square chip. (Right) Microfabricated PZT power receiver packaged for characterization.

μm) was chosen to operate at about this frequency within a 4-mm² area. For this specific design, the ratio of optimal PZT thickness to silicon thickness is around 0.4, resulting in a desired silicon layer thickness of 50 μm and a PZT layer thickness of 20 μm. One could also design an array of smaller and thinner devices with the same resonance frequency and fit them in the 4-mm² area. Such a device could result in similar high-power levels. However, we chose to use a single larger device with thick bulk piezoelectric materials to take advantage of their better performance.

The device was fabricated at the wafer-level with a silicon on insulator (SOI) wafer. The three-mask fabrication process includes deposition of bonding layer metals, bonding, mechanical lapping, release of diaphragm structure by back-side etching of the SOI wafer, and deposition of inner and outer electrodes (Cr/Au). The fabrication process starts with deposition of the bonding layer metals (Au/In) on the bulk PZT-5A and SOI wafer. The bonding layers act as a floating electrode and consist of 2.2 μm of Au and 600 nm of In on the wafer and 2.2 μm of Au on PZT. Then, the PZT sheet was diced into small square pieces of the desired size. The PZT pieces were then bonded to the SOI wafer using a heated platen press with a bonding pressure of 0.75 MPa at 188 °C for 1 h. Although there are several bonding techniques available, we chose In-Au diffusion bonding and used metals, instead of polymers, as the bonding layers in order to get a robust and high-quality bond and in order to stay well below the PZT Curie temperature of 350 °C. Gold can be used as a good bonding layer; however, the bonding temperature would be as high as 500 °C [16]. We used indium as the other bonding layer which has a relatively low melting temperature to reduce the bonding temperature. In this bonding technique, called transient-liquid-phase diffusion bonding, a low melting point interlayer metal (indium) is sandwiched in between two parent metals (gold). As the temperature increases, the molten
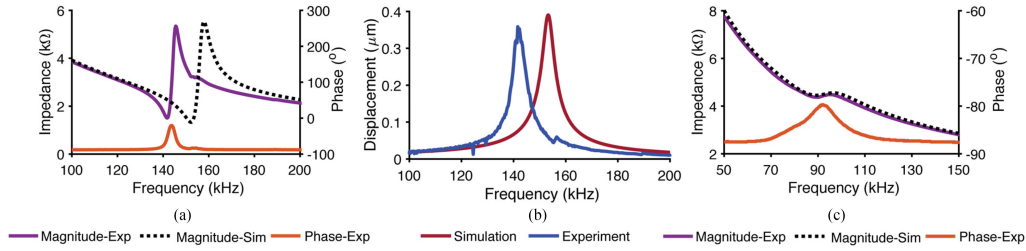
Fig. 3. (a) Impedance of the fabricated acoustic power receiver in air. (b) Comparison of measured and simulated displacement in air. (c) Impedance of the fabricated acoustic power receiver in water.
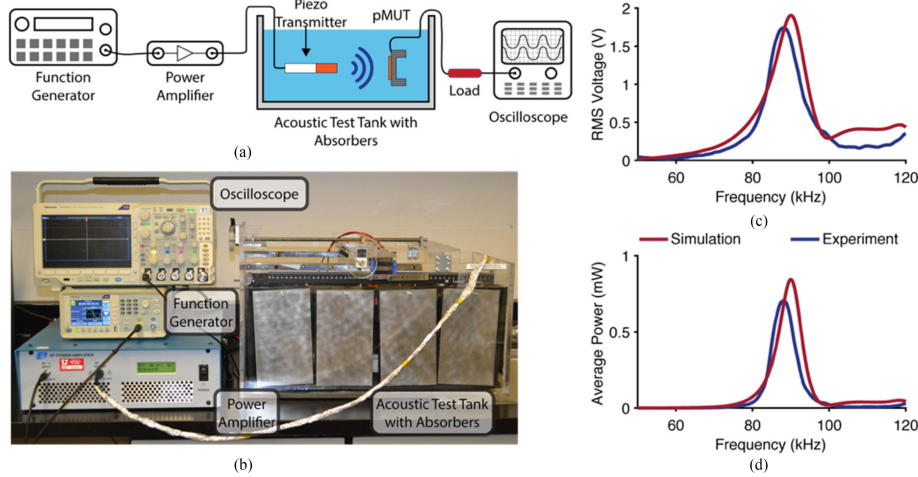
Fig. 4. (a) Schematic of the test setup for measuring voltage and power. (b) Actual test setup for measuring voltage and power. (c) Comparison of measured and simulated output voltage on a 4.3 kΩ resistive load at a distance of 20 mm in water. (d) Comparison of measured and simulated output power on a 4.3 kΩ resistive load at a distance of 20 mm in water.

interlayer diffuses into and reacts with the parent metals on both sides [17]. Mechanical lapping and polishing processes were performed to decrease the thickness of the bulk PZT from 127 to ∼40 μm. (Note that we choose a higher than optimal PZT thickness as our manual polishing process is not accurate enough to guarantee 20 μm thickness, and we stopped the polishing at 40 μm since we did not want to take the risk of ending up with a thickness less than 20 μm. The thickness variation over the surface of the PZT on a single device is about ±1 μm.) The diaphragm was created by back-side deep reactive ion etch (DRIE) stopping on a 100-nm SiO_2 layer. Finally, the top electrodes were patterned by sputtering and lifting off of Cr/Au. Fig. 2 shows photographs of the fabricated and packaged device.

III. RESULTS AND DISCUSSION

The fabricated diaphragm was first characterized in air. The impedance characterization was performed using an impedance analyzer (Agilent 4294A), as shown in Fig. 3(a). Off-resonance, the phase is −90° since the device acts like a capacitor; however, at resonance the reactance is zero leaving only a real impedance and the phase goes to zero. The resonance and anti-resonance frequencies are 140.25 kHz and 145.75 kHz, respectively. The effective electromechanical coupling coefficient k_{eff}^2 can be derived from the resonance frequency f_r and the anti-resonance frequency f_a through the following relation [18]:

$$k_{eff}^2 = \frac{f_a^2 - f_r^2}{f_a^2}. \tag{2}$$

The calculated effective electromechanical coupling coefficient (k_{eff}) of the presented pMUT is 0.272, which is in line with what

would be expected from a device with bulk PZT material (the published coupling coefficient of the piezoelectric material is 0.35 (k_{31}) [19]) and is significantly higher than most deposited PZT materials [20].

Actuated displacement of the fabricated device was measured using a laser Doppler vibrometer. Tests were run with a swept 3 V_{pp} sinusoidal input from a function generator (Tektronix AFG1062). Frequency sweep ranges were between 100 and 200 kHz. In order to confirm that the piezoelectric properties of the bulk material are fully conserved, measured displacement of a diaphragm is compared with its FEA simulation in Fig. 3(b). The piezoelectric layer thickness is set to 40 μm in the simulations. The experimental results agree well with the values extracted from COMSOL simulations. The measured resonance frequency of the device in air is 142 kHz, whereas the resonance frequency of the simulated device is 151 kHz. The small difference between the simulated and experimental resonance frequency values could result from not accounting for the metal layers in the simulation, and nonperfect polishing and DRIE processes. As power generation is a strong function of the quality factor (Q), it is important to empirically validate the quality factor for the MEMS implementation. The values of Q factor are used in our simulations to account for losses. The measured mechanical quality factor of the fabricated device in air is 33.8.

Second, the device was tested in an acoustic water tank. The test tank is a 59 × 28 × 28 cm^3 acrylic tank lined with ultra-soft polyurethane acoustic absorbers. Fig. 3(c) shows the impedance measurement in water and is compared to COMSOL simulations. The measured and simulated resonance frequencies in water are 88 and 90 kHz, respectively. The resonance frequency of the device decreases from 142 to 88 kHz due to the effect of added mass in water. Water has higher damping compared to air, which

lowers the Q factor. The measured Q factor of the device in water is 6.

After characterizing the device, the performance of the fabricated device in transferring power was investigated in a water-filled acoustic test tank. The schematic and image of the test setup are shown in Fig. 4(a) and (b), respectively. For the transmitter, a piezoelectric cylinder (APC Inc.; 850 material, 28.65-mm thick, 12.8 mm diameter) with a resonance frequency of 47 kHz in water was mounted to acrylonitrile-butadiene-styrene (ABS) tubing (McMaster-Carr; 1839T371) with cyanoacrylate and placed in distilled water. During the test, the receiver voltage under loading was measured and recorded for the peak input electrical power of 417.7 mW. The input power was calculated by knowing the input voltage and the impedance characteristics of the transmitter. As shown in Fig. 4(c), the device is capable of producing 1.74 V_{RMS} across an optimal load of 4.3 kΩ. The optimal load is the load at which the average power is maximum. It was selected by sweeping the resistive load and recording the voltage across the resistor. Three-dimensional COMSOL simulations were carried out by modeling the pMUT, the transmitter and the medium. Simulated and experimentally measured voltage and power of the pMUT are shown in Fig. 4(c) and (d) for the same transmitted acoustic intensity. The 1.74 V_{RMS} voltage results in average output power of 0.7 mW and a power density of 17.5 mW/cm^2. The overall efficiency of the system is about 0.33%. The input acoustic intensity of 322 mW/cm^2 is well below the safety limit for ultrasound intensity (720 mW/cm^2) defined by the United States Food and Drug Administration (FDA) [21]. The acoustic intensity at 20-mm depth is 74.8 mW/cm^2, which was measured with a hydrophone. The measured output power of 0.7 mW is significantly higher than that reported for devices with deposited PZT (59.01 μW with acoustic intensity of 700 mW/cm^2 at 10 mm [22], and 0.15 μW [23]) even with lower acoustic intensity due to the use of thicker PZT. The generated output power can be improved by applying input power intensity closer to the FDA limit and also using matching layers for the transmitter to reduce the reflection between the transmitter and the medium.

IV. CONCLUSION

In summary, a pMUT with inner and outer electrodes was developed using bulk piezoelectric materials. We found the optimal thickness ratio of the piezoelectric layer to silicon layer to achieve the maximum power from the device. We presented a fabrication process that is capable of producing piezo thicknesses much higher than current thin film deposition techniques. The fabricated device can operate at lower frequencies compared to off-the-shelf transducers resulting in lower attenuation in an aqueous environment. We characterized the device in air and water. The device is capable of providing 0.7 mW of power, which is sufficient for most bio-medical implants. As the final application of these devices is implantation in the human body, they need to be coated and packaged with bio-compatible materials [24]. Moreover, the acoustic power receiver may be misorientated at some angle with respect to the transmitter and may be laterally misaligned after being implanted in the human body. Any changes in the location of the receiver could affect the received power [25]. Future work should, therefore, include investigation of the location uncertainties on the performance of the device. This device shows great potential for powering IMDs since it can generate sufficient power in larger depth compared to other thin film receivers.

ACKNOWLEDGMENT

REFERENCES

[1] H. Basaeri, D. B. Christensen, and S. Roundy, "A review of acoustic power transfer for bio-medical implants," *Smart Mater. Struct.*, vol. 25, no. 12, 2016, Art. no. 123001.

[2] Z. Wang *et al.*, "A flexible ultrasound transducer array with micro-machined bulk PZT," *Sensors*, vol. 15, no. 2, pp. 2538–2547, 2015.

[3] T. Wang, T. Kobayashi, and C. Lee, "Micromachined piezoelectric ultrasonic transducer with ultra-wide frequency bandwidth," *Appl. Phys. Lett.*, vol. 106, no. 1, 2015, Art. no. 013501.

[4] Q. Shi, T. Wang, and C. Lee, "MEMS based broadband piezoelectric ultrasonic energy harvester (PUEH) for enabling self-powered implantable biomedical devices," *Sci. Rep.*, vol. 6, 2016, Art. no. 24946.

[5] T. C. Chang, M. J. Weber, M. L. Wang, J. Charthad, B. T. Khuri-Yakub, and A. Arbabian, "Design of tunable ultrasonic receivers for efficient powering of implantable medical devices with reconfigurable power loads," *IEEE Trans. Ultrason. Ferroelect. Freq. Control*, vol. 63, no. 10, pp. 1554–1562, Oct. 2016.

[6] H. Basaeri, D. Christensen, Y. Yu, T. Nguyen, P. Tathireddy, and D. J. Young, "Ultrasonically powered hydrogel-based wireless implantable glucose sensor," in *Proc. IEEE Sens.*, 2016, pp. 1–3.

[7] D. Seo, J. M. Carmena, J. M. Rabaey, M. M. Maharbiz, and E. Alon, "Model validation of untethered, ultrasonic neural dust motes for cortical recording," *J. Neuroscience Methods*, vol. 244, pp. 114–122, 2015.

[8] D. B. Christensen and S. Roundy, "Ultrasonically powered piezoelectric generators for bio-implantable sensors: Plate versus diaphragm," *J. Intell. Mater. Syst. Struct.*, vol. 27, no. 8, pp. 1092–1105, 2016.

[9] L. Pardo, R. Jiménez, A. García, K. Brebøl, G. Leighton, and Z. Huang, "Impedance measurements for determination of elastic and piezoelectric coefficients of films," *Adv. Appl. Ceram.*, vol. 109, no. 3, pp. 156–161, 2010.

[10] C. G. Hindrichsen, R. Lou-Moller, K. Hansen, and E. V. Thomsen, "Advantages of PZT thick film for MEMS sensors," *Sens. Actuators, A Phys.*, vol. 163, no. 1, pp. 9–14, 2010.

[11] E. Mehdizadeh and G. Piazza, "Through-package wireless powering via piezoelectric micromachined ultrasonic transducers," in *Proc. IEEE Int. Conf. Micro Electro Mech. Syst.*, 2018, pp. 1076–1079.

[12] C. Cassella and G. Piazza, "AlN two-dimensional-mode resonators for ultra-high frequency applications," *IEEE Electron Device Lett.*, vol. 36, no. 11, pp. 1192–1194, Nov. 2015.

[13] S. Trolier-Mckinstry and P. Muralt, "Thin film piezoelectrics for MEMS," *J. Electroceramics*, vol. 12, pp. 7–17, 2004.

[14] S. Kim, W. W. Clark, and Q. Wang, "Piezoelectric energy harvesting using a diaphragm structure," *Smart Struct. Mater.*, vol. 5055, pp. 307–318, 2003.

[15] X. Ma, A. Wilson, C. D. Rahn, and S. Trolier-McKinstry, "Efficient energy harvesting using piezoelectric compliant mechanisms: Theory and experiment," *J. Vib. Acoust.*, vol. 138, no. 2, 2016, Art. no. 021005.

[16] K. Tanaka, T. Konishi, M. Ide, and S. Sugiyama, "Wafer bonding of lead zirconate titanate to Si using an intermediate gold layer for microdevice application," *J. Micromechanics Microeng.*, vol. 16, no. 4, pp. 815–820, 2006.

[17] E. E. Aktakka, R. L. Peterson, and K. Najafi, "Wafer-level integration of high-quality bulk piezoelectric ceramics on silicon," *IEEE Trans. Electron Devices*, vol. 60, no. 6, pp. 2022–2030, Jun. 2013.

[18] J. Jung, S. Kim, W. Lee, and H. Choi, "Fabrication of a two-dimensional piezoelectric micromachined ultrasonic transducer array using a top-crossover-to-bottom structure and metal bridge connections," *J. Micromechanics Microeng.*, vol. 23, no. 12, 2013, Art. no. 125037.

[19] "PSI-5A4E Piezoceramic Sheets and Their Properties, Piezo Systems, Inc." [Online]. Available: http://www.piezo.com/prodsheet1sq5A.html

[20] P. Muralt *et al.*, "Piezoelectric micromachined ultrasonic transducers based on PZT thin films," *IEEE Trans. Ultrason. Ferroelect. Freq. Control*, vol. 52, no. 12, pp. 2276–2288, Dec. 2005.

[21] "Guidance for industry and FDA staff information for manufacturers seeking marketing clearance of diagnostic ultrasound systems and transducers," FDA, Silver Spring, MD, USA, 2008.

[22] Q. Shi, T. Wang, T. Kobayashi, and C. Lee, "Investigation of geometric design in piezoelectric microelectromechanical systems diaphragms for ultrasonic energy harvesting," *Appl. Phys. Lett.*, vol. 108, no. 19, pp. 106–111, 2016.

[23] B.-S. Lee, P.-J. Shih, J.-J. He, W.-P. Shih, and W.-J. Wu, "A study of implantable power harvesting transducers," *Proc. SPIE*, vol. 6530, 2007, Art. no. 65300I.

[24] C. Zhang, T. W. Piaget, K. R. Maile, and R. A. Balczewski, "Acoustic communication transducer in implantable medical device header," U.S. Patent 570,998B2, 2002.

[25] D. B. Christensen, H. Basaeri, and S. Roundy, "A computationally efficient technique to model depth, orientation and alignment via ray tracing in acoustic power transfer systems," *Smart Mater. Struct.*, vol. 2006, no. 12, 2017, Art. no. 125020.

CHAPTER 4

ACOUSTIC POWER TRANSFER FOR BIOMEDICAL

IMPLANTS USING PIEZOELECTRIC RECEIVERS:

EFFECTS OF MISALIGNMENT AND

MISORIENTATION

This chapter was submitted as "Acoustic power transfer for biomedical implants using piezoelectric receivers: effects of misalignment and misorientation," to Journal of Micromechanics and Microengineering managed by Institute of Physics Publishing on March 29, 2019. The published version of this chapter has been published in volume 29, number 8, in June 2019 by IOP Publishing.

Acoustic power transfer for biomedical implants using piezoelectric receivers: effects of misalignment and misorientation

Hamid Basaeri[1] ![ORCID]**, Yuechuan Yu**[2]**, Darrin Young**[2] **and Shad Roundy**[1]

[1] Department of Mechanical Engineering, University of Utah, Salt Lake City, UT, United States of America
[2] Department of Electrical and Computer Engineering, University of Utah, Salt Lake City, UT, United States of America

E-mail: h.basaeri@utah.edu

Abstract

Implantable medical devices (IMDs) can be powered wirelessly using acoustics with no need for a battery. In an acoustic power transfer system, which consists of a transmitter, medium, and a receiver, the power that the receiver generates is a function of its position (depth, orientation, and alignment relative to the transmitter). The power delivered to the implant should remain stable and reliable even with possible uncertainties in the location of the implant. In this paper, we compare two common designs for piezoelectric ultrasonic transducers that can be used for acoustically powering IMDs, and study their generated power sensitivity to any change in their location. Although commercial off-the-shelf (COTS) transducers are widely being used in the literature, they may not be the best candidate for powering small implants since they may not be able to provide sufficient power in the presence of location uncertainties. Piezoelectric micromachined ultrasonic transducers (pMUTs) are diaphragm structures and are also suitable for wirelessly powering implants. We present a pMUT receiver and study the sensitivity of the generated power of the pMUT to changes in its position. We then perform a comparative study between power generation capability of our pMUT and a COTS transducer with the same lateral dimensions as the pMUT. We observed that the generated power from a pMUT structure is less sensitive to misorientation and misalignment of the device. The average percentage improvement in the generated power from pMUT compared to COTS are 86%, 917%, and 111% for depth, alignment, and orientation, respectively.

Keywords: piezoelectric micromachined ultrasonic transducer, acoustics power transfer, bulk-mode transducer, ultrasonic generator

(Some figures may appear in colour only in the online journal)

1. Introduction

The use of implantable medical devices (IMDs) for monitoring human health is growing rapidly. These devices are usually designed to monitor biological parameters, deliver drugs, or improve the function of particular organs in the human body. IMDs require a sufficient and stable source of power in order to perform their tasks properly. The need for wirelessly powering IMDs is significantly increasing as batteries are not often the best candidate to power these devices due to their limited lifetime and large size [1]. The power required for IMDs is generally on the order of hundreds of micro-watts to tens of milliwatts at the extreme high end [2, 3]. For example, pacemakers usually require a power below 100 μW while cochlear implants need around 1 mW to 10 mW to operate [4]. Kinetic energy harvesting has been implemented

as a method to power implantable devices such as pacemakers [5, 6]. These systems harvest the energy of human motion to power an implant. The available vibration intensity inside the body is usually not very high [7]. Thus, vibrational or kinetic energy harvesters cannot be considered as an appropriate method to power implantable devices.

Wireless power transfer technology is a promising alternative to batteries as well. Although inductive power transfer [8] and mid-range radio frequency (RF) power transmission [9] are capable of providing wireless power to IMDs, acoustic waves have the potential to be employed in wireless transfer systems to safely provide electrical power to an IMD and have several advantages over other powering techniques. These advantages include lower absorption in tissue, shorter wavelength enabling smaller transducers, and higher power intensity threshold for safe operation. Acoustic power transfer systems can provide sufficient power for deeply implanted devices [10]. For a more detailed discussion of different power approaches and in particular acoustic power transfer for implantable medical devices (IMDs) we refer the reader to a recent review [11]. An acoustic power transfer system generally consists of a transmitter outside the human body, and a receiver implanted inside the human body. The transmitter converts the input electrical energy to mechanical energy. The mechanical energy travels through the human body and is captured by the receiver, and is converted to electrical energy to power the IMD.

For an acoustic power transfer system, the power delivered to an IMD in human tissue is dependent on several system parameters: load impedance, operating frequency, receiver position relative to the transmitter, and receiver and transmitter size. As the position and orientation of the implant cannot be perfectly controlled, it is essential to consider the effect of the uncertainty of position and orientation of the implanted receiver on power transfer. Variation in position and orientation can be characterized using three parameters: depth, angle, and offset. Depth is the axial distance between the transmitter and receiver. Angle or orientation is defined as the angle between the receiver face and the transmitter face. Offset or alignment is the lateral distance between the center of the transmitter and center of the receiver. Any change in the location of the receiver may result in a drop in the generated power and may lead to a power level which is not sufficient for the IMD. In some cases, a lateral offset equal to the diameter of the receiver may result in approximately 70% drop in the generated voltage [12]. The drop could also be worse for the generated power as it is a function of voltage squared. The majority of literature in the area of acoustic power transfer for IMDs reported voltage or power delivered to the load as a function of depth or offset [13–15]. There are few researchers that have thoroughly investigated the dependency of power to depth, angle, and offset [16]. The sensitivity of the generated power to any change in the location of the receiver needs to be fully studied. This sensitivity may depend on the operating frequency as operating at lower frequencies which have longer wavelength can result in devices that are less sensitive to offset and alignment mismatches. As there are several types of ultrasonic receivers with different resonance frequencies,

it is necessary to study the effect of working in different frequencies on the sensitivity of the generated power to any change in the location of the receiver.

Capacitive micromachined ultrasonic transducers (CMUTs) have also been employed for wirelessly transferring power using a comb drive to generate electrical energy from a base vibration [17, 18]. The small gap required for achieving high sensitivity limits the potential generated acoustic power by reducing the deflection of the plate. CMUTs require large bias voltage which may create safety concerns. They have inherently nonlinear transduction mechanism that may introduce significant circuit design challenges [19]. Piezoelectric transducers are an alternative solution to these problems. Conventional ultrasonic transducers that may be employed for acoustic energy transfer are mostly based on commercial off-the-shelf (COTS) bulk piezoelectric materials, i.e. plate structures, with high acoustic impedance and poor acoustic coupling to human tissue. On the other hand, piezoelectric micromachined ultrasonic transducers (pMUTs), i.e. diaphragm structures, have lower acoustic impedance due to the lower stiffness of the membrane structure. Small element size and easy integration with supporting electronics are other advantages of pMUTs compared to COTS bulk piezoelectric transducers [20]. The thickness of pMUTs is much smaller than the wavelength while the thickness of bulk transducers needs to be half of the wavelength. So, using pMUTs would result in smaller devices compared to bulk structures when operating at the same frequency. Furthermore, for the same size of a receiver, diaphragm structures would have lower resonance frequencies. The bulk piezoelectric structure is widely used in therapeutic and diagnostic applications; however, the pMUT structure seems to be a better candidate for acoustic power transfer for IMDs in which the receivers are very small since this architecture is capable of generating more power than the bulk structure and is significantly less sensitive to changes in implant location for generator diameters in the sub-millimeter range [21]. Christensen and Roundy compared COTS plate and diaphragm mode structures for an acoustic power transmission system and numerically showed that the diaphragm structure is significantly less sensitive to changes in implant offset and angle. Although the pMUT seems to be a better candidate, the number of publications fabricating a microelectromechanical systems (MEMS) receiver are sparse compared to those using COTS transducers. One issue is that there is a significant gap in available piezoelectric material thickness between MEMS and COTS transducers. COTS piezoelectric transducers are typically available in thicknesses higher than 127 μm (0.005″) since this is the thinnest available bulk piezoelectric layer. On the other hand, MEMS piezoelectric processes can only fabricate layer thicknesses up to about 6 μm. [22]. In this paper, we present a MEMS fabrication process to fabricate pMUT devices with thicknesses in the range of 6 μm–127 μm.

The purpose of this paper is to provide a comprehensive comparison between two common piezoelectric ultrasonic transducers for powering implantable devices. To this end, load voltage and power of these structures as a function of depth, orientation, and alignment are fully studied and compared together. Although both of these structures have been

studied in the literature separately, there is no such an experimental analysis to compare these two structures. In order to fully explore the comparison of MEMS and COTS ultrasound transducers, we propose a new fabrication process that can bridge the gap in available piezoelectric layer thicknesses. We theoretically and experimentally analyze the performance of the fabricated device in the presence of uncertainties and compare its performance to a COTS device. The analysis provides insight into the conditions in which a MEMS scale diaphragm would be preferred as the receiver over a COTS transducer for a robust acoustic transfer system considering power loss due to disturbances in depth, orientation, and alignment.

2. Frequency selection for an acoustic power transfer system

The acoustic power transfer system needs to operate at a certain frequency. The resonance frequency of the receiving transducer is usually selected as the operating frequency, which results in maximum transferred power. Resonance frequencies are determined by the geometry of transducer and material constants. Generally, there are constraints on the size of the receiver as it needs to be implanted inside the human body. For a given size constraint, different transducers would have different frequency characteristics, which will be discussed in the next section. The operating frequency can affect the performance of the acoustic transfer system since several factors such as tissue attenuation, and Rayleigh distance are strong functions of frequency. To fully understand these effects, we need to first cover some basics of acoustics and beam patterns for an acoustic transmitter in this section. The behavior of this beam pattern is critical in understanding the sensitivity of the generated power to the location of the receiver.

For a circular unfocused bulk thickness-mode transducer, the acoustic beam radius is approximately equal to the radius of the transducer up to a certain distance, but it begins to spread at larger distances. In the region near the transducer (near-field), the pressure magnitude oscillates (i.e. has spatial resonances) resulting in multiple minima and maxima as one moves away from the face of the transmitter. This irregularity in amplitude, which is due to the interference between contributing waves from all parts of the transducer face, makes the power transfer unpredictable. However, in the regions further from the transducer face (far-field), the beam shape is more uniform and decays with increasing distance.

The pressure on the face of the receiver can be derived using Huygens principle. This principle calculates the pressure generated by an ultrasound transducer at any distance from the transducer face. Every point on the transducer face is assumed to be a radiator of a spherical pressure wave and considered as a point source. The pressure at any observation point is the contribution of all spherical waves from all point sources. For a circular transmitter as shown in figure 1 whose face is vibrating with a sinusoidal pressure with magnitude p_0 and angular frequency ω, the total pressure at the observation point is [23]:

$$p = \frac{kp_0}{2\pi} \int_{source} \frac{\cos\left(\omega t - kr' + \pi/2\right)}{r'} \rho d\rho d\theta, \quad (1)$$

where t is time, r' is the distance from the source points to the observation point, and k is the wavenumber $(2\pi/\lambda)$ assuming λ is the wavelength of the wave. Equation (1) can be solved separately in near-field and far-field. The near-field pattern of a circular transducer with radius a on the z-axis is expressed as [23]:

$$p(z, t) = p_0 \left[\cos\left(\omega t - kz\right) - \cos(\omega t - k\sqrt{a^2 + z^2})\right]. \quad (2)$$

The instantaneous acoustic intensity is the acoustic power per unit area. The acoustic intensity in a medium with the acoustic impedance Z is defined as:

$$I(z, t) = \frac{p^2(z,t)}{Z} = \frac{p_0^2}{Z}\left[\cos\left(\omega t - kz\right) - \cos(\omega t - k\sqrt{a^2 + z^2})\right]^2. \quad (3)$$

Equation (2) only holds for on-axis observation points and gives the on-axis pressure amplitude. The irregular pressure pattern in near-field can be described by this equation. The first term in equation (2) contains the contribution of pressure coming from all points on the face of the transducer. The second term contains the contributions of pressure coming from all points at the perimeter of the transducer and subtracts from the first term. As the distance between the transducer and the observation point increases, the phases of the first and second terms change at different rates resulting in a constructive/destructive interference pattern. The pressure magnitude is plotted in figure 2 for a circular transducer with radius a for a frequency range of 100 kHz–1 MHz. In the near-field, there are some points at which the pressure magnitude is zero resulting in zero output power. The transition between near-field and far-field occurs at a distance called Rayleigh distance. The Rayleigh distance increases with the increase in the operating frequency. Thus, at higher frequency the near-field is longer, so the receiver is more likely to be in the near-field. And when the receiver is in the near-field, there is a constructive/destructive interference pattern along the face of the receiver, so as the receiver moves axially that interference pattern will change and the output power will significantly change. It should be mentioned that operating at higher frequencies would result in higher pressure at a given distance. However, this may come at tradeoff in robustness to misalignment and misorientation.

In far-field, equation (1) can be calculated for any point, not just points along the transmission axis. This is due to the fact that the distance between the transmitter and the observation point is large enough to make some simplifications. The pressure profile and acoustic intensity for a circular transducer at any point (off-axis as well as on-axis) when the beam is observed in the far-field are [23]:

$$p(r, \phi, t) = \frac{\pi a^2 p_0 \sin\left(\omega t - kr\right)}{\lambda r}\left[\frac{2J_1\left(ka\sin\phi\right)}{ka\sin\phi}\right], \quad (4)$$

$$I(r, \phi, t) = \frac{\pi^2 a^4 p_0^2 \sin^2\left(\omega t - kr\right)}{\lambda^2 r^2}\left[\frac{2J_1\left(ka\sin\phi\right)}{ka\sin\phi}\right]^2, \quad (5)$$
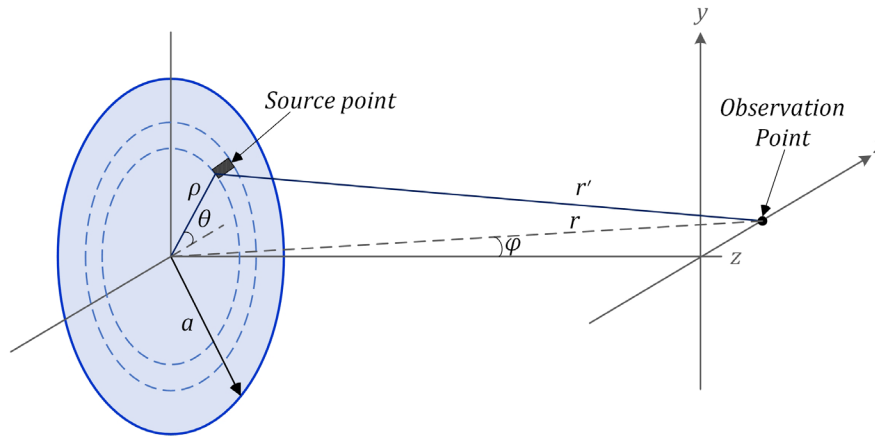
Figure 1. Geometry of a circular transmitter.
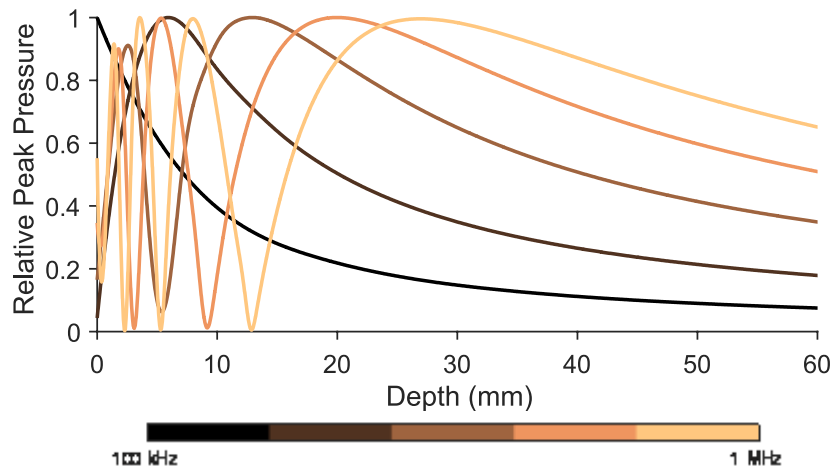
Figure 2. Relative on-axis peak pressure magnitude from a transducer with radius *a* at one particular time $t = 0$.

a)   b)
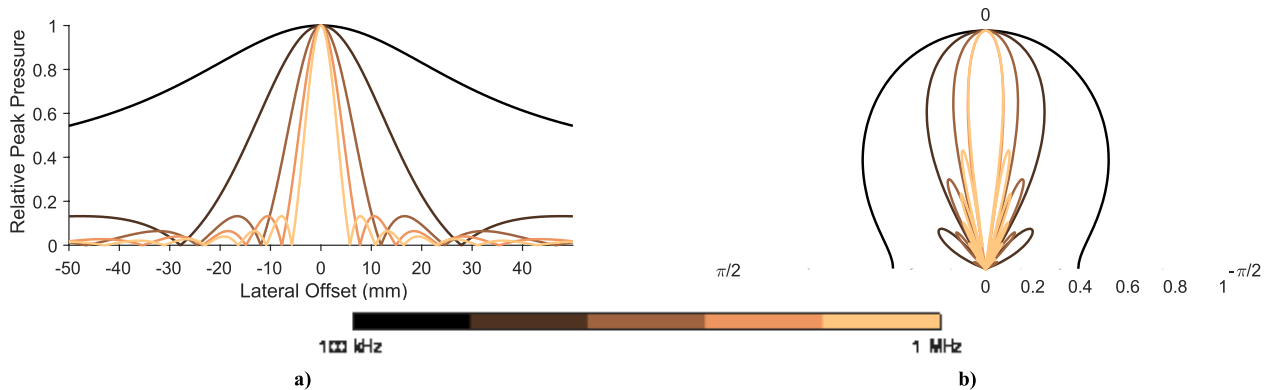
Figure 3. (a) The far-field pressure pattern from a transducer with radius *a* versus lateral offset; (b) an angular plot of the far-field pressure pattern in polar coordinates (the pressure is plotted in decibel units).

where J_1 is the Bessel function of the first kind with order 1. As we expected, the pressure in far-field has an inverse relationship with the distance, r. The term in the square bracket, which is called directional factor, is 1 at on-axis points and starts to decrease as the lateral distance between the transducer and the observing point increases. The normalized acoustic intensity at far-field is plotted against the lateral distance for a circular transducer in figure 3 for a frequency range

of 100 kHz–1 MHz. As shown in figure 3, at higher frequencies the pressure can drop significantly due to small changes in the lateral offset, which makes operation at high frequency very sensitive to any misalignment and misorientation of the receiver. As the receiver rotates or becomes misoriented with regard to the transmitter, a pressure gradient across the surface of the face results in decreasing the average pressure seen by the receiver. Any transducer that operates at high frequencies
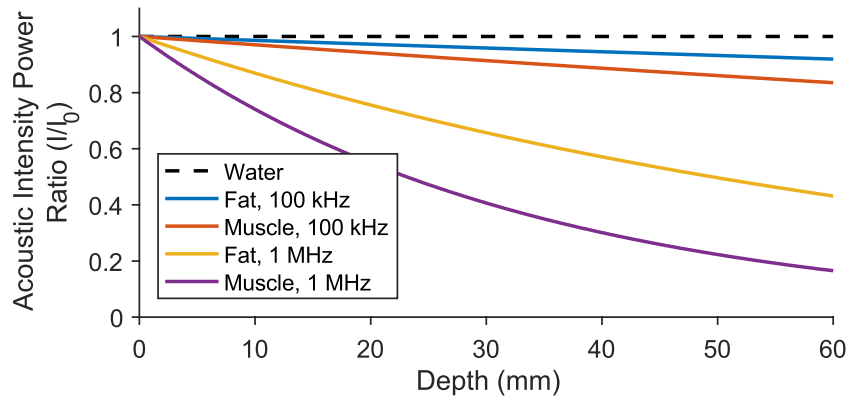
Figure 4. The effect of attenuation for different operating frequencies in different mediums.
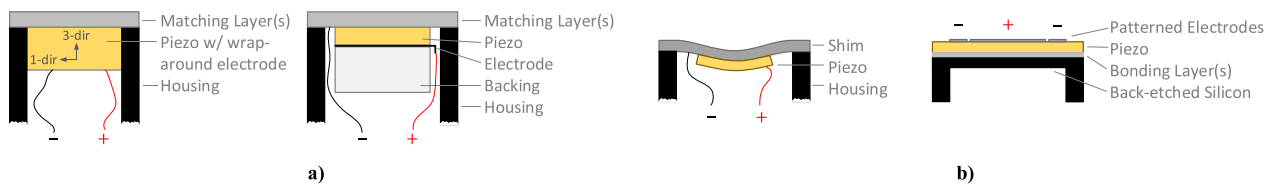
Figure 5. Two common piezoelectric structures for acoustic power transfer, (a) plate structure; (b) diaphragm structure.

will probably have similar sensitivity. Therefore, it is possible to improve the robustness of the ultrasonic receiver by operating it at lower frequencies.

Attenuation in human tissue strongly depends on the operating frequency. Attenuation in acoustics is the drop in the amplitude of the ultrasound beam as a function of distance through the human tissue. As the pressure wave travels through the medium, i.e. the human body, it is absorbed in the tissue. This reduction is expressed as:

$$I(z) = I_0 e^{-2\alpha z}, \qquad (6)$$

where I_0 is the unattenuated acoustic intensity at the face of the transmitter, and I is the attenuated acoustic intensity at distance z from the transmitter. The attenuation factor α changes with frequency based on $\alpha = \alpha_0 f$ in which f is the frequency in MHz and α_0 is the attenuation factor at 1 MHz. The attenuation factor in water is very low and near zero, however, the attenuation factor for the human body is not. The attenuation factor at 1 MHz for fresh fat and human muscle is $0.07\,\mathrm{cm}^{-1}$ and $0.15\,\mathrm{cm}^{-1}$, respectively [24]. Figure 4 shows the ratio of power at a certain distance to the unattenuated power for muscle and fat mediums in two frequencies 100 kHz, and 1 MHz. It is clear from the figure that at higher frequencies, the attenuation would be a significant problem and it is beneficial to design devices that can operate at lower frequencies.

3. Structures for ultrasonic piezoelectric power receivers

Piezoelectric power transducers are the most common types of ultrasonic receivers to convert acoustic energy into electrical energy. Two common piezoelectric structures suitable for acoustic power transfer are the plate and the diaphragm structures shown in figure 5. A bulk mode plate structure

is a piezoelectric disk operating at 3–3 mode in which the poling axis is in the same direction as the dominant strain (both perpendicular to the face of the plate). To operate at 3–3 mode, the diameter to thickness ratio of the plate needs to be in the range between 1 to 10. The resonance frequency of a plate structure only depends on its material and its thickness. A plate structure for transmitting and receiving power is most commonly used in the literature. For optimal performance, the thickness of the piezoelectric layer should be half the acoustic wavelength in the piezoelectric material. The acoustic wavelength in PZT at 1 MHz is approximately 4 mm. For the piezoelectric element to be much thinner (significantly below 1 mm) and operate efficiently, the frequency must go up. The resonance frequency has an inverse relationship with the thickness, and therefore, small receivers have a higher resonance frequency. At millimeter thicknesses, the resonance frequency is on the order of megahertz resulting in high tissue absorption. The resonance frequency for a PZT material with speed of sound 4080 m s^{-1} is plotted against the device thickness in figure 6. As discussed in the previous section, operating at high frequencies results in higher attenuation in mediums like the human body and makes devices more sensitive to orientation and alignment. Some researchers are studying the use of piezoelectric devices with an alternative and more compliant geometries as power receivers [22, 25]. This will enable a thinner device to be used efficiently at lower frequencies resulting in increased generated power.

A piezoelectric unimorph diaphragm can be utilized to more efficiently transduce the acoustic wave at very small receiver sizes. Unlike plate structures that use the thickness-mode motion of a plate, diaphragm structures are based on the flexural motion of a thin elastic layer coupled with a thin piezoelectric layer. This structure operates in 3–1 mode in which the poling axis is perpendicular to the face of the
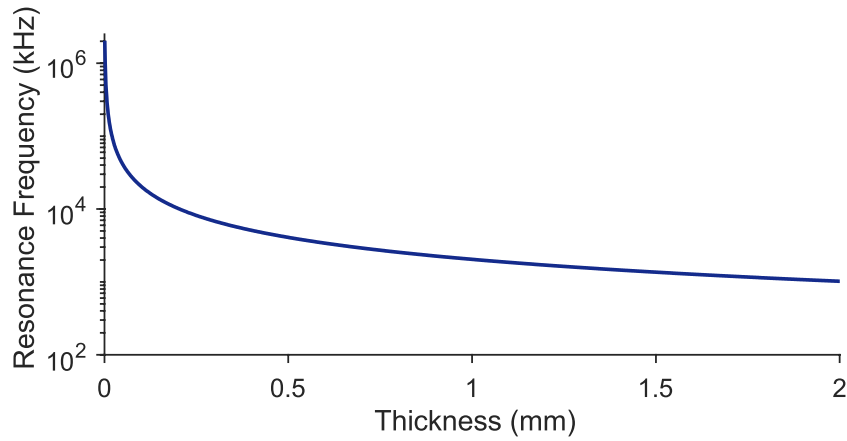
Figure 6. Resonance frequency of plate structures versus the thickness of the plate.

Table 1. Electro-mechanical properties of piezoelectric materials used in pMUTs [32, 34–36].

	Material thickness (μm)	Coupling coefficient, k_{31}^2 (%)	Relative permittivity, ε_{33}	Piezoelectric coefficient, $-d_{31}$ (pm V^{-1})
Deposited AlN	<6	3.1–8	8–10.5	1.9–2.3
Deposited PZT	<5	7–25	300–1300	10–100
Bulk PZT	>127	35	1800–3800	190–320

diaphragm (direction 3) whereas the strain is dominant in the direction parallel to the face of the diaphragm (direction 1). In a diaphragm structure, a piezoelectric layer is attached to a non-piezoelectric layer, i.e. shim, to produce a bending mode. This structure has multiple benefits compared to bulk mode plate transducer: its effective acoustic impedance is much lower than that of bulk piezoelectric, its resonance frequency is lower for a given size enabling lower frequency acoustic transmission which has reduced attenuation, and it is more easily achievable in a MEMS format. This diaphragm structure is usually referred to as a piezoelectric micromachined ultrasound transducer or pMUT if implemented as a MEMS device. The resonance frequency of the diaphragm structures is not just a function of its thickness, but depends on the diameter as well. For a similar size, the resonance frequency of a pMUT is typically more than an order of magnitude lower than a plate structure. The resonance frequency, *f*, for a circular pMUT is [26]:

$$f = \frac{1}{2\pi}\sqrt{\left(\frac{3.2}{a}\right)^4 \frac{D}{\rho}}, \qquad (7)$$

where *a* and ρ are the diaphragm radius and area mass density, respectively. *D* is the flexural rigidity of the structure and is a function of thickness (*h*), Young's modulus (*E*) and Poisson's ratio (ν) of all the layers of the diaphragm. For a unimorph diaphragm consisting of an elastic layer and a piezoelectric layer, flexural rigidity is calculated by integrating from the bottom surface of the elastic layer to the top piezoelectric layer:

$$D = \int_{h=0}^{h=h_{Elastic}} \frac{E_{Elastic}h^2}{1-\nu_{Elastic}^2}dh + \int_{h=h_{Elastic}}^{h=h_{Piezo}} \frac{E_{Piezo}h^2}{1-\nu_{Piezo}^2}dh. \qquad (8)$$

According to equations (7) and (8), it is clear that diaphragm devices with smaller thicknesses have lower

resonance frequencies that are more suitable for power transfer applications. In other words, at a given operating frequency, diaphragm structures can be smaller compared to plate structures and this makes them more suitable for our specific application of wirelessly powering IMDs. Although these equations are for a circular diaphragm, the dependency of frequency to thickness holds for a rectangular diaphragm as discussed in [27].

The piezoelectric layer of a pMUT is usually achieved by thin film deposition techniques such as sputtering [28], screen printing [29], and sol-gel spin coating [30]. Lead zirconate titanate (PZT) and aluminum nitride (AlN) are two common piezoelectric materials used in pMUTs. The electro-mechanical properties of bulk and deposited PZT, and deposited AlN are summarized in table 1. The maximum achievable thickness for current deposition techniques is about 6 μm [31]. Growing piezoelectric films thicker than a few microns is particularly challenging because of the large film stress and the tendency to form microcracks [32]. Additionally, as the thickness gets higher than 6 μm, the piezoelectric layer starts to become more porous. It is true that for two pMUTs with the same piezoelectric material thicknesses (one with PZT and one with AlN), AlN pMUTs show higher optimal receiving sensitivity due to small dielectric constant of AlN and can provide much more voltage; however, PZT can produce higher power from a device. COTS bulk piezoelectric transducers are typically available in thicknesses higher than 127 μm (0.005″). This leaves a large gap in available piezoelectric material thickness between deposited thin layers and COTS bulk transducers. As discussed in [33], the required thickness for the PZT layer in this study cannot be provided by deposition techniques nor COTS bulk transducers. In other words, in order to have a device with a relatively low resonance frequency around 100 kHz, the total diaphragm thickness around
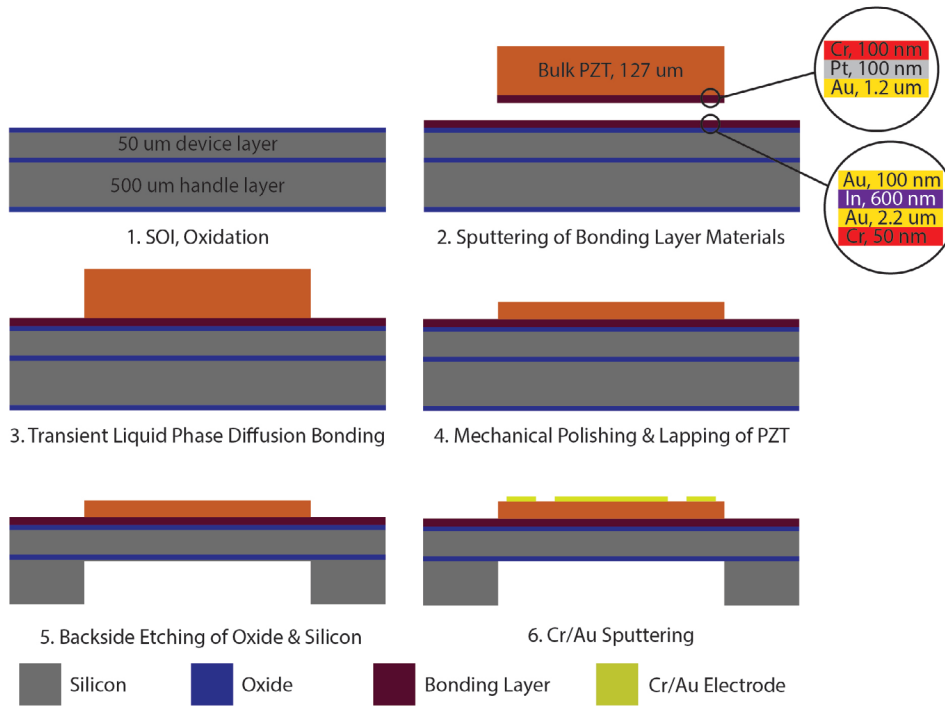
Figure 7. MEMS process flow for very thick PZT devices. The process includes bonding pre-diced pieces of bulk PZT to an SOI wafer to achieve high-quality PZT devices.
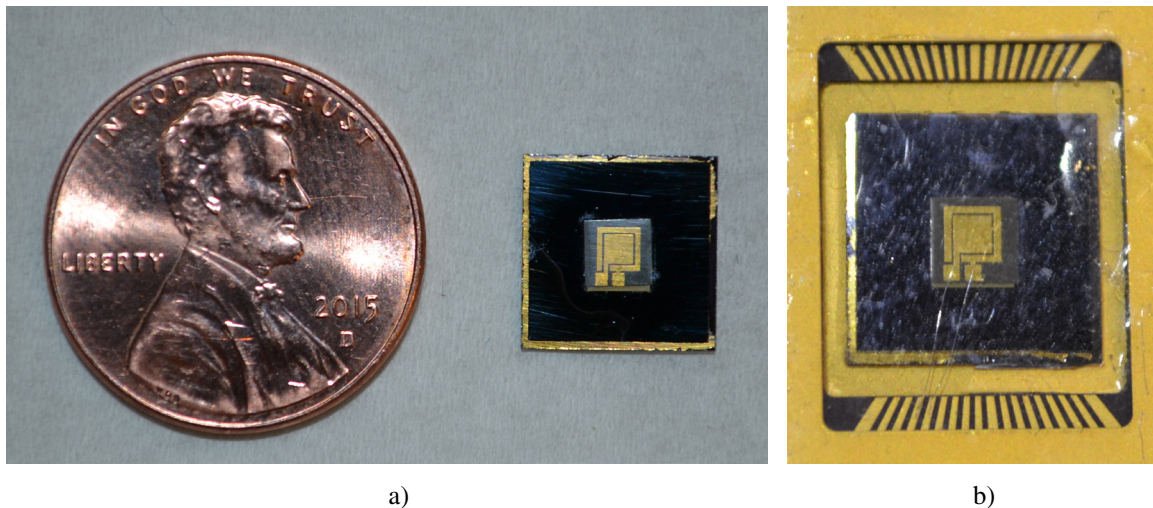
Figure 8. (a) Microfabricated PZT power receiver chip; (b) the packaged microfabricated PZT power receiver.

70 μm is required within a 4 mm^2 area to get the maximum power. A fabrication process is presented in the following section that uses bulk piezoelectric materials for pMUTs and can bridge the gap in available piezoelectric layer thicknesses.

4. Experimental test setup and model verification

We fabricated a pMUT device using the fabrication process shown in figure 7. The structure is a 2 mm × 2 mm square diaphragm consisting of a piezoelectric layer bonded to silicon. An SOI wafer is used to fabricate the device. First, the bonding layer metals were deposited on the bulk PZT-5A and SOI wafer. Then, the PZT sheet was diced into small square pieces of the desired size. The PZT pieces were then bonded

to the SOI wafer using transient-liquid-phase (TLP) diffusion bonding [37]. In this bonding technique, a low melting point interlayer metal (indium) is sandwiched in between two parent metals (gold). Using this technique, there is no need to repolarize the PZT layer since bonding occurs at low temperatures below the Curie temperature of PZT. It should be noted that the bonding layer is solid to a much higher temperature above the curie temperature after bonding. Mechanical lapping and polishing processes were performed to decrease the thickness of the bulk PZT from 127 μm to the desired thickness. The diaphragm was created by back-side deep reactive ion etch (DRIE). Finally, the top inner and outer electrodes were patterned by sputtering and lifting off of Cr/Au. Figure 8 shows photographs of the fabricated device. The fabricated pMUT was packaged and then coated with polydimethylsiloxane
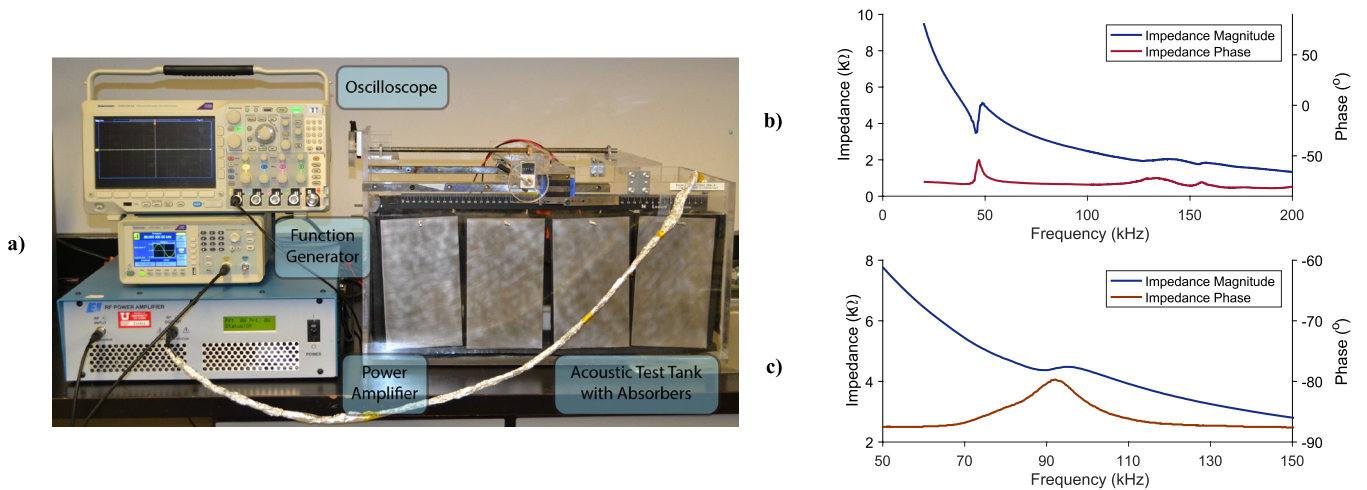
Figure 9. (a) Acoustic test setup for measuring voltage and power; (b) impedance of the bulk transmitter in water; (c) impedance of the fabricated pMUT in water.
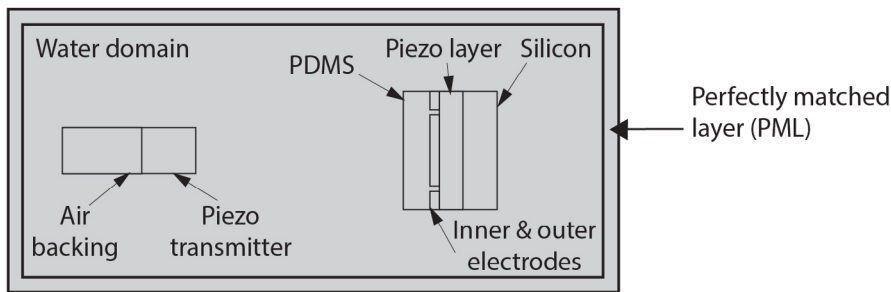
Figure 10. Schematic of the modeled system in COMSOL (top view, not drawn to scale).

(PDMS), which is a bio-compatible silicon-based organic polymer.

The fabricated pMUT was characterized, and the results can be found in a recently published paper by the authors [33]. The resonance frequency of the pMUT in air and water is 142 kHz and 88 kHz, respectively. The shift in the resonance frequency is due to the added mass effect in which an inertia is added to the system because the device displacement moves some volume of the medium. The performance of the fabricated device in transferring power was investigated in a water-filled acoustic test tank (figure 9(a)) in the presence of depth, orientation and alignment uncertainties. The test tank is a $59 \times 28 \times 28\,cm^3$ acrylic tank lined with ultra-soft polyurethane acoustic absorbers. Our test setup enables fine control of the orientation and alignment between acoustic transmitter and receiver. The transmitter is a bulk-mode piezoelectric element that is set atop an ABS tube with cyanoacrylate and sealed against water on the back side. The impedance measurement of the fabricated pMUT receiver and transmitter in water are shown in figures 9(b) and (c). The measurements were performed using an impedance analyzer (Agilent 4294A). The transmitter is powered by a Tektronix AFG1062 function generator connected to an E&I 240L power amplifier. The receiver has an optimal resistive load of $4.3\,k\Omega$ connected across its terminals. The optimal load is chosen to be equal to the impedance of the pMUT at 88 kHz. Zero to peak voltage measurements across the receiver load were recorded using a Tektronix MDO3014 oscilloscope, and the generated average

power was calculated using the measured voltage and the receiver load. The input acoustic intensity for all the experiments is set to be 322 mW cm^{-2}, which is well below the safety limit for ultrasound intensity (720 mW cm^{-2}) defined by the United States Food and Drug Administration (FDA) [38]. During the tests, the location of the receiver was changed with respect to the transmitter, and the receiver load voltage was measured and recorded. The power generated (measured and simulated) across the optimal load is plotted versus the depth of the receiver, alignment, and orientation of the receiver in figures 11–13, respectively. The voltage measurements are also provided as a practical reference as most power conditioning schemes will require a minimum voltage to operate.

The COMSOL model used in this study includes the fabricated receiver, transmitter, and the medium as shown in figure 10. Modeling techniques such as circuit equivalent models and 2D axisymmetric finite elements are unable to model the effects of orientation and alignment. While a simplified 1D model can provide a general guide, a three-dimensional (3D) model and simulation are necessary to study the effects of depth, orientation, and alignment for a square diaphragm. First, the pMUT is modeled. The lowest layer of the pMUT is silicon. On top of that, there is the piezoelectric layer made of PZT-5A. Above the piezoelectric layer are the inner and outer Au electrodes creating access to the generated AC potential. The topmost layer of the pMUT is PDMS. Both the inner and outer electrode layers are 0.3 μm thick and modeled as separate structural layers. The width of the square

Table 2. Properties of the piezoelectric material, silicon, and water medium used in the COMSOL simulations.

| | | Piezo Transmitter | pMUT | | | | Water |
	Unit		Piezo	Silicon	Gold electrodes	PDMS	
Diameter	mm	12.8					
Length	mm		2	2	1.4 (inner electrode)	2	
Thickness	mm	28.65	0.04	0.05	0.0003	0.3	
Density	kg m^{-3}	7600	7800	2330	19 300	965	1000
Speed of sound	m s^{-1}	4080	3900	8433	3240	2200	1500
Young's modulus (Y_1^E)	Pa	63×10^9	61×10^9	166×10^9	70×10^9	2.36×10^6	
Young's modulus (Y_3^E)	Pa	54×10^9	52×10^9				
Poisson's ratio		0.32	0.32	0.27	0.44	0.4	
Charge constant ($-d_{31}$)	pm V^{-1}	175	190				
Relative permittivity		1900	1800				
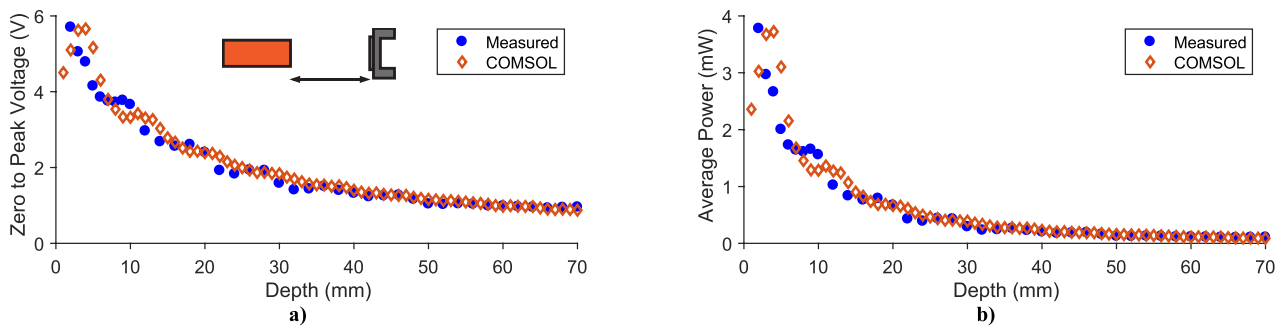
Figure 11. (a) Generated peak voltage and (b) generated average power versus receiver depth at 88 kHz at 0 mm offset and 0° angle for the fabricated pMUT.

device is 2 mm. The transmitter model consists of a piezoelectric layer and an air backing layer. The transmitter and the receiver are modeled inside a water domain. A perfectly matched layer (PML) is used to model the absorption of sound waves as they propagate far away from the sound source. The PML reduces the effect of any reflection from the edges. The dimensions of all system constituents and the material properties used for the simulations are given in table 2. The acoustic-piezoelectric interaction, frequency domain interface is used to simulate the acoustic power transfer system. The pressure acoustics interface solves the wave equation in the medium. The solid mechanics interface is solved on all structural materials including piezoelectric materials, silicon, and electrodes. Silicon is considered as an anisotropic material. The electrostatics interface is only solved on the piezoelectric material layers. The electrical equat1ions are not solved in the metallic gold layers because the electrical conductivity of gold is many orders of magnitude higher than that of PZT and hence the gold layers act as equipotential regions allowing extremely small conduction current through them. Thus, the electrical characteristics of electrode layers do not have any significant effect on the response of the pMUT. The maximum mesh element size is specified as 1/5th of the wavelength to accurately resolve the pressure waves within the inner water domain. The total number of degrees of freedom solved for is 675873 for COMSOL simulations. The COMSOL finite element simulation used 75 321 elements for the transmitter, 268 989 elements for the pMUT, and 331 563 elements for the medium.

According to figure 11, the trend of simulation and experimental data matches, and this trend indicates that the device is operating in far-field and away from the Rayleigh distance as the power profile is uniformly decreasing with depth. The operating resonance frequency 88 kHz results in a wavelength of 17.04 mm and Rayleigh distance 2 mm in water. Another important takeaway from this graph is that the system is capable of generating about 0.5 mW of average power (1 mW of peak power) in distances between 20 mm to 30 mm. The pMUT device is also capable of producing about 0.23 mW of average power (0.46 mW of peak power) at a depth of 40 mm with zero offset and angle. The generated power decreases when the receiver is moved axially away or laterally from the transducer. For example, as shown in figure 12, when the receiver has a 10 mm lateral offset, the generated power drops by about 36% and the voltage drops by 20%. The plate structure is more sensitive to change in the offset of the receiver and we will investigate this comprehensively in the next section. The results for the angle experiment (figure 13) are only valid in the angle range of −5° to +5°. This is due to the fact that the package of the pMUT is much larger than the pMUT size. When the device has an angle not in that range, the incoming acoustic wave hits the package and not the device, which can cause the voltage and the power to drop faster than predicted by simulation. In other words, the size of the package is bigger than the size of the device itself, so when we rotate the device, the upcoming pressure wave hits the package first resulting in a faster power drop in experimental data. We did not model the whole package in our COMSOL simulation.
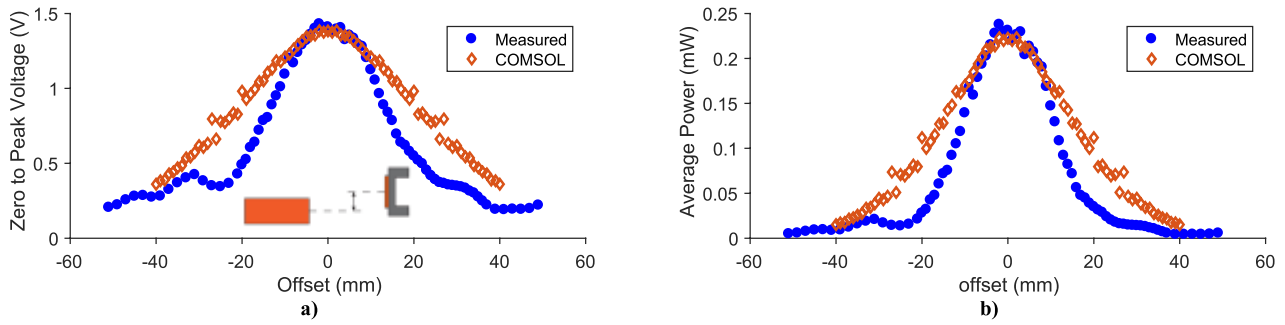
Figure 12. (a) Generated peak voltage and (b) generated average power versus receiver offset at 88 kHz at 40 mm depth and 0° angle for the fabricated pMUT.
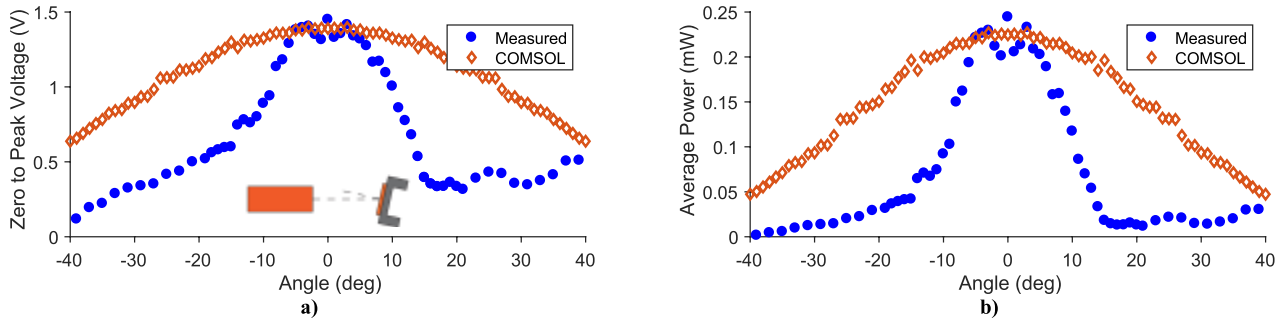
Figure 13. (a) Generated peak voltage and (b) generated average power versus receiver angle at 88 kHz at 0 mm offset and 40 mm depth for the fabricated pMUT.
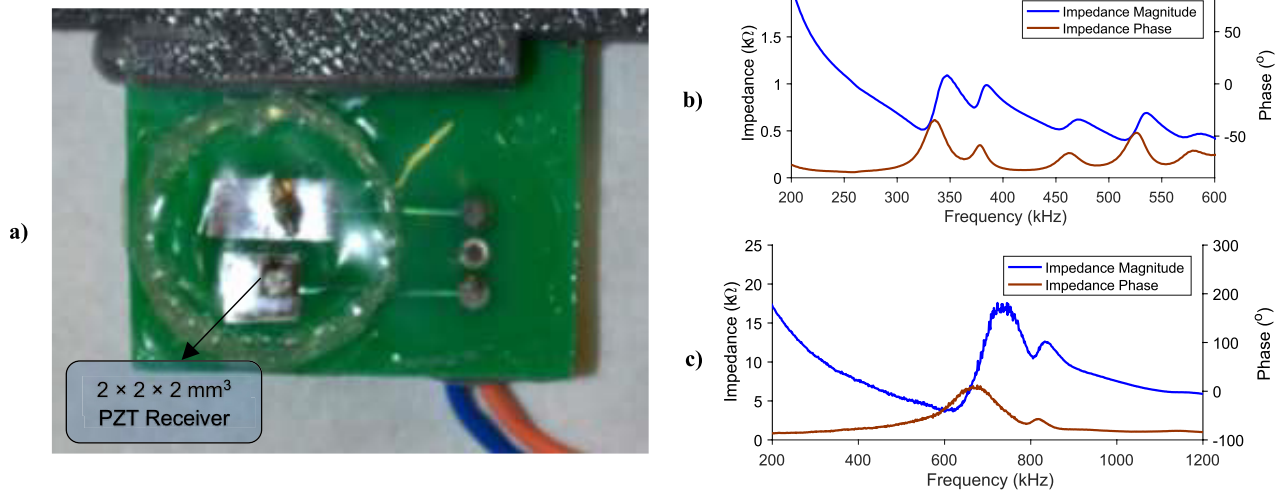
Figure 14. (a) The packaged COTS bulk receiver; (b) impedance of the bulk transmitter in water; (c) impedance of the COTS bulk receiver in water.

5. Generated power and sensitivity comparison

To compare the results of our pMUT to a COTS bulk piezo-electric transducer, we used a bulk PZT with a similar area to the fabricated device. Please note that we did not match the thickness of the COTS transducer to our pMUT since it would result in a very high resonance frequency. The COTS device is a $2 \times 2 \times 2$ mm^3 PZT-5A and is attached to a PCB and coated with PDMS as shown in figure 14(a). The COTS bulk receiver was tested in the same acoustic tank. The device was characterized in air and water. The resonance frequency of the device in air and water is 658 kHz and 628 kHz, respectively. The

resonance frequency slightly drops for plate structures as they have smaller displacement compared to diaphragm structures. We chose another transmitter that has a similar resonance frequency to the receiver, which is a bulk-mode piezoelectric element that is set atop an ABS tube with cyanoacrylate and sealed against water on the back side. The piezoelectric element is 12.7 mm in diameter, 3.43 mm thick, and has a standard separate electrode on each face. The impedance results of the bulk receiver and transmitter in water are shown in figures 14(b) and (c). The impedance response of the transmitter shows some lower frequency peaks, which are from the radial vibration mode and harmonics. The impedance of the COTS
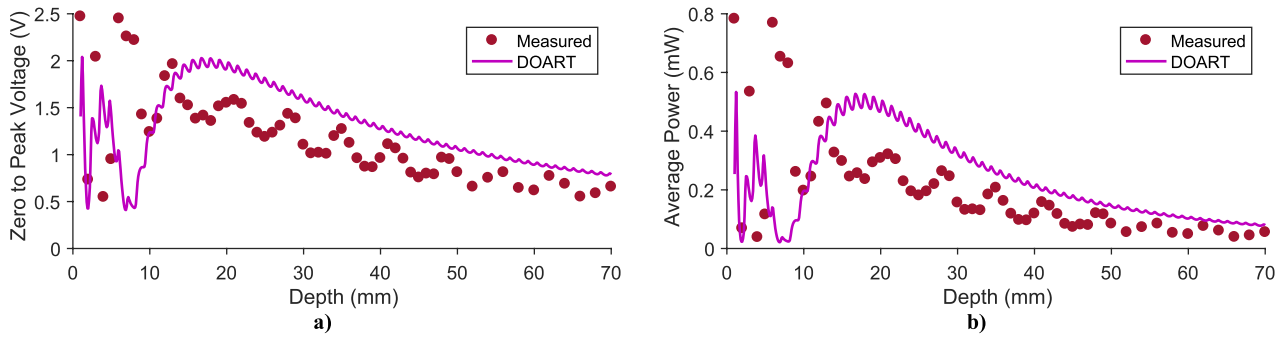
Figure 15. (a) Generated peak voltage and (b) generated average power versus receiver depth at 88 kHz at 0 mm offset and 0° angle for the COTS bulk receiver.
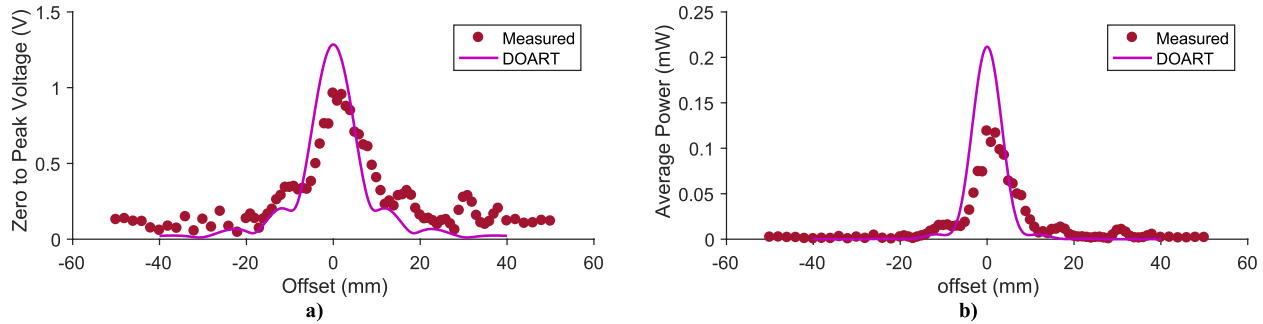
Figure 16. (a) Generated peak voltage and (b) generated average power versus receiver offset at 88 kHz at 40 mm depth and 0° angle for the COTS bulk receiver.

device at its resonance frequency is 3.9 kΩ. This was chosen as the optimal load of the bulk transducer. We measured the voltage and calculated the power across the optimal load as a function of depth, offset, and angle for the input power of 322 mW cm⁻² at 628 kHz.

Although 3D finite element analysis has the capabilities to model the effects of orientation and alignment, the computational cost is very high as the operating frequency of the acoustic power transfer system goes up. As the frequency goes up, the wavelength becomes shorter, and more elements are needed in meshing the geometry. In order to efficiently model the effects of orientation and alignment in high frequencies, we employed a modeling technique that models the effect of depth, orientation, and alignment via ray tracing (DOART) as presented in [39]. This technique uses Huygens principle to discretize the face of the transmitter into spherically radiating pressure sources. It can be utilized to determine the power transferred to the receiver for any position and orientation. DOART provides a reduction in computational cost that enables a more thorough exploration of the design and operational space of acoustic power transfer systems. Therefore, the measured voltage and power of the COTS bulk receiver are plotted against depth, offset and angle in figures 15–17 and compared with DOART. DOART is capable of modeling circular transducers and not rectangular ones. It also considers an air backing layer for the transducers, which is not the case in our COTS receiver. With these considerations, we modeled a circular receiver with the same area size to our rectangular COTS receiver and used DOART. The general overpredicting of DOART in voltage values can be attributed to the fact that air backing will result in a better performance. The trend of

measured data is in agreement with DOART data. Depth measurements were taken from 1 mm to 70 mm at 0° angle and 0 mm offset. Irregular voltage patterns occur in the near-field; however, the voltage profile becomes more uniform from about 17 mm depth. The device is capable of producing about 0.12 mW of average power (0.24 mW of peak power) at a depth of 40 mm with zero offset and angle. The generated voltage and power in far-field fluctuate when the axial distance between the transmitter and receiver changes because of acoustic standing waves reflecting back and forth between the transmitter and receiver. The package is not modeled in DOART, which makes the standing waves not as strong as for the measured data. When the transmitter and receiver are relatively close together, the reflection activity between them increases. In the far-field, there would be zero fluctuation in voltage and power if the receiver were perfectly acoustically matched to the medium. The difference between the measured and simulated voltages particularly in the near-field may be attributed to several factors. There may be an error in setting the zero distance between the transmitter and the receiver in the experiment which results in a shift in the experimental data. Also, the fact that DOART models a circular receiver with air backing instead of a rectangular one may result in a different performance.

The performance of the COTS is compared to the pMUT structure. Figure 18 shows the measured average power and voltage versus depth for the pMUT and COTS device over the 20–60 mm depth range when angle and offset are equal to zero. This is the range in which both receivers operate at far-field. The results show that voltage and power generally decrease when the depth increases due to beam divergence
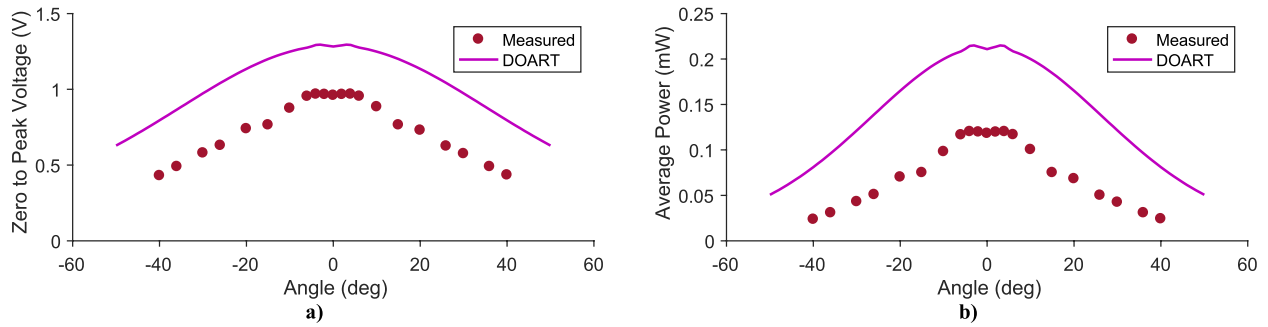
Figure 17. (a) Generated peak voltage and (b) generated average power versus receiver angle at 88 kHz at 0 mm offset and 40 mm depth for the COTS bulk receiver.
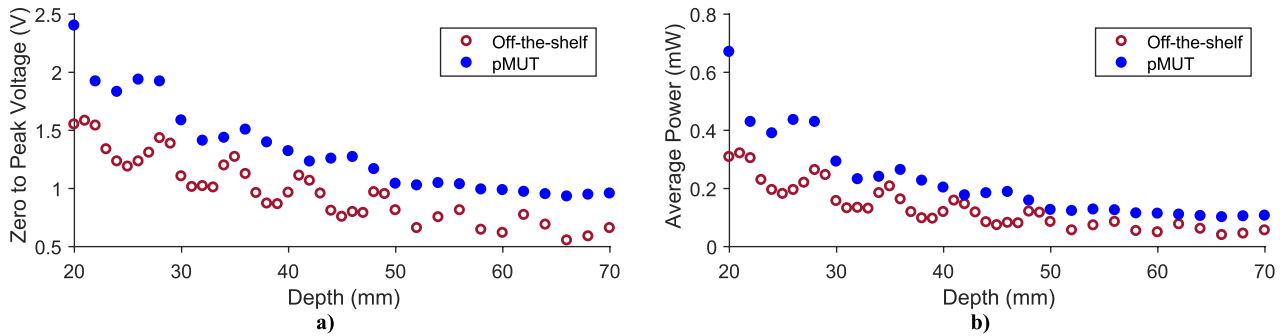
Figure 18. (a) Generated peak voltage and (b) generated average power versus receiver depth at 0 mm offset and 0° angle for the pMUT device and COTS bulk receiver.
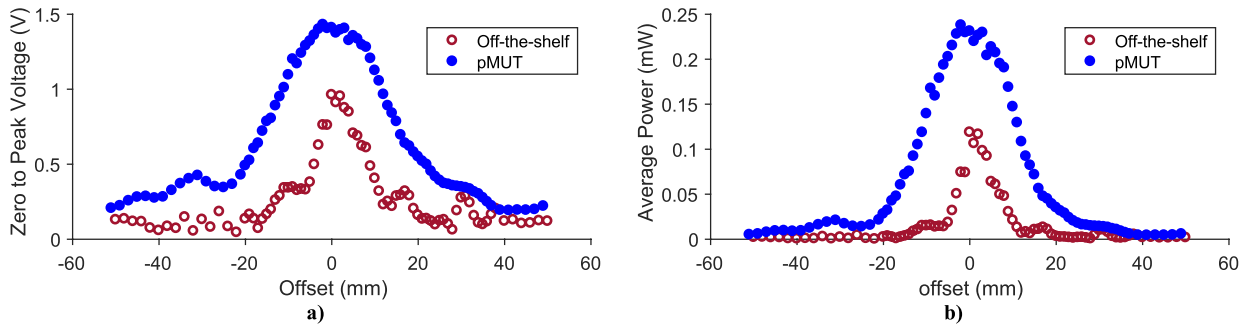
Figure 19. (a) Generated peak voltage and (b) generated average power versus receiver offset at 40 mm depth and 0° angle for pMUT device and COTS bulk receiver.

and absorption. Although the COTS device is less sensitive to change in the depth in shallow depths, it has a similar sensitivity to the pMUT as the depth increases. Please note that these results are in a water medium, which has a very low attenuation. In the real applications in the human tissue, the sensitivity to depth of a plate structure would increase more than a diaphragm structure due to operating at higher frequencies as discussed in section 2 of this paper. The diaphragm structure has a lower acoustic impedance compared to a plate structure. This results in lower reflection from the face of the pMUT and better performance since its acoustic impedance is closer to water. The pMUT seems to generate slightly more voltage and power at any depth compared to the COTS device. This is in agreement with the numerical results published in [21] in which a diaphragm structure at about 4 mm² size scale would generate slightly higher power numbers compared to a plate structure with the same size at depths higher than 20 mm when a same acoustic input is applied.

The measured voltage and power versus offset for the pMUT and COTS devices are shown in figure 19. These measurements were conducted at 40 mm depth and zero angle. This depth was chosen as it is far away from Rayleigh distances of both receivers and it is also in an acceptable depth range for implants. As the offset between the transmitter and receiver increases, the receiver captures less of the transmitted power. The pMUT is operating at 88 kHz, and the COTS device is operating at 628 kHz. Disturbances in the generated voltage and power are a strong function of frequency since higher frequencies result in a narrower beam as discussed in section 2. Therefore, the generated voltage and power of a diaphragm structure are less sensitive to the changes in offset of the implants as expected. When the transmitter and receiver become misoriented, the pressure profile on the face of the receiver changes resulting in smaller average pressure on its face. Figure 20 shows the generated voltage and power of pMUT and COTS device versus angle. As the pMUT
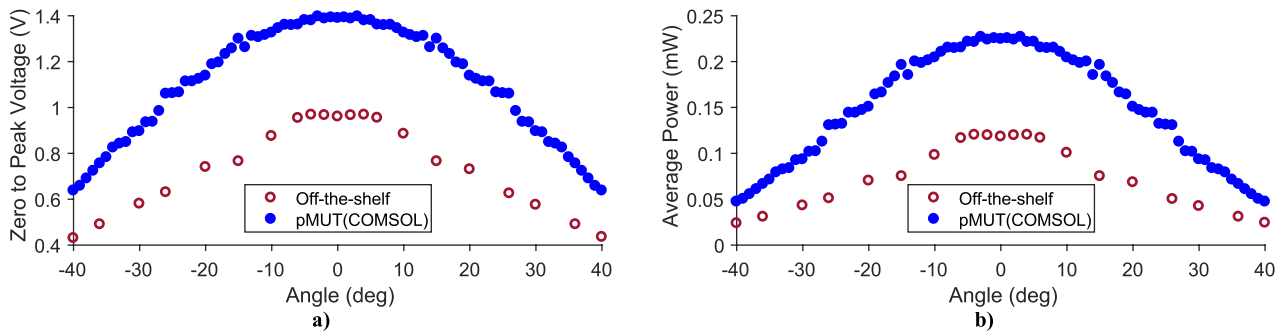
Figure 20. (a) Generated peak voltage and (b) generated average power versus receiver angle at 0 mm offset and 40 mm depth for pMUT device and COTS bulk receiver.

Table 3. Comparison between the performance of our fabricated pMUT and a COTS receiver.

	pMUT Structure	COTS Structure
PZT size	$2\,mm \times 2\,mm \times 40\,\mu m$	$2\,mm \times 2\,mm \times 2\,mm$
Resonance frequency	88 kHz	628 kHz
Optimal load	4.3 kΩ	3.9 kΩ
Peak input electrical power	417.7 mW (322 mW cm^{-2})	417.7 mW (322 mW cm^{-2})
Output voltage at 40 mm depth, 0 mm offset and 0° angle	1.41 V	0.96 V
Average output power at 40 mm depth, 0 mm offset and 0° angle	0.23 mW	0.12 mW
Half power offset	11 mm	3 mm
Half power angle	27°	20°
Efficiency at 40 mm depth, 0 mm offset and 0° angle	0.11%	0.057%
Efficiency at 20 mm depth, 0 mm offset and 0° angle	0.32%	0.15%
Area normalized efficiency at 40 mm	3.54%	1.83%
Area normalized efficiency at 20 mm	10.29%	4.82%

measured data for the angle is not valid at large angles due to the way we packaged the device, we used COMSOL data for the angle comparison. Note that the way we package the COTS device does not affect its angle performance since the incoming acoustic wave can still hit the edges of the misoriented device.

6. Discussion

To quantify the comparison between the pMUT and COTS devices, we defined average percentage improvements in power for all the considered depths, offsets and angles as the ratio of difference in generated power from pMUT and COTS over the generated power of COTS. The average percentage improvement in power are 86%, 917%, and 111% for figures 18–20, respectively. These percentage improvements are the average improvement over all data points shown in figures 18–20. However, as is visually evident, the percentage improvement near zero offset or angle is much lower. At zero offset, for example, the percentage improvement in power is 94%. As the offset increases, the power from pMUT and COTS devices both drop; however, power from COTS device drops much faster. Therefore, at large offsets there are big differences in power numbers between pMUT and COTS devices even when power numbers are relatively very low. The percentage improvement in power for offsets of −5, −10, −20, and −30 mm are 994%, 831%, 1087%, 847%, respectively. This shows the pMUT is capable of providing better

power compared to the COTS device. To better compare the performance of two receivers, we also defined a half power offset and angle for the pMUT and COTS devices as the offsets and angles at which power drops by 50%. The comparison results are summarized in table 3.

The output power from both structures is high enough to power an IMD. The power required for IMDs is generally on the order of hundreds of microwatts to tens of milliwatts at the extreme high end [2, 3]. The voltages are also large enough for rectification purposes. The efficiency of the acoustic power transfer system, which is defined by the ratio of generated output power to the input power, may seem low; however, it is higher than the efficiency of similarly sized RF power transmission systems [2]. Furthermore, the efficiency can be improved by addressing two main sources of loss in the current setup. First, the diameter of the transmitter is larger than the receiver, and much of the acoustic energy transmitted is not captured by the receiver. This can be explained by calculating the area normalized efficiency in table 3 as defined in [11]. The area normalized efficiency (the ratio of output power intensity to input power intensity) is a useful metric when the transmitter is large, and the receiver is small. Second, the reflection between the face of the transmitter and water due to acoustic impedance mismatch significantly reduces efficiency. The generated output power can be improved by applying input power intensity closer to the FDA limit and also using matching layers for the transmitter to reduce the reflection between the transmitter and the medium, which were not the focus of this paper. Regarding sensitivity to the location of the

receiver, the half power angle and half power offset are larger for the fabricated pMUT compared to the COTS device. As the size of the receiver decreases, the sensitivity will become more of a major issue for the plate structure as power degrades significantly with implant location because its resonance frequency is very high.

7. Conclusion

In this paper, we presented a MEMS ultrasonic power receiver for powering IMDs, and studied the effect of depth, angle, and offset on the generated power. We developed a 3D COMSOL model and compared the results to the measured data. There is acceptable agreement between the COMSOL simulation and experimental results. The pMUT device is less sensitive to location uncertainties compared to a COTS plate mode transducer with a size similar to the fabricated pMUT. Future work includes addressing the performance of the pMUT device in a full system where the received power can be used to power a bio-medical implant. The fabricated pMUT shows great potential for powering IMDs as it can generate sufficient power (0.23 mW) at large depths. (i.e. 40 mm) and is less sensitive to misorientation and misalignment between transmitter and receiver.

Acknowledgment

ORCID iDs

Hamid Basaeri ⬤ https://orcid.org/0000-0002-7657-2916

References

[1] Wei X and Liu J 2008 Power sources and electrical recharging strategies for implantable medical devices *Frontiers Energy Power Eng. China* **2** 1–13
[2] Ho J S *et al* 2014 Wireless power transfer to deep-tissue microimplants *Proc. Natl Acad. Sci. USA* **111** 201403002
[3] Eshaghian-Wilner M M (ed)2016 *Wireless Computing in Medicine: from Nano to Cloud with Ethical and Legal Implications* (New York: Wiley)
[4] Ben Amar A, Kouki A B and Cao H 2015 Power approaches for implantable medical devices *Sensors* **15** 28889–914
[5] Karami M and Inman D 2012 Powering pacemakers from heartbeat vibrations using linear and nonlinear energy harvesters *Appl. Phys. Lett.* **100** 042901
[6] Ansari M and Karami M 2016 Modeling and experimental verification of a fan-folded vibration energy harvester for leadless pacemakers *J. Appl. Phys.* **119** 094506
[7] Roundy S and Wright P 2004 A piezoelectric vibration based generator for wireless electronics *Smart Mater. Struct.* **13** 1131
[8] Silay K, Dehollain C and Declercq M 2011 Inductive power link for a wireless cortical implant with two-body packaging *IEEE Sens. J.* **11** 2825–33

[9] Lu X, Wang P and Niyato D 2015 Wireless networks with RF energy harvesting: a contemporary survey *IEEE Commun. Surv. Tutorials* **17** 757–89
[10] Basaeri H and Roundy S 2017 A micromachined ultrasonic power receiver for biomedical implants *Proc. SPIE* **10164** 1016416
[11] Basaeri H, Christensen D B and Roundy S 2016 A review of acoustic power transfer for bio-medical implants *Smart Mater. Struct.* **25** 123001
[12] Basaeri H, Christensen D, Yu Y, Nguyen T, Tathireddy P and Young D J 2016 Ultrasonically powered hydrogel-based wireless implantable glucose sensor *2016 IEEE Sensors Proc.* pp 1–3
[13] Meng M and Kiani M 2017 Design and optimization of ultrasonic wireless power transmission links for millimeter-sized biomedical implants *IEEE Trans. Biomed. Circuits Syst.* **11** 98–107
[14] Shmilovitz D, Ozeri S, Wang C-C and Spivak B 2014 Noninvasive control of the power transferred to an implanted device by an ultrasonic transcutaneous energy transfer link *IEEE Trans. Biomed. Eng.* **61** 995–1004
[15] Shi Q, Wang T and Lee C 2016 MEMS based broadband piezoelectric ultrasonic energy harvester (PUEH) for enabling self-powered implantable biomedical devices *Sci. Rep.* **6** 24946
[16] Seo D *et al* 2016 Wireless recording in the peripheral nervous system with ultrasonic neural dust neuron neuroresource wireless recording in the peripheral nervous system with ultrasonic neural dust *Neuron* **91** 1–11
[17] Fowler A G and Moheimani S O R 2016 4-DOF SOI-MEMS ultrasonic energy harvester *IEEE-NANO 2015—15th Int. Conf. Nanotechnology* pp 1481–4
[18] Banerji S, Goh W L, Cheong J H and Je M 2013 CMUT ultrasonic power link front-end for wireless power transfer deep in body *2013 IEEE MTT-S Int. Microwave Workshpo Series RF Wireless Technologies Biomedical Healthcare Applications, IMWS-BIO 2013—Proc.* pp 1–3
[19] Smyth K M 2017 Piezoelectric micro-machined ultrasonic transducers for medical imaging Massachusetts Institute of Technology
[20] Wang Z, Zhu W, Tan O K, Chao C, Zhu H and Miao J 2005 Ultrasound radiating performances of piezoelectric micromachined ultrasonic transmitter *Appl. Phys. Lett.* **86** 1–3
[21] Christensen D B and Roundy S 2016 Ultrasonically powered piezoelectric generators for bio-implantable sensors: plate versus diaphragm *J. Intell. Mater. Syst. Struct.* **27** 1092–105
[22] Shi Q, Wang T, Kobayashi T and Lee C 2016 Investigation of geometric design in piezoelectric microelectromechanical systems diaphragms for ultrasonic energy harvesting *Appl. Phys. Lett.* **108** 106–11
[23] Christensen D 1988 *Ultrasonic Bioinstrumentation* (New York: Wiley)
[24] Goss S A, Johnston R L and Dunn F 1980 Compilation of empirical ultrasonic properties of mammalian tissues. II *J. Acoust. Soc. Am.* **68** 93–108
[25] Wang T, Kobayashi T and Lee C 2015 Micromachined piezoelectric ultrasonic transducer with ultra-wide frequency bandwidth *Appl. Phys. Lett.* **106** 013501
[26] Lu Y and Horsley D A 2015 Modeling, fabrication, and characterization of piezoelectric micromachined ultrasonic transducer arrays based on cavity SOI wafers *J. Microelectromech. Syst.* **24** 1142–9
[27] Choi H S, Anderson M J, Ding J L and Bandyopadhyay A 2010 A two-dimensional electromechanical composite plate model for piezoelectric micromachined ultrasonic transducers (pMUTs) *J. Micromech. Microeng.* **20** 015013
[28] Mehdizadeh E and Piazza G 2018 Through-package wireless powering via piezoelectric micromachined

ultrasonic transducers *Proc. IEEE Int. Conf. Micro Electro Mechanical Systems* (*January*) pp 1076–9

[29] Hindrichsen C G, Lou-Moller R, Hansen K and Thomsen E V 2010 Advantages of PZT thick film for MEMS sensors *Sensors Actuators* A **163** 9–14

[30] Pardo L J, Jiménez R, García A, Brebøl K, Leighton G and Huang Z 2010 Impedance measurements for determination of elastic and piezoelectric coefficients of films *Adv. Appl. Ceram.* **109** 156–61

[31] Cassella C and Piazza G 2015 AlN two-dimensional-mode resonators for ultra-high frequency applications *IEEE Electron Device Lett.* **36** 1192–4

[32] Fu Y Q *et al* 2017 Advances in piezoelectric thin films for acoustic biosensors, acoustofluidics and lab-on-chip applications *Prog. Mater. Sci.* **89** 31–91

[33] Basaeri H, Yu Y, Young D and Roundy S 2019 A MEMS-scale ultrasonic power receiver for biomedical implants *IEEE Sens. Lett.* **3** 2501104

[34] Trolier-Mckinstry S and Muralt P 2004 Thin film piezoelectrics for MEMS *J. Electroceram.* **12** 7–17

[35] Khan A, Abas Z, Kim H S and Oh I 2016 Piezoelectric thin films: an integrated review of transducers and energy harvesting *Smart Mater. Struct.* **25** 053002

[36] Piezo Systems 2019 PSI-5A4E piezoceramic sheets and their properties, piezo systems, Inc (https://support.piezo.com/article/62-material-properties)

[37] Aktakka E E, Peterson R L and Najafi K 2013 Wafer-level integration of high-quality bulk piezoelectric ceramics on silicon *IEEE Trans. Electron Devices* **60** 2022–30

[38] FDA 2008 Guidance for industry and FDA staff information for manufacturers seeking marketing clearance of diagnostic ultrasound systems and transducers

[39] Christensen D B, Basaeri H and Roundy S 2017 A computationally efficient technique to model depth, orientation and alignment via ray tracing in acoustic power transfer systems *Smart Mater. Struct.* **2006** 125020

CHAPTER 5

STUDY THE EFFICIENY OF ACOUSTIC POWER TRANSFER

SYSTEMS AND RADIO FREQUENCY SYSTEMS

5.1 Introduction

In this project, an ultrasonic power receiver suitable for powering implantable devices is developed. The fabricated device is capable of providing sufficient and stable power to deeply implanted biomedical devices. In this chapter, we focus on the efficiency of acoustic power transfer systems and compare them to RF systems under similar conditions. It should be stated that the comparison presented in this chapter is preliminary. In order to compare our acoustic power transfer system to an RF system, we use prior published studies and anecdotal experimental data from our close collaborators on this project (primarily Yuechuan Yue and Prof. Darrin Young) from the Department of Electrical and Computer Engineering at the University of Utah. More on their detailed work on RF power transfer for bio medical implants can be found in [1] and [2]. RF power transfer systems perform much better than acoustics in air. Acoustic waves travel much better in mediums such as water or tissue compared to air. Therefore, below is a summary aiming to answer one paramount question: Is acoustic power transfer more efficient than RF for powering deeply implanted medical devices?

The efficiency is defined by the ratio of generated output power to the input power.

In this chapter, the concept of the area normalized efficiency is discussed in more detail, and then the efficiency of an acoustic power transfer system is compared to an RF system when the distance between the transmitter and receiver is the same.

5.2 Area Normalized Efficiency

Although efficiency can give a good insight into the effectiveness of power transfer, it does not consider the dependence of input and output power to the device size. In other words, the best efficiency is usually achieved when the transmitter and receiver have the same size. However, this may not always be desirable for a couple of reasons. First, as the implant could be very small (on the order of mm^2), it would be difficult to ensure that a similarly sized transmitter was well aligned. In other words, it is useful for the acoustic beam emanating from the transmitter to be much larger than the size of the receiver. Second, for the case of acoustic power transfer, a very small transmitter would have a large acoustic beam divergence, which is undesirable. Furthermore, in many cases for wirelessly powering implantable devices the critical issue is the power generated by, and the size of, the receiver, not the overall efficiency. Therefore, output power intensity, the ratio of output power to the receiver area, is another useful metric to consider. The area normalized efficiency (the ratio of output power intensity to input power intensity) is a useful metric, particularly for acoustic power transfer, when the transmitter is large, and the receiver is small [4].

The experimental efficiency data of an acoustic power transfer system versus depth with the same size receiver and transmitter is plotted in Fig. 5.1. The transmitter and receiver are piezoelectric disks with 12.8 mm diameter, and 1.9 mm thickness. The

operating frequency is set to be the resonance frequency of the transmitter and receiver, which is 1.06 MHz. The oscillation of the efficiency suggests that the data were recorded at near-field. The wavelength and Rayleigh distance for this frequency and transducer are 1.4 mm and 29.2 mm, respectively. The spatial oscillation in the data is due to the standing wave effect and the reflection between the transmitter and receiver. This oscillation occurs at around every half of the wavelength. Note that, the area normalized efficiency in this case is equal to the efficiency since the area of the receiver and transmitter are the same. If a smaller receiver is used, the efficiency would certainly drop because the diameter of the transmitter would be larger than the receiver, and much of the acoustic energy transmitted would not be captured by the receiver. Fig. 5.2 shows the experimental efficiency data for a piezoelectric disk transmitter with 12.8 mm diameter, and the fabricated pMUT receiver that has a smaller area. The operating frequency is 88 kHz, which is the resonance frequency of the pMUT in water. The wavelength and Rayleigh distance in this case are 17 mm, and 2 mm, respectively. Therefore, there is almost no near-field region and the pMUT device operates in the far-field. As the area of the transmitter and receiver are not the same in this case, the area normalized efficiency is not equal to the efficiency. The area normalized efficiency is plotted in Fig. 5.3. If a larger transmitter is used, the Rayleigh distance would be longer, enabling the pMUT to operate in the near-field which would improve the power output. The area normalized efficiency of the pMUT at small depths is around 50% based on the data shown in Fig. 5.3. As will be shown, with a larger transmitter diameter, the area normalized efficiency would be of similar magnitude.
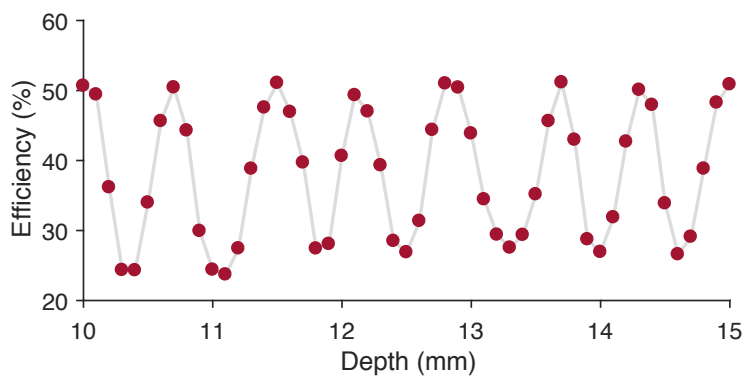
Figure 5.1. Efficiency of an APT system with a same size receiver and transmitter versus depth.
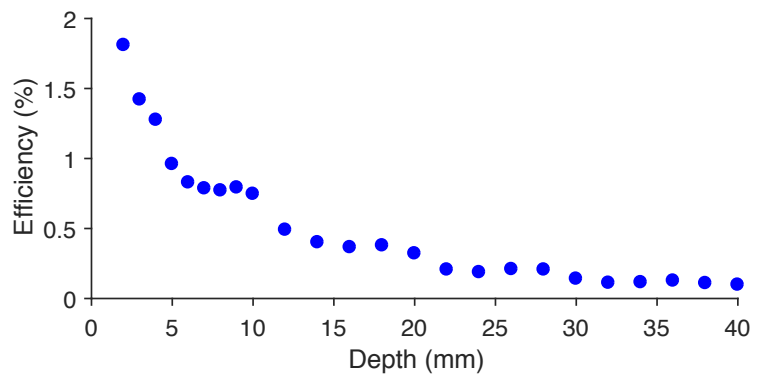
Figure 5.2. Efficiency of an APT system with the fabricated pMUT and large transmitter.
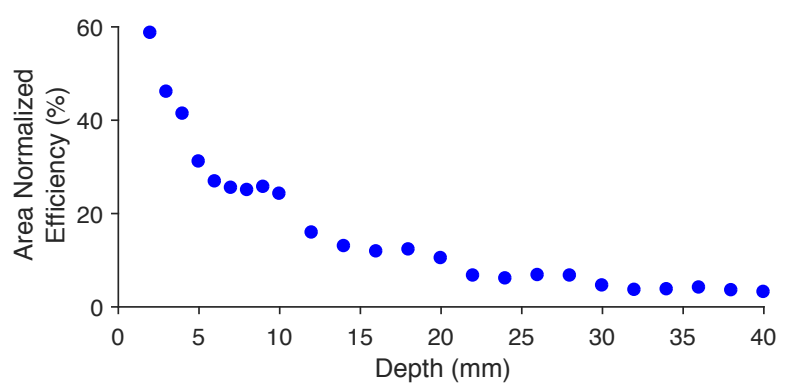
Figure 5.3. Area normalized efficiency of an APT system with the fabricated pMUT and large transmitter.

Using (1) to (4) presented in Chapter 4, the acoustic intensity is plotted in Fig. 5.4 for the circular transmitter used for pMUT but with two different diameters of 12.8 mm and 25.6 mm. The Rayleigh distance increases with the increase in the transmitter diameter. Thus, the receiver is more likely to be in the near-field when the Rayleigh distance is longer. It should be mentioned that the input power intensity at the transmitter face is the same for both cases in Fig. 5.4, which results in higher input power for the larger transmitter. When the receiver is in the near-field, it generally receives higher power intensity with the larger transmitter. For instance, at 30 mm depth, doubling the size of transmitter diameter (25.6 mm instead of 12. 8 mm) would result in about 13 times higher output power intensity. As the area of the receiver has not changed, the output power would also increase by 13 times. However, the input power increases by 4 times. Therefore, the efficiency should go up by about 3.2 times when the receiver is at 30 mm depth and the transmitter is 25.6 mm in diameter. This is also shown with COMSOL simulations in Table 5.1 as the transmitter diameter changed to 25.6 mm, the output power and efficiency would be 4.4 mW, and 0.53%, respectively, for the pMUT device. Please note that increasing the diameter of the transmitter does not always increase the efficiency as it increases both input and output powers.
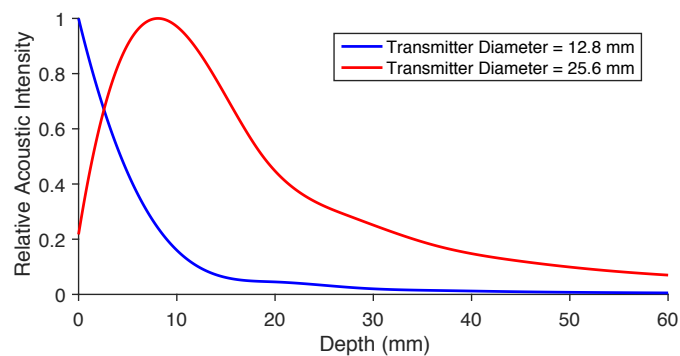
Figure 5.4. Relative on-axis acoustic power intensity magnitude from a transducer at one particular time $t = 0$.

Table 5.1 COMSOL simulations for two transmitters with the same acoustic intensity

Transmitter diameter (mm)	Input power (mW)	Input power intensity (mW/cm^2)	Average output power of the receiver (mW)	Output power intensity (mW/cm^2)	Efficiency	Area normalized efficiency
12.8	207	163.4	0.29	7.25	0.14%	4.5%
25.6	828	163.4	4.4	110	0.53%	67.3%

It should be noted that in order to know the efficiency of the pMUT device, the acoustic intensity was measured with a hydrophone (RESON TC 4038) in several distances from the transmitter for the same electrical input power to the transmitter. At depth 30 mm, the pressure is about 22 kPa. This is just the peak pressure on the pressure axis of the transmitter. Assuming this pressure is being applied on all the points on the receiver surface, the acoustic intensity at depth 30 mm would be 32.3 mW/cm^2. Therefore, that means that the acoustic power at the receiver face is about 1.29 mW. We can then conclude that the efficiency of the pMUT itself is about 45%.

5.3 Efficiency of APT compared to RF

The efficiency of an RF power transfer system is compared to APT systems in Table 5.2 when the distance between the transmitter and receiver is set to be 30 mm. The input power intensity to the pMUT systems is about half of the safety limit defined by FDA which is 720 mW/cm^2 peak power [5]. (The power numbers shown in Table 5.2 are RMS power, so the peak transmit powers are twice the values reported in the table.) The RF receiver is a solenoid with 3 mm diameter and 7 mm height. The efficiency reported in Table 5.2 for this system is in air and for a frequency of 10 MHz. Water should probably not degrade the efficiency too much because the frequency is relatively low. The total

attenuation loss at 10 MHz in water is below 6 dB for depths less than 50 cm [6]. Attenuation is low unless transmitter coil is put right next to water (0 mm air gap). There should be about 2mm air gap in between to prevent attenuation. Another RF system from Poon et. al. [3] is reported in Table 5.2. They have proposed midfield RF wireless power transfer to implants in the GHz frequency range where the coupling is in the midfield (i.e., at the transition between near-field and far-field). By using multiple transmitting antennas, they produce a constructive interference effect at the implant. The receiver antenna is a 2 mm diameter coil, giving a power intensity at the receiver of 11.33 mW/cm^2 (113.3 μW/mm^2). The safety limits for RF power exposure in this frequency range are 10 and 2 W/kg [7] for occupational and general public exposure, which correspond to 10 and 2 μW/mm^3. The safety regulations are measured as an average over 10 grams, roughly 10 cm^3. Therefore, it would seem that this power density is only achievable by locally exceeding the safe power level averaged over 10 grams.

Two different APT systems are included in Table 5.2: experimental results from a bulk piezoelectric structure with a diameter smaller than the diameter of the RF receiver (in this case the area of the transmitter and receiver are equal); and experimental results from the fabricated pMUT. Note that as the size of the receiver in an acoustic power transfer system decreases while the size of the transmitter is fixed, the efficiency decreases as well. However, the area normalized efficiency would remain constant. An acoustic power transfer system with a similar size transmitter and receiver, each with a diameter of 12.8 mm, has a higher efficiency compared to the RF systems in Table 5.2. However, the efficiency of the first RF system in Table 5.2 (3.3%) is higher than the fabricated pMUT. As noted above, the efficiency of the pMUT can be slightly improved when a bigger

transmitter is used. As the separation distance for the RF system is small compared to the transmitter size, if the transmitter size were closer to size of the transmitter for pMUT, the 3.3% efficiency at 30 mm would likely decrease. However, as it is not within the scope of this comparison to do a fully exploration of the RF transfer efficiency, we have not determined the exact amount of this decrease. The efficiency of an APT system can also be improved by using matching layers for the transmitter to reduce the reflection between the transmitter and the medium. This reflection between the face of the transmitter and water due to acoustic impedance mismatch significantly reduces efficiency.

Table 5.2 Comparison of the efficiency of RF systems to APT systems

	APT		RF	
	Bulk	pMUT	Yu & Young	Poon [3]
Transmitter size	12.8 mm diameter	12.8 mm diameter	70 mm – spiral coil	6 cm × 6 cm
Receiver size	12.8 mm diameter	2 mm × 2 mm	3 mm diameter - 7 mm height solenoid	2 mm diameter
Depth (mm)	30	30	30	30
Medium	Water	Water	Air	Tissue
Frequency	1.06 MHz	88 kHz	10 MHz	1.6 GHz
Ratio of depth to transmitter area	0.23	0.23	0.0078	0.0083
RMS Input Power (mW)	32.6	207	11.8	500
RMS output power of the receiver (mW)	15.16	0.29	0.39	0.356
Output power intensity (mW/cm^2)	11.97	7.25	5.52	11.33
Efficiency	46.5%	0.14%	3.3%	0.07%
Area normalized efficiency	46.5%	4.5%		

The area normalized efficiency is not reported for RF systems in Table 5.2. The concept of area normalized efficiency is not very applicable for RF power transfer because the physics are not similar to acoustics. In order to define area normalized efficiency, it is assumed that the electrical power input for APT is the same regardless of whether the receiver is there or not. This assumption is not very accurate for RF power transfer systems.

Therefore, area normalized efficiency is primarily useful for comparing different APT systems with each other, and it is not as useful for comparing APT to RF systems.

The results obtained in this chapter are in agreement with the simulation results presented in [8], in which the authors built detailed models for two wireless power transfer methods: an ultrasonic, and an RF system. They compared the two systems for different depth (1–10 cm) and sizes of the receiver (2–10 mm diameter). They optimized the geometric parameters of each system to maximize the efficiency. Based on their results, the overall efficiencies of both systems decrease as the receiver gets smaller. For a large size receiver ($>\sim 3$ mm), the RF system has higher efficiencies than the acoustic system at small depth of 10 mm. However, as the receiver gets smaller, the acoustic power transfer system results in better efficiency. They demonstrated that for small sizes ($<\sim 3$ mm) and large implant depths ($>\sim 10$ mm), acoustic power transmission can be an order of magnitude more efficient than RF. For an implant size of 2 mm and a depth of 10 mm, the efficiency of an RF link is approximately 3%. Also, for a receiver size of 5 mm, the efficiency at a depth of 3 cm is around 1% for an RF system and 10% for an APT system with a transmitter size of 20 mm. It should be noted that the efficiency numbers for the APT system were calculated considering matching layers for both the transmitter and the receiver.

5.4 Conclusion

An experimental comparison study to compare the efficiency of APT systems to RF systems has been presented. The efficiency of two acoustic power transfer systems, one with similar size transmitter and receiver and the other with different size transmitter and

receivers, was studied. The area normalized efficiency of two APT systems was reported as this is a better figure of merit for acoustic power transfer systems for implants where the size of the receiver is usually much smaller than the size of the transmitter. The efficiency of two RF systems was then compared to two APT systems. Although the comparison was done for the pMUT operating at far-field and RF receivers at near-field or mid-field, it should be noted that the pMUT structure results in slightly higher efficiencies if it operates at near-field when a larger transmitter is used. Simulation results show that the efficiency of the APT system with pMUT can be improved from 0.14% to 0.53% when a diameter of transmitter is doubled.

5.5 References

[1]   Yu, Y., Bhola, V., Tathireddy, P., Young, D. J., and Roundy, S. "Inductive sensing technique for low power implantable hydrogel-based biochemcial sensors," *In 2015 IEEE SENSORS. IEEE*, 2015.

[2]   Yu, Y., Nguyen, T., Tathireddy, P., Young, D. J., & Roundy, S. "Wireless hydrogel-based glucose sensor for future implantable applications," *In 2016 IEEE SENSORS*. IEEE, 2016.

[3]   J. S. Ho *et al.*, "Wireless power transfer to deep-tissue microimplants," *Proc. Natl. Acad. Sci. U. S. A.*, vol. 111, no. 22, p. 201403002, 2014.

[4]   H. Basaeri, D. B. Christensen, and S. Roundy, "A Review of Acoustic Power Transfer for Bio-Medical Implants," *Smart Mater. Struct.*, vol. 25, no. 12, p. 123001, 2016.

[5]   Food and Drug Administration 2008 "Guidance for Industry and FDA—Staff Information for Manufacturers Seeking Marketing Clearance of Diagnostic Ultrasound Systems and Transducers" Silver Spring US FDA.

[6]   Jiang, S., and Georgakopoulos, S. "Electromagnetic wave propagation into fresh water." *J. Electromagn. Anal. Appl.*, vol. 3, no. 07, 261, 2011.

[7]   International Commission on Non-Ionizing Radiation Protection, "ICNIRP Guidelines for Limiting Exposure To Time-Varying Electric, Magnetic and Electromagnetic fields," *Health Phys.*, vol. 74, pp. 494–522, 1998.

[8]   Denisov, A. and Yeatman, E. "Ultrasonic versus inductive power delivery for miniature biomedical implants" *2010 Int. Conf. on Body Sensor Networks,* pp 84–9, 2010.

CHAPTER 6

CONCLUSIONS

The final chapter summarizes the main conclusions from the project and highlights some original contributions. In addition, some suggestions on future work are provided.

6.1 Summary of Conclusions

This project starts with a literature review on the state-of-the-art in wireless power transfer systems for biomedical implants, with a focus on acoustic power transfer systems. To wirelessly power an implantable device using acoustics, a MEMS fabrication process was developed that enables using bulk piezoelectric materials in design and fabrication of pMUTs. The sensitivity of the fabricated device was compared to a similar size COTS transducer. What follows are the primary results of the project.

Chapter 2 compared alternative techniques to batteries in powering implantable devices in the literature including RF, inductive coupling, vibrational energy harvesting, and APT. APT is capable of obtaining more power with smaller devices compared to other methods. This chapter also covered the basic physics and modeling of APT and reviewed the current state of acoustic (or ultrasonic) power transfer for biomedical implants. As the sensing and computational elements for biomedical implants are becoming very small, particular attention was devoted to the scaling of acoustic and alternative power transfer

techniques. Current issues and challenges related to the implementation of this technique for powering implantable devices was presented. Operating at a relatively low frequency to reduce attenuation in human tissue while having small devices to reduce the trauma to the patient is one of the main challenges.

Chapter 3 reported on the evaluation of different ultrasonic receiver structures with different thicknesses of silicon and piezoelectric layers. For a 2×2 mm^2 pMUT, the optimal thickness ratio of the piezoelectric layer to silicon layer was reported to achieve the maximum power from the device. A MEMS fabrication process was presented that is capable of producing piezoelectric thicknesses much higher than current thin film deposition techniques. The fabricated device can operate at lower frequencies compared to COTS transducers resulting in lower attenuation in an aqueous environment. The pMUT is able to generate a power of 0.7 mW across an optimal resistive load of 4.3 kΩ when separated from the transmitter by a distance of 20 mm. The transmitter generates an input power intensity of 322 mW/cm^2 at 88 kHz, less than Food and Drug Administration limit of 720 mW/cm^2. The measured output power of 0.7 mW is significantly higher than that reported for devices with deposited PZT due to the use of bulk PZT, which has better piezoelectric coefficients.

Chapter 4 investigated a comparison study of the performance of the pMUT and COTS transducer in terms of power transfer potential as a function of depth, orientation, and alignment. A 3D COMSOL model was presented, and the results were compared to the measured data. There is acceptable agreement between the COMSOL simulation and experimental results. The pMUT device is less sensitive to location uncertainties compared to a COTS plate mode transducer with a size similar to the fabricated pMUT. The fabricated

pMUT shows great potential for powering implantable medical devices as it can generate sufficient power (0.23 mW) at large depths. (i.e., 40 mm) and is less sensitive to misorientation and misalignment between transmitter and receiver. It was demonstrated that the pMUT has a more robust performance in the presence of location and orientation uncertainties compared to COTS bulk-mode piezoelectric transducers. For example, at zero offset, the percentage improvement in power is 94%. The percentage improvement in power for offsets of -5, - 10, -20, and -30 mm are 994%, 831%, 1087%, 847%, respectively.

Chapter 5 reports on the efficiency of acoustic power transfer systems and compares it to a few example RF systems. The highest efficiency of the systems evaluated is an APT system with 12.8 mm diameter receiver, which achieves 46.5% efficiency at 30 mm separation distance. The area normalized efficiency for APT systems was discussed in more detail in this chapter. The area normalized efficiency of the fabricated pMUT is higher than the efficiency of RF systems even with a much smaller transmitter. As the transmitter gets larger, the Rayleigh distance becomes longer and the receiver would operate at near-field resulting in higher power and efficiency. Simulation results show that the efficiency of the APT system with pMUT can be improved from 0.14% to 0.53% when a diameter of transmitter is doubled.

6.2 Original Contribution

In addition to the findings above, the following highlights the original contribution of this work:

- A comprehensive study was performed on the available wireless power transfer methods for IMDs and in particular acoustics. The results of this comparison

concluded that APT was the most effective method of powering these devices. Specifically, higher power density is achieved at larger depths using acoustics compared to RF and IPT devices with almost the same size.

- A new metric, area normalized efficiency, was defined and introduced into the comparison since the proportion of the sizes of receivers and transmitters is typically not factored into efficiency calculations. This results in less accurate calculations in many situations.

- A MEMS process fabrication was developed that is suitable for ultrasonic power receivers for implants using bulk piezoelectric materials. This process bridges the gap in available piezoelectric layer thicknesses by producing a piezoelectric layer that is thicker than standard microfabrication processes but thin enough for a millimeter scale bending diaphragm.

- The performance of a pMUT structure was compared experimentally to a COTS device in the presence of location uncertainties. It was observed that the generated power from a pMUT structure is less sensitive to misorientation and misalignment of the device. The average percentage improvement in the generated power from pMUT compared to COTS are 86%, 917%, and 111% for depth, alignment, and orientation, respectively.

6.3 Future Work

Below are some recommendations for future work with a basis in the efforts and results presented in this dissertation:

- Fabricate devices smaller than 2×2 mm^2.

- Develop an analytical model for a full acoustic power transfer system with square diaphragms.

- Implementing an entire acoustic power transfer system to power a biomedical device through a tissue phantom.

- A study of how implantable devices migrate in tissue would be beneficial for the design of an acoustic power transfer system. Change in implants position as a function of time. Statistical data of changes in implants depth, orientation, and alignment, due to human interaction, when the implant is implanted in tissue.

- A rigorous comparison of RF and acoustic power transfer systems with taking into consideration the safety constraints and looking at the sizes and frequencies at which APT have higher power density and/or efficiency.

- Study the interaction of alignment and orientation in order to investigate the power drop in cases where the implant experiences misorienation and misalignment at the same time.

APPENDIX A

INVESTIGATION OF POTENTIAL OF

USING AN ARRAY OF DEVICES

Instead of designing a device with a 4 mm^2 area with a resonance frequency of 88 kHz, one could also design an array of smaller and thinner devices with the same resonance frequency and fit them in the 4 mm^2 area. We did 3D COMSOL simulations for two smaller device sizes with the same resonance frequency as our presented pMUT and compared them together in Table A.1. An array of small devices would result in slightly better power numbers; however, there are a couple of reasons that we prefer a thick and big device rather than a thin and small device. First, we want to take advantage of thick bulk piezoelectric materials. Thin piezo films generally suffer from a low electromechanical coupling coefficient due to film stresses and/or lower density compared to their bulk piezo material counterparts. We've done simulations for thin devices using piezoelectric electromechanical coupling coefficient for deposited PZT as well to show how it can affect the generated power. We used the average electromechanical properties for the thin film piezoelectric materials from Table 4.1 in Chapter 4 (a thin piezoelectric layer with a d_{31} of 55 pm/V, coupling coefficient of 16%, and relative permittivity of 800). Using a deposited PZT instead of a bulk material clearly can affect the output power. Based on the COMSOL simulations, it can result in more than four times power difference. Second, we should mention that we did not assume any gaps between the elements and or any space for bond pads in our simulations. Considering the gaps between elements result in a power drop as well. As we increase the number of elements, the loss in the area increases as well. Finally, a smaller device that can operate at the same resonance frequency would have higher stress under the same loading condition. As the number of elements increases, the stress on each element also increases, which results in higher output; however, one should be careful not to exceed the maximum allowable stress of the film.

Table A.1 COMSOL simulations for an array of devices with deposited and bulk PZT

Size of an element		2 mm × 2 mm	1 mm × 1mm	0.5 mm × 0.5 mm
PZT thickness (μm)		20	6	2
Silicon thickness (μm)		50	15	5
Number of elements		1	4	16
Bulk PZT	Power from one element (mW)	2.978	0.789	0.236
	Total power (mW)	2.978	3.154	3.773
Deposited PZT	Power from one element (mW)	-	0.178	0.053
	Total power (mW)	-	0.712	0.848

APPENDIX B

DETAILS ON THE FABRICATION PROCESS

The pMUT fabrication process starts with a 4 in Silicon-on-Insulator (SOI) wafer consisting of a 50 μm device layer and 500 nm buried oxide layer supported by a 415 μm silicon handle layer. The fabrication process steps (shown in Figure B.1) are as follows:

1. Grow a 100 nm layer of oxide on the wafer. Use wet oxidation with CleanOx furnace. The temperature is 950ºC. The information and the process steps can be found in ProTemp Furnace SOP located in the Nanofab.

2. Pattern the wafer

    a. Deposit a 2 μm positive photoresist for the lithography using CEE 200X 9260 Spinner with 2000 rpm for 60 s

    b. Baked the wafer at 110˚C for 60 s

    c. Develop with AZ 1:1 for 30 s

    d. Rinse the wafer with DI water for 2 min

3. Deposit metal layers on the silicon wafer using Denton Discovery 18.

    a. 50 nm of chromium as an adhesion layer, use 100 W power for 2.95 min

    b. 2.2 μm of gold, use 100 W power for 40 min

    c. 600 nm of Indium, It is important to use low power for In sputtering in order to avoid melting the target.

    d. 100 nm of gold, use 100 W power for 2 min

4. Lift off the photoresist.

5. Deposit the metal bonding layers on one side of the PZT sheet using the Denton Discovery 18. The PZT sheet needs to be cleaned with acetone first.

    a. 100 nm of chromium as an adhesion layer, use 100 W power for 5.9 min

    b. 100 nm of Platinum as diffusion barrier, use 100 W power for 5 min

c.   1.2 μm of gold, use 100 W power for 24 min

6. Dice the PZT sheet into square shapes with the desired dimensions using a manual dicing saw.

7. Bond the diced PZTs to the silicon wafer using a heated platen press. Use the maximum temperate on the equipment (188˚C) as the bonding temperature and set the bonding pressure to 0.75 MPa. The bonding time is set for 1 hr.

8. Polish the PZT. Our polishing process was: manually polish the wafer for a short time, measure it, then repeat polishing.

a.   Mount the wafer, PZT-side down (so the PZT is exposed to be polished off) to a metal polishing chuck using a Wafer Grip.

b.   Place the stack on a hot plate and set to 160ºC, making sure the wafer grip and wafer remained centered on the chuck. Wait for hot plate to reach temperature. While the wafer is heating, carefully press down on it using several folded paper towels and mov it around the wafer grip to help remove any air bubbles that may be between the grip and the wafer. When the plate reaches the set temp of 160º C the wafer grip adhesive should be fluid and the wafer should move around on the grip easily. At this point, carefully remove the chuck with the attached wafer from the hot plate and place it on the metal plate of the polishing wheel to cool off.

c.   When it is cool enough to handle, screw on the chuck handle.

d.   Attach the abrasion paper to a plastic polishing wheel bat by peeling off the plastic on the back to expose the sticky tape and pressing the paper

against the bat. The polishing wheel should be set to its full speed. Polish the wafer with grit papers 1200, 800, and 600.

e. To begin polishing the wafer, use DI water to wet the abrasion paper and pressed the chuck against the abrasion paper to grind off the excess PZT. Once the wafer is moving smoothly against the platen, gradually increase the pressure of the chuck against the polishing wheel. It is important to keep the wafer moving in order to grind the wafer evenly. (It may also help to rotate the wafer around its own axis.) The abrasion paper must be kept wet with DI water throughout process to remove ground material and act as a lubricant.

9. Release the diaphragm with a Deep Reactive Ion Etching (DRIE) of the handle wafer from the backside using oxide as an etch stop.

a. Use the third mask for pattern generation

b. Backside alignment

c. Use STS ICP ASE in the nanofab and 12TO6SOP as the recipe for etching

10. Deposit the top inner and outer electrodes

a. Pattern the wafer using the same lithography and lift-off technique using the second mask.

b. Deposit 100 nm Chromium on the wafer using a sputtering chamber outside the Nanofab since it is not allowed to use the sputtering machine in the Nanofab for sputtering on top of PZT.

c. Deposit 300 nm gold using Denton 635.

11. Dice the wafer

12. Wirebond the chip to a ceramic package
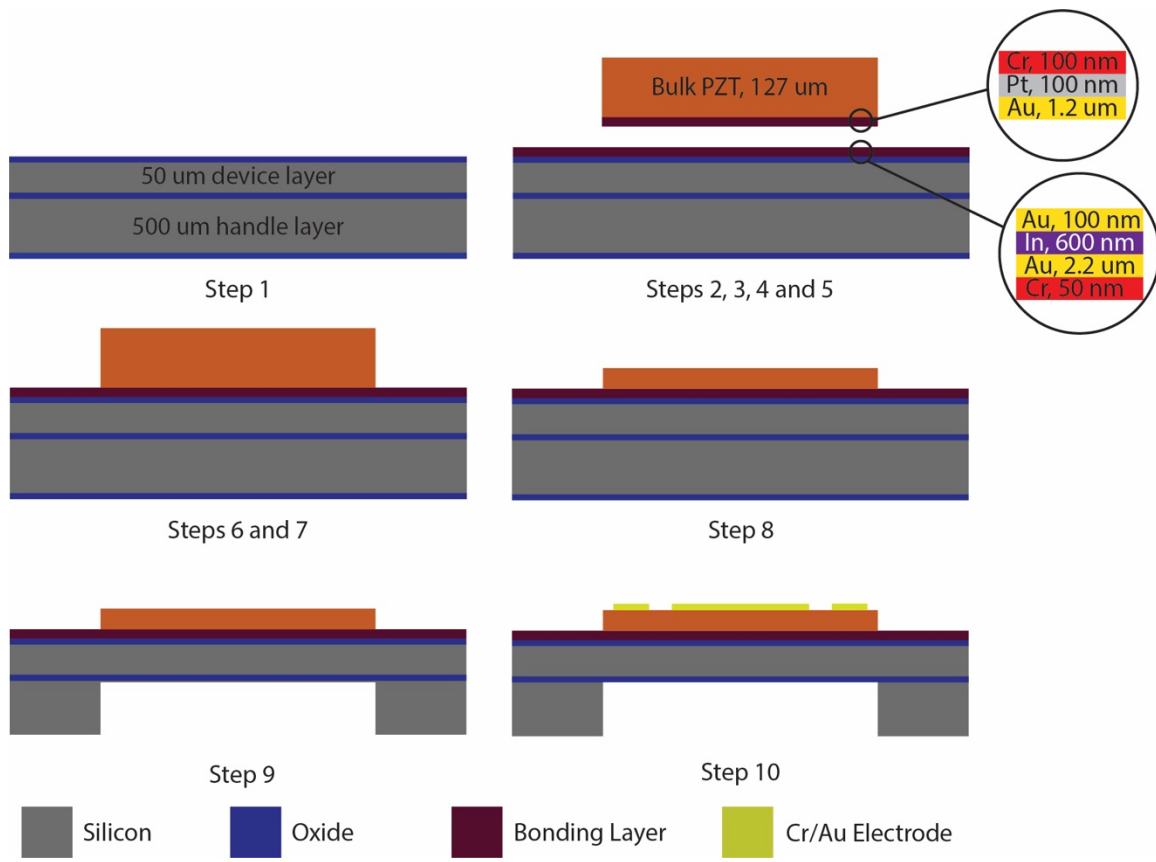
Figure B.1. Fabrication process flow.

APPENDIX C

EXPERIMENTAL RESULTS FROM PORK TESTS

The final goal of the presented pMUT in this work is to be implanted in human tissue. All the tests have been carried out in water since it has similar acoustic properties to a fatty muscle. However, water does not have as attenuation as the human tissue has. Therefore, we decided to repeat the tests when pork meat is placed in between the transmitter and the receiver. The thickness of the pork meat was around 22 mm, as shown in Figure C.1. We did the tests in two depths (22 mm, and 43 mm) with one and two slices of pork meats (see Figure C.2), and compared them to their corresponding power numbers in water. The results from the pMUT device are shown in Tables C.1 and C.2, respectively.
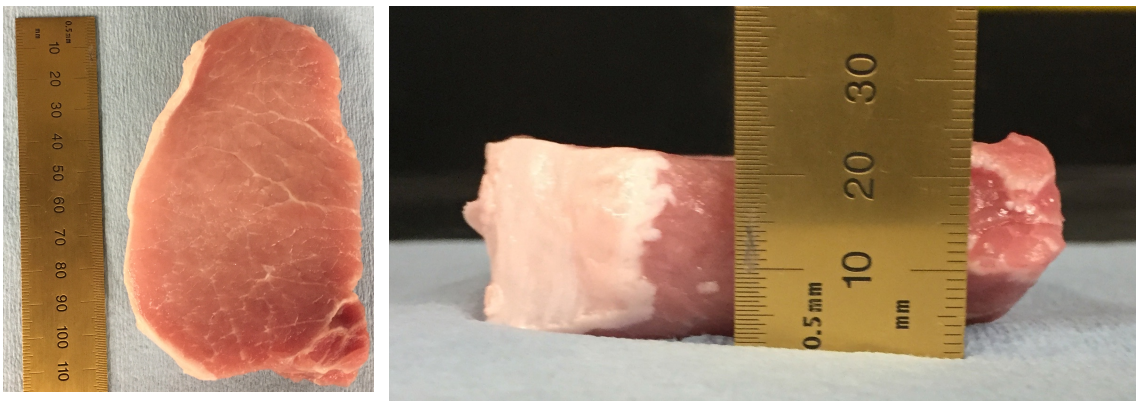
Figure C.1. Pork meat used for the experiments.
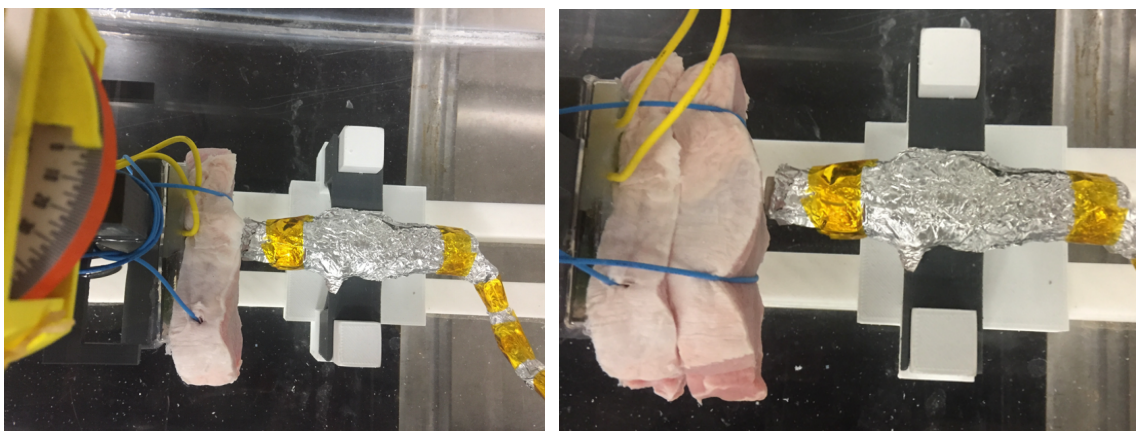
Figure C.2. Experimental acoustic tank with one and two slices of pork meats.

Table C.1 Experimental results of the pMUT device with pork meat

Depth (mm)	Water		Pork	
	V_{p-p} (V)	Average Power (mW)	V_{p-p} (V)	Average Power (mW)
22	3.84	0.4287	2.38	0.1647
43	2.5	0.1817	1.04	0.0314

Table C.2 Experimental results of the COTS device with pork meat

Depth (mm)	Water		Pork	
	V_{p-p} (V)	Average Power (mW)	V_{p-p} (V)	Average Power (mW)
22	3.079	0.3039	1.42	0.0646
43	1.909	0.1168	0.485	0.0075

The results show that either the attenuation or the reflection at the surface of the pork is quite significant. We did some COMSOL simulations by changing the density and speed of the sound of water to muscle and considering the attenuation effect in that medium. We used acoustic properties for muscle from literature. The simulation results are close to simulations. At 22 mm and 43 mm depth in tissue, COMSOL predicts 0.19 mW and 0.036 mW of power, respectively. From the pork tests, we obtained 0.16 mW and 0.0314 mW for depth 22 mm and 43 mm, respectively. The comparison of the experimental and simulation results for the pMUT device are shown in Figure C.3.
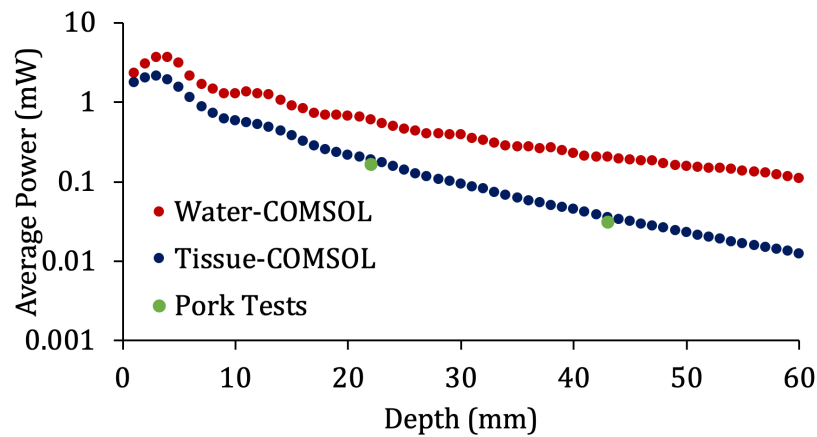
Figure C.3. Comparison of the simulation and experimental results for the pMUT device in water and pork meat.